



Spectroscopic Study of Ice Analogs of Trans-Neptunian Objects Exposed to Ionizing Radiation. II. Infrared Spectra and Functional Groups

Chaojiang Zhang^{1,2} , Jia Wang^{1,2} , Andrew M. Turner^{1,2}, Leslie A. Young³ , and Ralf I. Kaiser^{1,2}

¹ Department of Chemistry, University of Hawaii at Mānoa, Honolulu, HI 96822, USA; ralfk@hawaii.edu

² W. M. Keck Laboratory in Astrochemistry, University of Hawaii at Mānoa, Honolulu, HI 96822, USA

³ Department of Space Studies, Southwest Research Institute, Boulder, CO 80302, USA; layoung@boulder.swri.edu

Received 2025 February 14; revised 2025 April 8; accepted 2025 April 24; published 2025 June 16

Abstract

The surfaces of airless trans-Neptunian objects (TNOs) are subject to continuous ionizing radiation from solar winds and Galactic cosmic rays accompanied by alteration of surface compositions. The crust resulting from chemical reactions and products at various radiation levels can influence their spectral gradients and surface colors, which are essentially controlled by the chromophores of complex organic molecules. This study presents comprehensive infrared spectra of TNO-analog ices processed by ionizing radiation, which include water, methane, ammonia, carbon monoxide, carbon dioxide, and methanol along with their binary mixtures. The spectral data suggest that complex organic and inorganic products are synthesized when carbon-bearing ice mixtures are exposed to proxies of Galactic cosmic-ray and solar wind irradiation. A series of functional groups of hydrocarbons, hydroxyl, amine, carbonyl, imine, cyanate, and nitrile are identified, which can be incorporated in complex compounds including alcohols, aldehydes, ketones, carboxylic acids, esters, amines, amides, cyanates, and nitriles along with critical prebiotic molecules such as sugar and amino acids. By combining them with corresponding visible reflectance spectra, these species play a crucial role in revealing the color diversity of TNOs and are also highly relevant to the emergence of life in our solar system. The findings in this study serve as an important starting point to fully unravel the chemical complexity, compositions, and evolutionary processes of objects in the outer solar system and will also provide fundamental support for the interpretation of astronomical observations such as those from the James Webb Space Telescope.

Unified Astronomy Thesaurus concepts: Trans-Neptunian objects (1705); Surface ices (2117); Experimental data (2371); Infrared spectroscopy (2285)

1. Introduction

Trans-Neptunian objects (TNOs) represent a vast population of small objects in the outer solar system whose heliocentric orbits hold semimajor axes between Neptune and the Oort cloud, approximately 30–2000 au from the Sun (D. Jewitt & J. Luu 1993; D. K. Prialnik et al. 2020; B. Gladman & K. Volk 2021). Considering the large distance, TNOs have a low surface temperature typically ranging from 30 to 50 K and thereby are covered with various molecular ices. Pluto's surface, one of the largest TNOs, is dominated by solid water (H_2O), nitrogen (N_2), methane (CH_4), and carbon monoxide (CO) (M. E. Brown 2012; D. P. Cruikshank et al. 2015; M. A. Barucci & F. Merlin 2020; L. A. Young et al. 2020; M. N. De Prá et al. 2025; N. Pinilla-Alonso et al. 2025). Simultaneously, the surfaces of these icy bodies are subject to continuous irradiation by the solar wind, ultraviolet photons, and Galactic cosmic rays (GCRs), leading to complex chemical products that are essential in understanding the color diversity of TNOs (D. C. Jewitt & J. X. Luu 2001; J. F. Cooper et al. 2003; D. P. Cruikshank et al. 2005; R. Brunetto et al. 2006; M. E. Brown et al. 2011; C. J. Bennett et al. 2013; N. Sakakibara et al. 2020; E. Quirico et al. 2023; C. Zhang et al. 2023b, 2024). Knowledge of these compounds in trans-Neptunian (TN) space can provide valuable clues for understanding the chemical and physical conditions of the

protoplanetary disk, the processes involved in planetary formation, and the constraints of the migration models of giant planets, which are pivotal in sculpting the early history of our solar system (J. X. Luu & D. C. Jewitt 2002; M. Barucci et al. 2008; D. Nesvorný 2018; D. Nesvorný et al. 2019; D. K. Prialnik et al. 2020; K. I. Öberg et al. 2023). The dynamical simulation of the solar system suggests that TNOs are one of the main sources of short-period comets like 67P/Churyumov–Gerasimenko, which are possibly transformed into delivery systems for important prebiotic species to the nascent Earth (C. F. Chyba et al. 1990; C. Chyba & C. Sagan 1992; M. Pasek & D. Lauretta 2008; D. Nesvorný et al. 2017; C. R. Walton et al. 2024). Thus, the investigation of molecules on TNOs along with underlying formation mechanisms, especially biologically relevant compounds like sugars and amino acids, has promise to shed light on the origin of life in our solar system (J. R. Cronin & S. Pizzarello 1997; G. Cooper et al. 2001; K. Altweig et al. 2016; G. Cooper & A. C. Rios 2016; D. P. Cruikshank et al. 2019; Y. Furukawa et al. 2019; Y. Oba et al. 2019; S. A. Sandford et al. 2020). However, numerous compositions of TNOs remain inadequately described due to most TNOs being too faint to permit a detailed spectroscopic study.

Despite the fact that probing the materials on the surface of TNOs by remote observation remains a challenge, laboratory investigations of TNO surface ice analogs processed by various radiation sources can effectively facilitate the understanding of molecule distributions on these small bodies (R. Hudson et al. 2008; C. J. Bennett et al. 2013; B. C. Ferrari et al. 2021). The first confirmed and also most widespread



Original content from this work may be used under the terms of the [Creative Commons Attribution 4.0 licence](#). Any further distribution of this work must maintain attribution to the author(s) and the title of the work, journal citation and DOI.

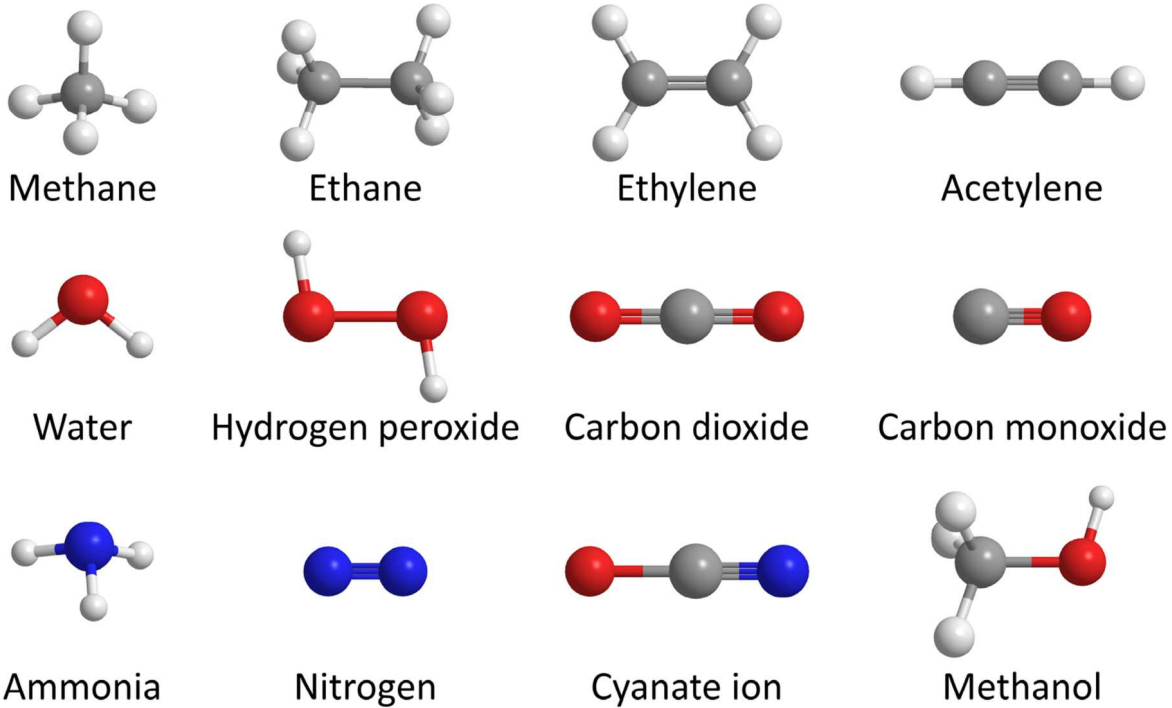


Figure 1. Molecules identified on the surface of TNOs. The colors correspond to the following elements: hydrogen (white), carbon (gray), nitrogen (blue), and oxygen (red). Note that ground- and space-based observations also indicate silicates and unassigned refractory carbonaceous materials on TNO surfaces, along with tentative detection of hydrogen sulfide (H_2S), which is not presented here.

Table 1
Experimental Parameters of the Ices, Ratio, and Temperature Used in This Work

Ice No.	Composition	Ratio	Temperature (K)	Ice No.	Composition	Ratio	Temperature (K)
1	H_2O	...	40	19	$^{13}\text{CH}_4 : ^{13}\text{CO}_2$	$(1.1 \pm 0.2) : 1$	20
2	H_2O	...	10	20	$^{13}\text{CH}_4 : ^{13}\text{CO}_2$	$(1.2 \pm 0.2) : 1$	10
3	NH_3	...	40	21	$^{13}\text{CH}_4 : ^{13}\text{CH}_3\text{OH}$	$(2.2 \pm 0.2) : 1$	20
4	NH_3	...	10	22	$^{13}\text{CH}_4 : ^{13}\text{CH}_3\text{OH}$	$(0.8 \pm 0.2) : 1$	10
5	$\text{H}_2\text{O} : ^{13}\text{CH}_4$	$(1.8 \pm 0.2) : 1$	20	23	$\text{NH}_3 : ^{13}\text{CO}$	$(0.4 \pm 0.2) : 1$	20
6	$\text{H}_2\text{O} : ^{13}\text{CH}_4$	$(1.7 \pm 0.2) : 1$	10	24	$\text{NH}_3 : ^{13}\text{CO}$	$(0.4 \pm 0.2) : 1$	10
7	$\text{H}_2\text{O} : \text{NH}_3$	$(2.8 \pm 0.2) : 1$	40	25	$\text{NH}_3 : ^{13}\text{CO}_2$	$(0.6 \pm 0.2) : 1$	40
8	$\text{H}_2\text{O} : \text{NH}_3$	$(2.6 \pm 0.2) : 1$	10	26	$\text{NH}_3 : ^{13}\text{CO}_2$	$(0.6 \pm 0.2) : 1$	10
9	$\text{H}_2\text{O} : ^{13}\text{CO}$	$(1.0 \pm 0.2) : 1$	20	27	$\text{NH}_3 : ^{13}\text{CH}_3\text{OH}$	$(0.3 \pm 0.2) : 1$	40
10	$\text{H}_2\text{O} : ^{13}\text{CO}$	$(1.6 \pm 0.2) : 1$	10	28	$\text{NH}_3 : ^{13}\text{CH}_3\text{OH}$	$(0.3 \pm 0.2) : 1$	10
11	$\text{H}_2\text{O} : ^{13}\text{CO}_2$	$(1.2 \pm 0.2) : 1$	40	29	$^{13}\text{CO} : ^{13}\text{CO}_2$	$(1.1 \pm 0.2) : 1$	20
12	$\text{H}_2\text{O} : ^{13}\text{CO}_2$	$(1.2 \pm 0.2) : 1$	10	30	$^{13}\text{CO} : ^{13}\text{CO}_2$	$(1.1 \pm 0.2) : 1$	10
13	$\text{H}_2\text{O} : ^{13}\text{CH}_3\text{OH}$	$(1.0 \pm 0.2) : 1$	40	31	$^{13}\text{CO} : ^{13}\text{CH}_3\text{OH}$	$(1.2 \pm 0.2) : 1$	20
14	$\text{H}_2\text{O} : ^{13}\text{CH}_3\text{OH}$	$(0.8 \pm 0.2) : 1$	10	32	$^{13}\text{CO} : ^{13}\text{CH}_3\text{OH}$	$(1.1 \pm 0.2) : 1$	10
15	$^{13}\text{CH}_4 : \text{NH}_3$	$(1.8 \pm 0.2) : 1$	20	33	$^{13}\text{CO}_2 : ^{13}\text{CH}_3\text{OH}$	$(1.2 \pm 0.2) : 1$	40
16	$^{13}\text{CH}_4 : \text{NH}_3$	$(1.7 \pm 0.2) : 1$	10	34	$^{13}\text{CO}_2 : ^{13}\text{CH}_3\text{OH}$	$(1.2 \pm 0.2) : 1$	10
17	$^{13}\text{CH}_4 : ^{13}\text{CO}$	$(1.0 \pm 0.2) : 1$	20
18	$^{13}\text{CH}_4 : ^{13}\text{CO}$	$(0.9 \pm 0.2) : 1$	10

Note. All ices have a thickness of 850 ± 50 nm with an irradiation dose up to $82 \pm 10 \text{ eV amu}^{-1}$ and are then warmed up to 320 K at 1 K min^{-1} .

molecule on TNOs is solid water (R. H. Brown et al. 1999; M. Barucci et al. 2008; M. E. Brown 2012; M. S. Gudipati & J. Castillo-Rogez 2013), and therefore extensive studies have been carried out to explore the radiation chemistry on water-bearing ices with primary products of hydrogen peroxide (H_2O_2), hydrogen (H_2), and oxygen (O_2) (M. H. Moore et al. 2003; R. L. Hudson & M. H. Moore 2005; W. Zheng et al. 2006a, 2009b; T. Bartels-Rausch et al. 2012; A. L. F. de Barros et al. 2015; K. A. Kipfer et al. 2024). H_2O_2 was recently

confirmed on Charon by the James Webb Space Telescope (JWST; S. Protopapa et al. 2024). Except for H_2O , the spectroscopic and chemical evolution of processed ice mixtures containing N_2 , CH_4 , and CO molecules has also been studied as a consequence of their detection on Pluto (C. J. Bennett et al. 2009; Y. S. Kim et al. 2011; Y. S. Kim & R. I. Kaiser 2012; C. K. Materese et al. 2014; C. K. Materese et al. 2015; B. Augé et al. 2016; M. J. Abplanalp et al. 2018; R. L. Hudson 2018; F. A. Vasconcelos et al. 2020; N. F. Kleimeier et al. 2022). In

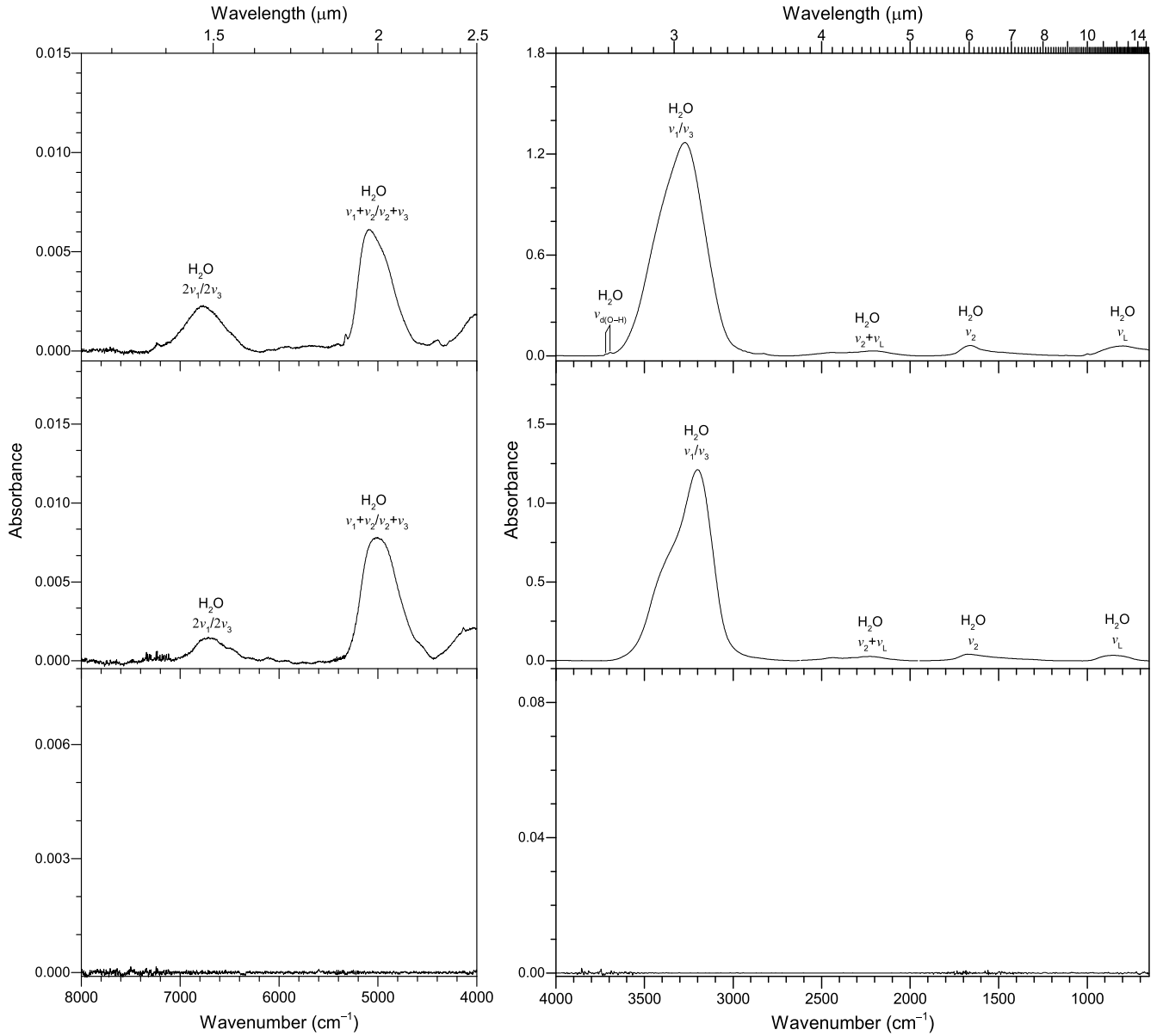


Figure 2. Infrared spectra of water (H_2O) before (top) and after (middle) irradiation at 40 K. The infrared spectra of the irradiated sample warmed up to 320 K are shown at the bottom. Only noticeable peaks are labeled for clarity, and detailed peak assignments are listed in Table 2. L and d indicate libration and dangling, respectively.

addition, observation data have reported the existence of additional molecules on the surface of TNOs, including ammonia (NH_3), carbon dioxide (CO_2), methanol (CH_3OH), ethane (C_2H_6), ethylene (C_2H_4), acetylene (C_2H_2), and cyanate ion (OCN^-) along with tentative detection of hydrogen sulfide (H_2S), silicates, and tholin-like constituents (Figure 1; M. E. Brown 2012; T. Seccull et al. 2018; M. A. Barucci & F. Merlin 2020; W. M. Grundy et al. 2020; J. P. Emery et al. 2024; M. N. De Prá et al. 2025; N. Pinilla-Alonso et al. 2025). Irradiation experiments of ices composed of these molecules have suggested that various complex organic molecules could potentially be detected in TN space and reproduce the colors of TNOs through chemical reactions (M. E. Brown et al. 2011; W. M. Grundy et al. 2016; M. J. Poston et al. 2018; N. Sakakibara et al. 2020; N. F. Kleimeier et al. 2022; Y. Y. Phua et al. 2022; C. Zhang et al. 2023b, 2024). R. Brunetto et al. (2006) reported a strong

reddening phenomenon when frozen CH_4 and CH_3OH are exposed to ion radiation in a vacuum, and observed dark refractory residues. N. Sakakibara et al. (2020) demonstrated that the reddish coloration from processed $\text{H}_2\text{O}-\text{CH}_3\text{OH}$ ice mixtures disappears upon heating to room temperature, suggesting that some ultraredd materials in TN space might only be stable at low temperatures. E. Quirico et al. (2023) employed high-energy heavy ions to process CH_3OH ices and found that the formation of conjugated olefinic groups can control the absorption of short wavelengths in the visible spectrum that could result in the reddish matter on Arrokoth. Our previous irradiation experiments suggested that ionizing radiation exposure on carbon-containing ices presents notable reddening on the visible reflectance due to the formation of complex organic molecules having absorption in the visible wavelengths (C. Zhang et al. 2025a), e.g., polycyclic aromatic hydrocarbons (PAHs) connected by

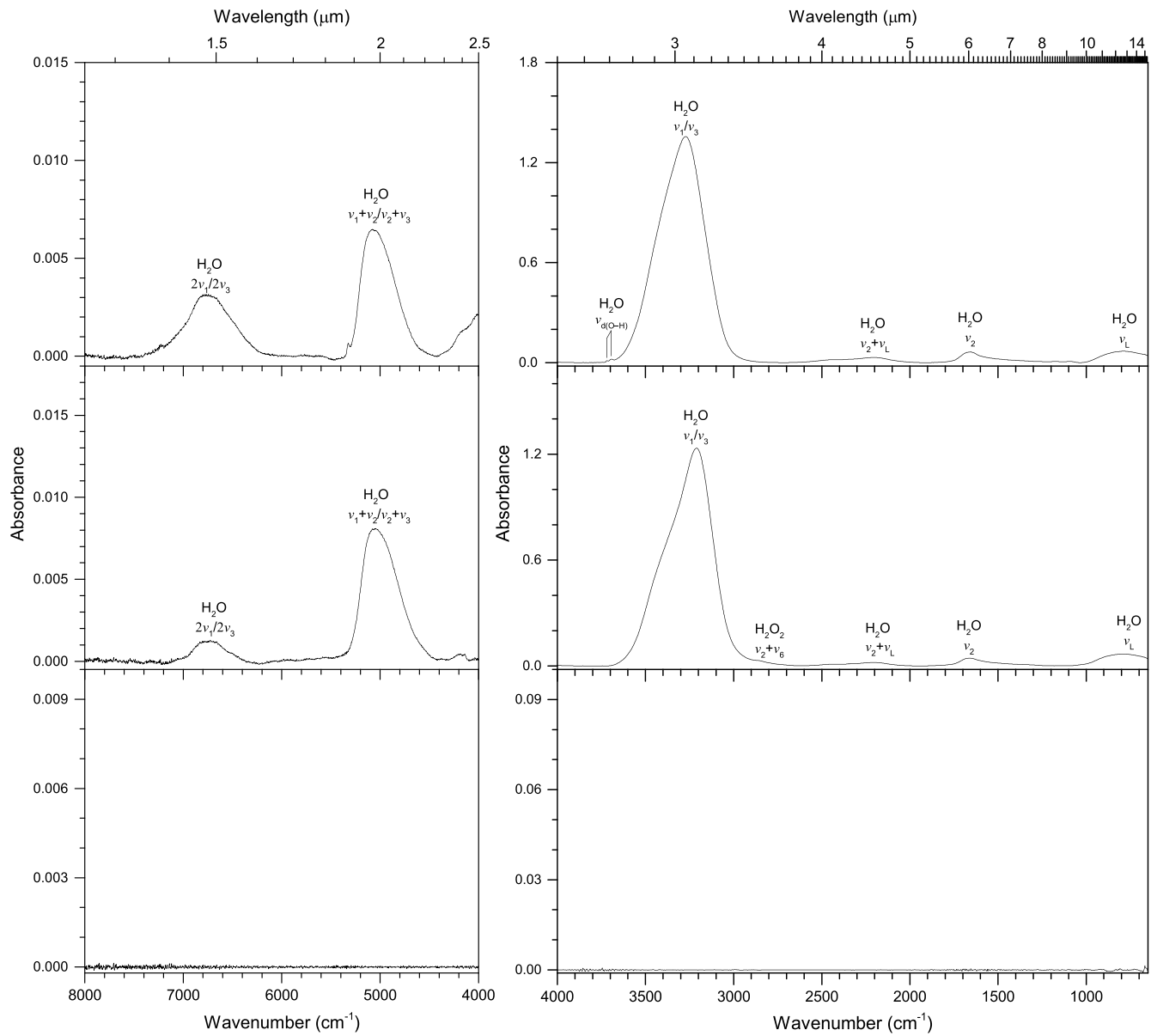


Figure 3. Infrared spectra of water (H_2O) before (top) and after (middle) irradiation at 10 K. The infrared spectra of the irradiated sample warmed up to 320 K are shown at the bottom. Detailed peak assignments are listed in Table 2. L and d indicate libration and dangling, respectively.

Table 2
Infrared Absorption Features of Water (H_2O) and Ammonia (NH_3) Ices before and after Irradiation at 40 and 10 K

40 K		10 K		Assignment	Reference		
Before Irradiation	After Irradiation	Before Irradiation	After Irradiation				
Position (cm^{-1})							
Water (H_2O)							
6789	6753	6799	6776	$2v_1/2v_3$ (H_2O)	(1, 2, 3, 4)		
5324	...	5324	...	$v_{\text{d(O-H)}} + v_1 + v_2/v_{\text{d(O-H)}} + v_2 + v_3$ (H_2O)	(1, 2, 3, 4)		
5076	5000	5075	5044	$v_1 + v_3/v_2 + v_3$ (H_2O)	(1, 2, 3, 4)		
4395	$2v_2 + 2v_L$ (H_2O)	(1, 2, 3, 4)		
3716, 3693	...	3717, 3693	...	$v_{\text{d(O-H)}}$	(1, 2, 3, 4)		
3269	3200	3269	3210	v_1/v_3 (H_2O)	(1, 2, 3, 4)		
...	2851	$v_2 + v_6$ (H_2O_2)	(2, 5)		
2215	2231	2208	2213	$v_2 + v_L$ (H_2O)	(1, 2, 3, 4)		
1664	1666	1664	1664	v_2 (H_2O)	(1, 2, 3, 4)		
802	820	803	821	v_L (H_2O) libration	(1, 2, 3, 4)		
Ammonia (NH_3)							
6514	...	6514	...	$2v_1$ (NH_3)	(6, 7)		
6100	...	6100	...	$v_2 + v_3 + v_4$ (NH_3)	(6, 7)		

Table 2
(Continued)

40 K		10 K		Assignment	Reference
Before Irradiation	After Irradiation	Before Irradiation	After Irradiation		
Position (cm^{-1})					
4995	...	4995	$v_3 + v_4$ (NH_3)	(6, 7)
4476	...	4475	...	$v_2 + v_3$ (NH_3)	(6, 7)
4334	...	4334	...	$v_1 + v_2$ (NH_3)	(6, 7)
3370	3367	3370	3367	v_3 (NH_3)	(6, 7)
3212	3208	3212	3209	v_1 (NH_3)	(6, 7)
...	3048	...	3052	N–H stretch within cis- $\text{HN}=\text{NH}$	(7, 8)
...	2774	...	2774	N–H stretch within $\text{N}=\text{NH}_2$	(7, 8)
2430	2440	2431	2436	$\text{N}-\text{H}^+$ stretch	(7, 8)
...	2328	$\text{N}\equiv\text{N}$ stretch within N_2	(7, 8)
...	2088	...	2087	N–N–N asymmetric stretch within HN_3	(7, 8)
1626	1630	1626	1629	v_4 (NH_3)	(6, 7)
1074	1098	1067	1091	v_2 (NH_3)	(6, 7)

References. (1) W. Zheng et al. (2009b); (2) W. Zheng et al. (2006a); (3) V. Buch & J. P. Devlin (1991); (4) C. M. Tonauer et al. (2021); (5) W. Zheng et al. (2006b); (6) J. S. Holt et al. (2004); (7) W. Zheng et al. (2008); (8) G. Socrates (2004).

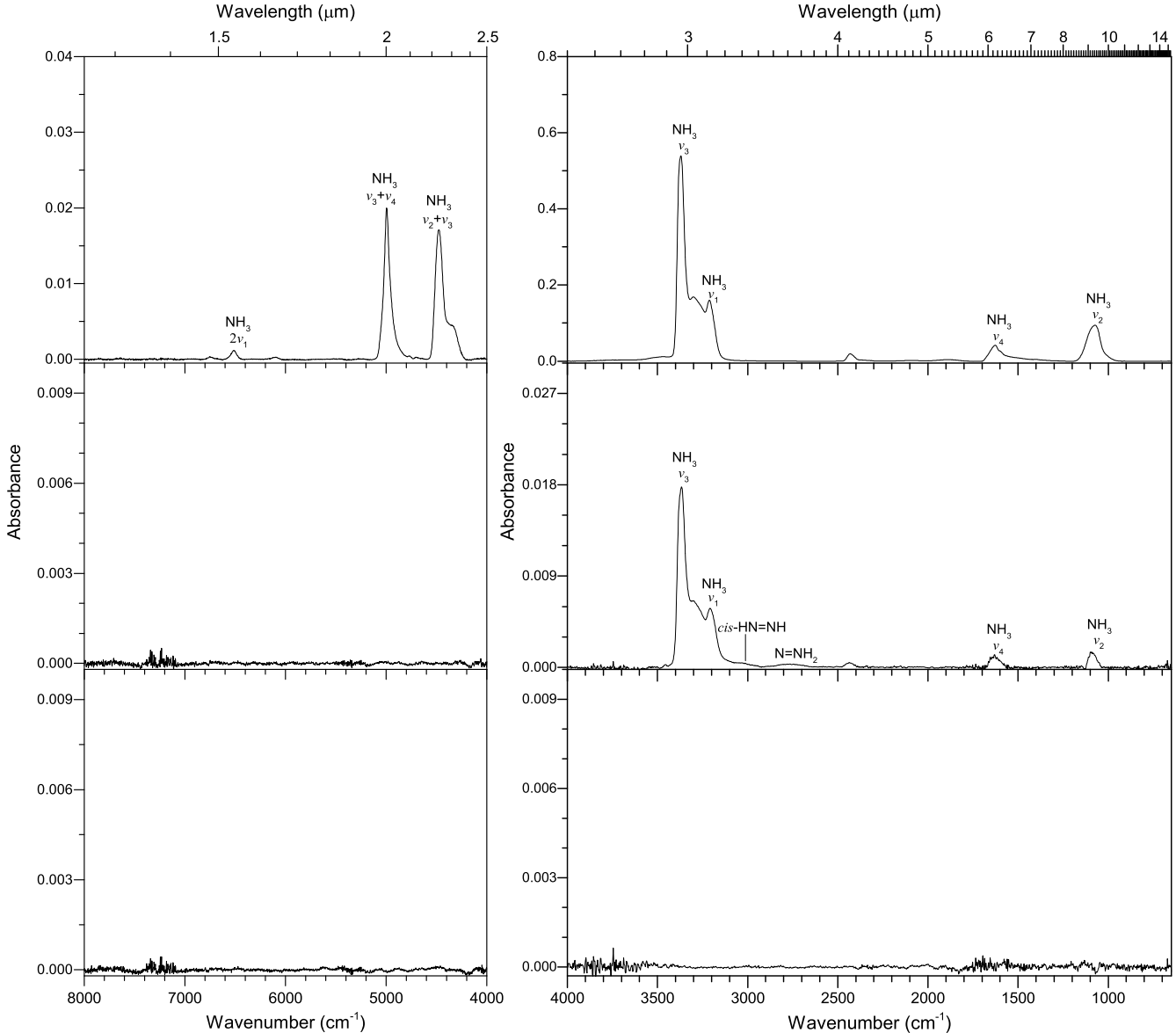


Figure 4. Infrared spectra of ammonia (NH_3) before (top) and after (middle) irradiation at 40 K. Detailed peak assignments are listed in Table 2. The infrared spectra of the irradiated sample warmed up to 320 K are shown at the bottom.

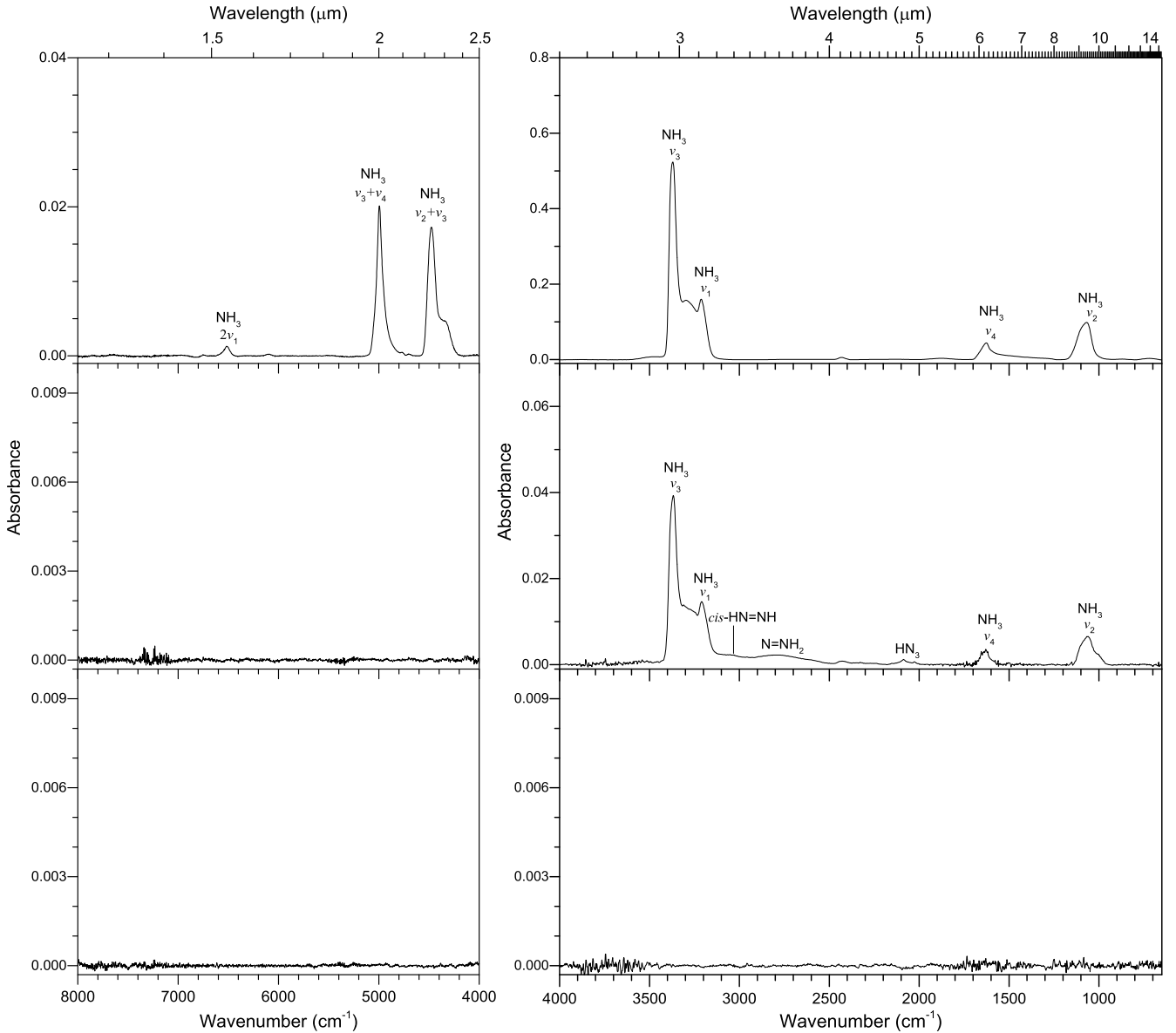


Figure 5. Infrared spectra of ammonia (NH_3) before (top) and after (middle) irradiation at 10 K. Detailed peak assignments are listed in Table 2. The infrared spectra of the irradiated sample warmed up to 320 K are shown at the bottom.

unsaturated linkers (C. Zhang et al. 2023b) and sugar (related) molecules (C. Zhang et al. 2024). However, it is not feasible to define specific chromophores—functional groups responsible for the colors of matter—from the visible reflectance spectra due to the lack of distinctive features.

This paper presents the infrared spectra data of GCR proxy processed ices of water, methane, ammonia, carbon monoxide, carbon dioxide, and methanol along with their binary mixtures as analogs of TNO surface compositions. Altogether, there are 34 ices composed of these compounds, which are listed in Table 1. These experiments mimic GCR penetration into small TNOs and form various products, contributing to the diverse colors of TNOs (R. E. Johnson 1990; J. F. Cooper et al. 2003; G. Strazzulla et al. 2003; C. J. Bennett et al. 2005; R. I. Kaiser et al. 2011; Y. S. Kim & R. I. Kaiser 2012; B. M. Jones & R. I. Kaiser 2013;

A. M. Turner & R. I. Kaiser 2020; C. Zhang et al. 2023b, 2025a). The formation of key functional groups related to chromophores, which in fact dictate the color, is analyzed, starting with distinct precursor molecules. The irradiation temperatures are kept at 40 K, which mimics the cryogenic condition for TNOs. Methane and carbon monoxide cannot condense at this temperature (C. J. Bennett et al. 2004, 2006); therefore, methane- and carbon monoxide-bearing samples are processed at 20 K. In addition, the infrared spectra at 10 K are also collected, which are highly relevant to the surface composition of TNOs with an average temperature lower than 20 K, such as Sedna (S. M. Menten et al. 2022), objects in the Oort cloud, and of ice-coated interstellar nanoparticles in cold molecular clouds (M. K. McClure et al. 2023; H. M. Cuppen et al. 2024; J. A. Noble et al. 2024). This comprehensive set of infrared

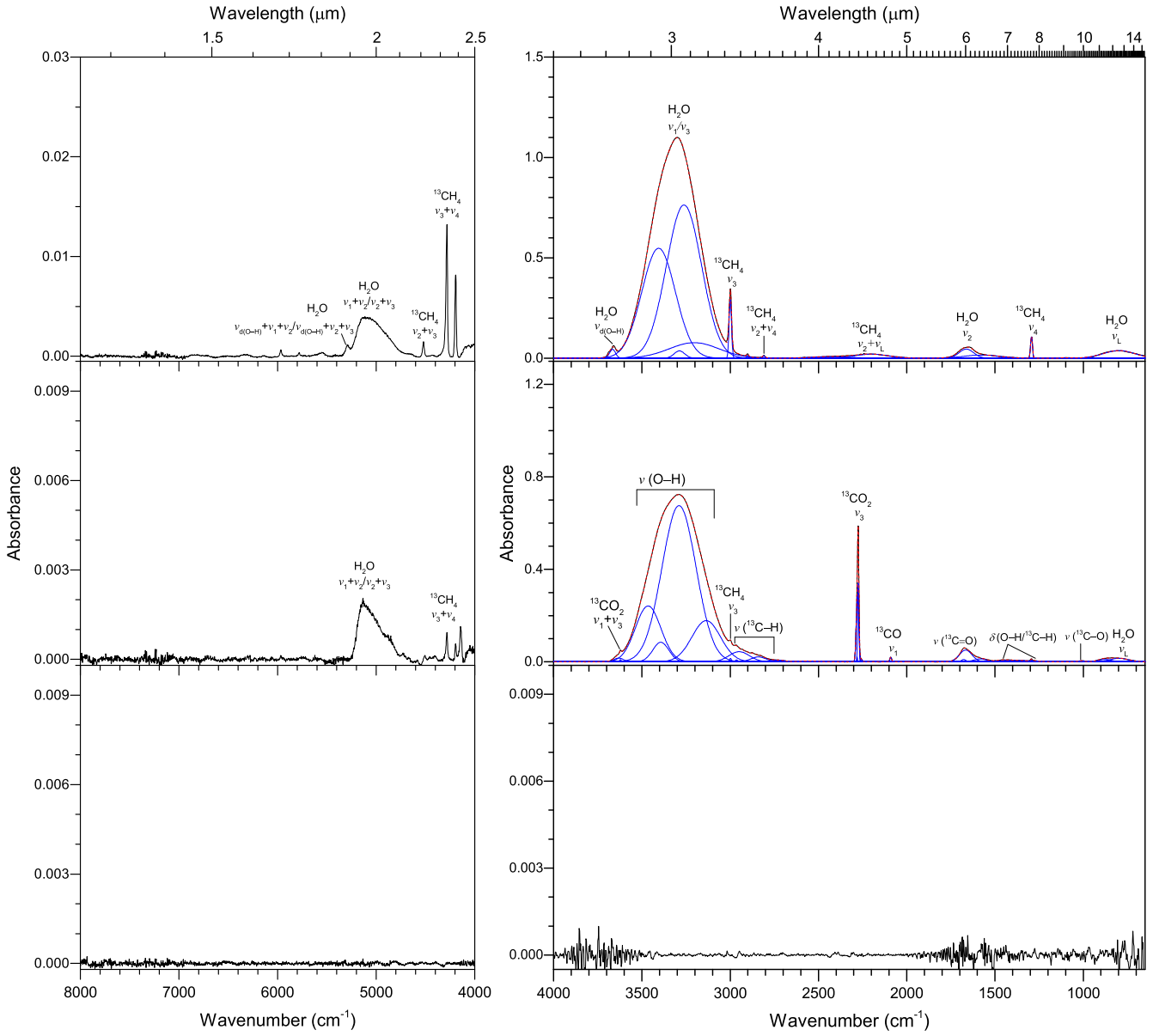


Figure 6. Infrared spectra of water–methane (H_2O – $^{13}\text{CH}_4$) ice mixtures before (top) and after (middle) irradiation at 20 K. The infrared spectra of the irradiated sample warmed up to 320 K are shown at the bottom. The experimental spectra are plotted in black, the deconvoluted peaks are in blue, and the sums are in red. Only noticeable peaks are labeled for clarity, and detailed peak assignments are listed in Table 3. L indicates libration.

spectra data, combined with their visible reflectance spectra, will provide important information for understanding the color diversity of TNOs along with underlying compositions and fundamental support for the interpretation of astronomical observations such as those from Spitzer and JWST.

2. Experimental Methods

The irradiation experiments were performed in an ultrahigh vacuum chamber at a pressure of about 10^{-11} Torr, which has been described in detail elsewhere (M. J. Abplanalp et al. 2016a; A. M. Turner & R. I. Kaiser 2020). In the chamber, a polished silver wafer was attached to an oxygen-free high conductivity copper target via indium foil. The copper target was connected to a two-stage closed-cycle helium refrigerator

(CTI-Cryogenics Cryodyne 1020, compressor: CTI-Cryogenics 9600) to generate a cryogenic temperature. This temperature was monitored by a silicon diode sensor (Lakeshore DT-470) and regulated in a range of 5–320 K by a programmable temperature controller (Lakeshore 336). When the silver wafer was cooled to 5.0 ± 0.1 K, the TNO ice analogs were prepared by introducing high-purity methane ($^{13}\text{CH}_4$, 99% atom ^{13}C , Sigma Aldrich), water (H_2O , HPLC, Fisher Chemical), ammonia (NH_3 , 99.9992%, Matheson), carbon monoxide (^{13}CO , 99% atom ^{13}C , Sigma Aldrich), carbon dioxide ($^{13}\text{CO}_2$, 99% atom ^{13}C , Sigma Aldrich), and methanol ($^{13}\text{CH}_3\text{OH}$, Sigma Aldrich, 99.9%) at the pressure of $\sim 3 \times 10^{-8}$ Torr in the chamber, followed by deposition on the wafer via a glass capillary array. The mixed ices were codeposited by using two glass capillary arrays concurrently.

Table 3
Infrared Absorption Features of Water–Methane ($\text{H}_2\text{O}-^{13}\text{CH}_4$) Ice Mixtures before and after Irradiation at 20 and 10 K

20 K		10 K		Assignment	Reference
Before Irradiation	After Irradiation	Before Irradiation	After Irradiation		
Position (cm^{-1})					
6715	...	6763	...	$2v_1/2v_3 (\text{H}_2\text{O})$	(1, 2, 3, 4, 5)
5966	...	5966	...	$2v_3 (^{13}\text{CH}_4)$	(6, 7)
5780	...	5781	...	$v_1 + v_3 (^{13}\text{CH}_4)$	(6, 7)
5536	...	5539	...	$v_3 + 2v_4 (^{13}\text{CH}_4)$	(6, 7)
5292	...	5285	...	$v_{\text{d}(\text{O}-\text{H})} + v_1 + v_2/v_{\text{d}(\text{O}-\text{H})} + v_2 + v_3 (\text{H}_2\text{O})$	(1, 2, 3, 4, 5)
5085	5099	5098	5107	$v_1 + v_3/v_2 + v_3 (\text{H}_2\text{O})$	(1, 2, 3, 4, 5)
...	4743, 4661	?	...
4520	4516	4520	4520	$v_2 + v_3 (^{13}\text{CH}_4)$	(6, 7)
...	4387	$^{13}\text{CH}_3\text{OH}$ combination	...
4282	4282	4282	4283	$v_3 + v_4 (^{13}\text{CH}_4)$	(6, 7)
4193	4195	4194	4194	$v_1 + v_4 (^{13}\text{CH}_4)$	(6, 7)
3684, 3660	...	3683, 3660	...	$v_{\text{d}(\text{O}-\text{H})}$	(1, 2, 3, 4, 5)
...	3620	...	3619	$v_1 + v_3 (^{13}\text{CO}_2)$	(9, 10)
3403, 3288, 3261, 3198	...	3388, 3294, 3239, 3205	...	$v_1/v_3 (\text{H}_2\text{O})$	(1, 2, 3, 4, 5)
...	3633, 3464, 3391, 3289, 3133	...	3636, 3453, 3391, 3274, 3128	O–H stretch	(13)
2999	3000	2999	2999	$v_3 (^{13}\text{CH}_4)$	(6, 7)
...	2963, 2930, 2903, 2870, 2823	...	2966, 2901, 2877, 2815, 2734	$^{13}\text{C}-\text{H}$ stretch	(13)
2901	...	2901	...	$v_1 (^{13}\text{CH}_4)$	(6, 7)
2808	...	2808	...	$v_2 + v_4 (^{13}\text{CH}_4)$	(6, 7)
...	2342	...	2341	$v_3 (\text{CO}_2)$	(9, 10)
...	2275	...	2275	$v_3 (^{13}\text{CO}_2)$	(9, 10)
2578	...	2579	...	$2v_4 (^{13}\text{CH}_4)$	(6, 7)
2206	...	2205	...	$v_2 + v_L (\text{H}_2\text{O})$	(1, 2, 3, 4, 5)
...	2091	...	2090	$v_1 (^{13}\text{CO})$	(8, 10)
...	1677, 1581	...	1679, 1569	$^{13}\text{C}=\text{O}$ stretch	(13)
1655	1657	1653	1657	$v_2 (\text{H}_2\text{O})$	(1, 2, 3, 4, 5)
...	1499	...	1499	$v_3 (\text{H}_2^{13}\text{CO})$	(11)
...	1460, 1426, 1277	...	1460, 1426, 1277	O–H/ $^{13}\text{C}-\text{H}$ deformation	(13)
1293	1294	1293	1294	$v_4 (^{13}\text{CH}_4)$	(6, 7)
...	1001	...	1003	$^{13}\text{C}-\text{O}$ stretch	(12, 13)
...	835	...	843	$^{13}\text{C}-\text{H}$ out-of-plane bending	(13)
805	...	803	...	$v_L (\text{H}_2\text{O})$ libration	(1, 2, 3, 4, 5)

Note. ? in column (5) means these peaks are difficult to assign.

References. (1) W. Zheng et al. (2009b); (2) W. Zheng et al. (2006a); (3) V. Buch & J. P. Devlin (1991); (4) C. M. Tonauer et al. (2021); (5) P. D. Tribbett et al. (2021); (6) M. J. Abplanalp et al. (2018); (7) C. J. Bennett et al. (2006); (8) C. J. Bennett et al. (2009); (9) P. A. Gerakines & R. L. Hudson (2015); (10) H. Carrascosa et al. (2019); (11) M. M. Wohar & P. W. Jagodzinski (1991); (12) C. Zhang et al. (2024); (13) G. Socrates (2004).

Here, we used carbon-13 labeled reactants to eliminate potential contaminants. The thickness (d) of each ice system was determined with Equation (1) (O. S. Heavens 1955; A. M. Turner et al. 2015), where N is the number of interference fringes recorded during the ice deposition by a helium-neon laser (CVI Melles-Griot, 25-LHP-230, 632.8 nm), n is the ice’s refractive index at 632.8 nm, and $\theta = 4^\circ$ is the angle of incidence:

$$d = \frac{N\lambda}{2\sqrt{n^2 - \sin^2 \theta}}. \quad (1)$$

The thickness of each ice was controlled to be 850 ± 50 nm by monitoring the number of fringes during deposition (A. M. Turner et al. 2015). The refractive indices used here

are as follows: water (1.27 ± 0.02), methane (1.34 ± 0.04), ammonia (1.33 ± 0.01), carbon monoxide (1.292 ± 0.003), carbon dioxide (1.27 ± 0.02), and methanol (1.296 ± 0.005) (M. Bouilloud et al. 2015; R. L. Hudson et al. 2020; R. L. Hudson et al. 2022, 2024; P. A. Gerakines et al. 2023). The refractive indices of binary ice mixtures were derived by averaging the refractive index of two components. After deposition, ices were warmed to 40, 20, and 10 K, respectively, at a ramping rate of 1 K minute^{-1} (L. A. Young et al. 2020; S. M. Menten et al. 2022). Then, the ices were isothermally processed by 5 keV energetic electrons (Specs EQ 22/35 electron source) to simulate the secondary electrons formed in the track of GCRs penetrating into the surfaces of TNOs. The electron incidence angle was 70° to the ice surface normal. Utilizing Monte Carlo simulations

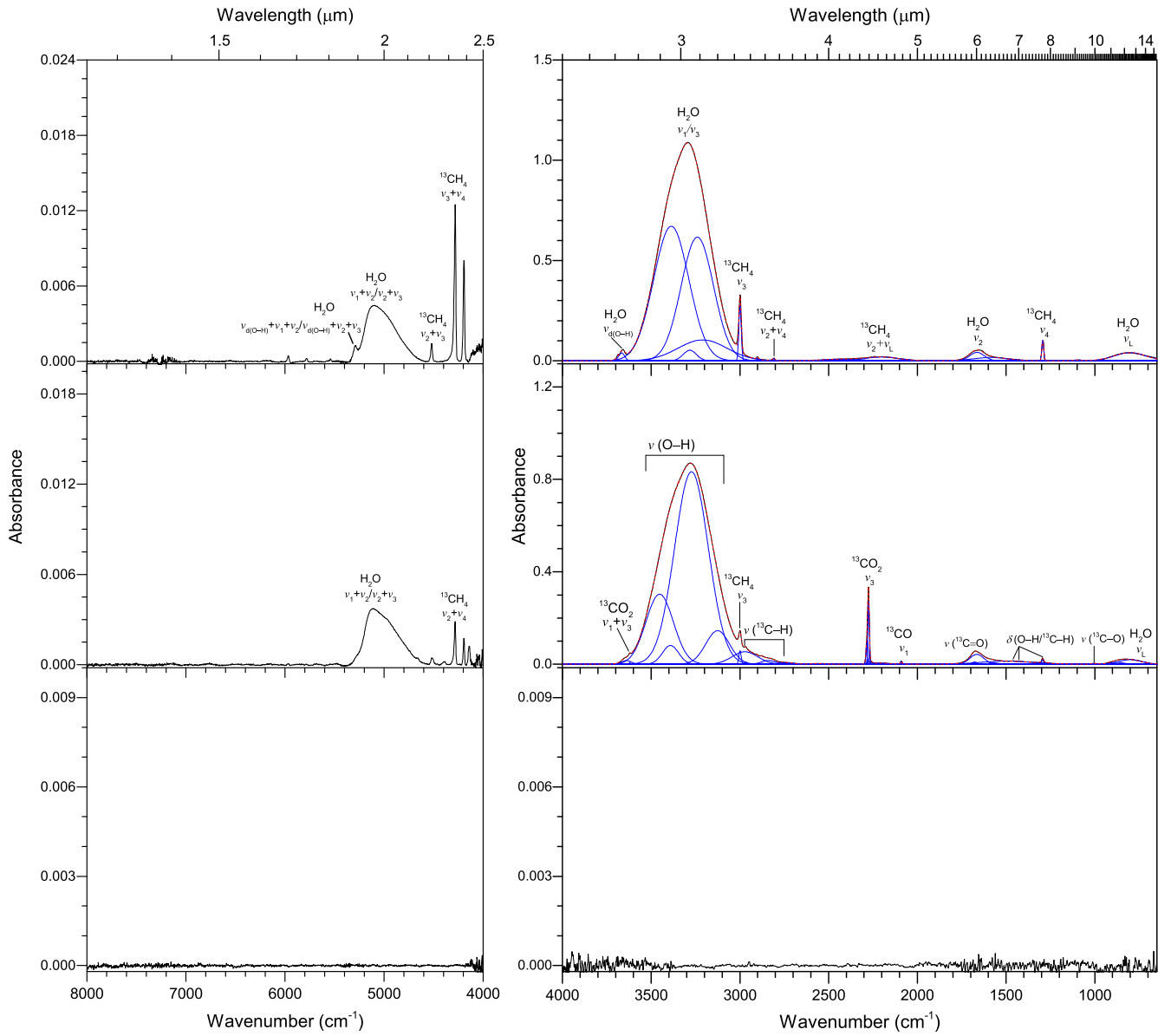


Figure 7. Infrared spectra of water–methane (H_2O – $^{13}\text{CH}_4$) ice mixtures before (top) and after (middle) irradiation at 10 K. The infrared spectra of the irradiated sample warmed up to 320 K are shown at the bottom. The experimental spectra are plotted in black, the deconvoluted peaks are in blue, and the sums are in red. Only noticeable peaks are labeled for clarity, and detailed peak assignments are listed in Table 3. L indicates libration.

Table 4
Infrared Absorption Features of Water–Ammonia (H_2O – NH_3) Ice Mixtures before and after Irradiation at 40 and 10 K

40 K		10 K		Assignment	Reference
Before Irradiation	After Irradiation	Before Irradiation	After Irradiation		
Position (cm^{-1})					
6801	...	6793	...	$2v_1/2v_3$ (H_2O)	(1, 2, 3, 4)
6581	...	6582	...	$2v_1$ (NH_3)	(5, 6, 7)
5105	5101	5109	5107	$v_1 + v_3/v_2 + v_3$ (H_2O)	(1, 2, 3, 4)
5015	5016	5016	5016	$v_3 + v_4$ (NH_3)	(5, 6, 7)
4522	4537	4525	4534	$v_2 + v_3$ (NH_3)	(5, 6, 7)
...	4141	...	4140	$v_1/v_3 + v_L$ (H_2O)	(1, 2, 3, 4)
3699	...	3698	...	$v_{d(\text{O}-\text{H})}$	(1, 2, 3, 4)
3384	3382	3382	3380	v_3 (NH_3)	(5, 6, 7)
3434, 3265, 3236, 3128, 2891	3245, 3212	3471, 3291, 3254, 3135, 2896	3414, 3246, 3232	v_1/v_3 (H_2O)	(1, 2, 3, 4)
2921	2923	2921	2921	$\text{H}_2\text{O} \cdot \text{NH}_3$ complex	(7, 8, 9)
2444	2448	2451	2452	N–H ⁺ stretch	(7, 8, 9)

Table 4
(Continued)

40 K		10 K		Assignment	Reference
Before Irradiation	After Irradiation	Before Irradiation	After Irradiation		
Position (cm^{-1})					
2230	2213	2227	2179	$v_2 + v_L (\text{H}_2\text{O})$	(1, 2, 3, 4)
...	1699	...	1700	N–H deformation	(7, 8, 9)
1660	1646	1662	1662	$v_2 (\text{H}_2\text{O})$	(1, 2, 3, 4)
1630	...	1636	...	$v_4 (\text{NH}_3)$	(5, 6, 7)
1111	1122	1111	1121	$v_2 (\text{NH}_3)$	(5, 6, 7)
805	837	803	837	$v_L (\text{H}_2\text{O})$ libration	(1, 2, 3, 4)

References. (1) W. Zheng et al. (2009b); (2) W. Zheng et al. (2006a); (3) V. Buch & J. P. Devlin (1991); (4) C. M. Tonauer et al. (2021); (5) J. S. Holt et al. (2004); (6) W. Zheng et al. (2008); (7) W. Zheng et al. (2009a); (8) W. Zheng & R. I. Kaiser (2010); (9) G. Socrates (2004).

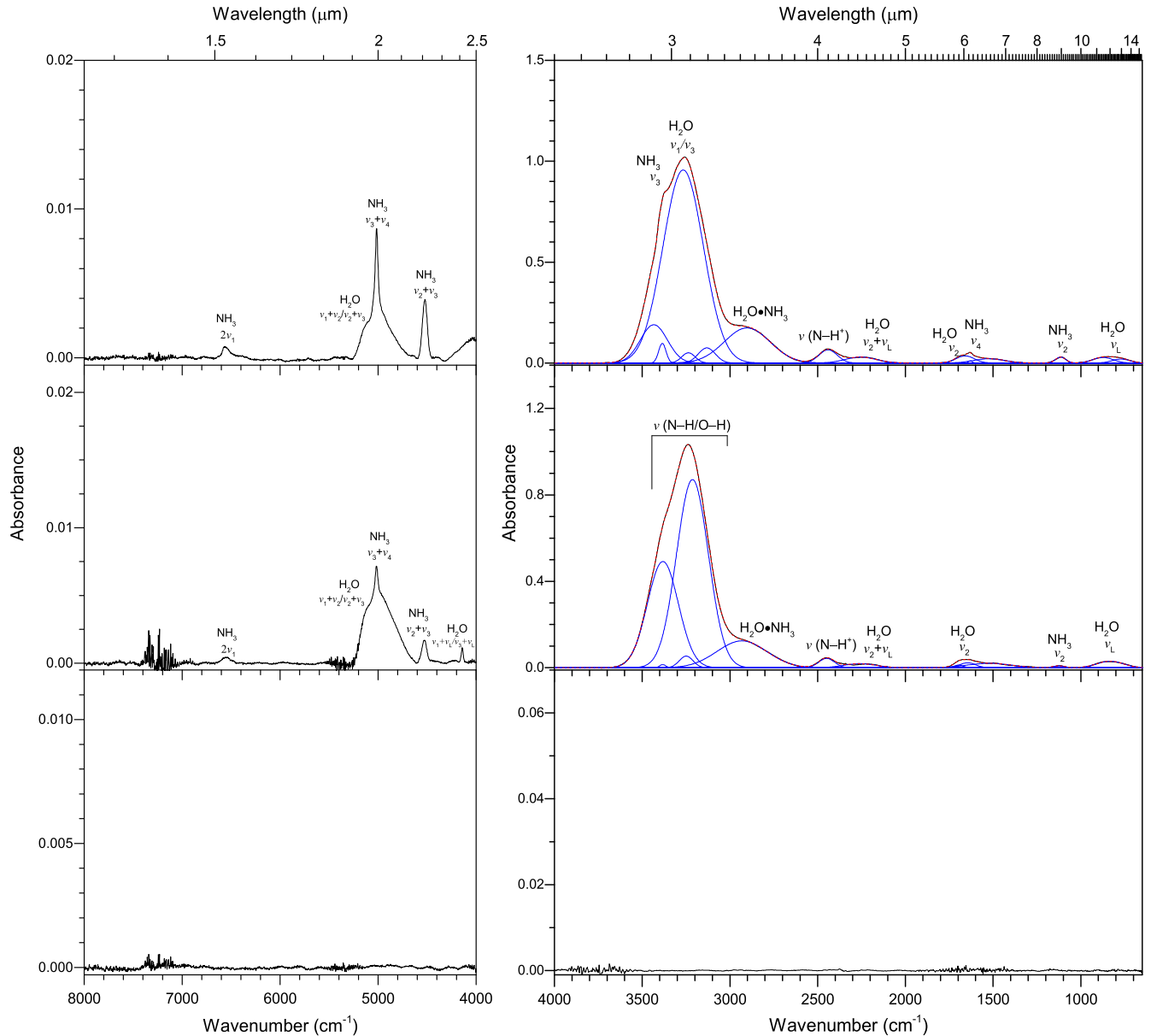


Figure 8. Infrared spectra of water–ammonia ($\text{H}_2\text{O}-\text{NH}_3$) ice mixtures before (top) and after (middle) irradiation at 40 K. The infrared spectra of the irradiated sample warmed up to 320 K are shown at the bottom. The experimental spectra are plotted in black, the deconvoluted peaks are in blue, and the sums are in red. Only noticeable peaks are labeled for clarity, and detailed peak assignments are listed in Table 4. L indicates libration.

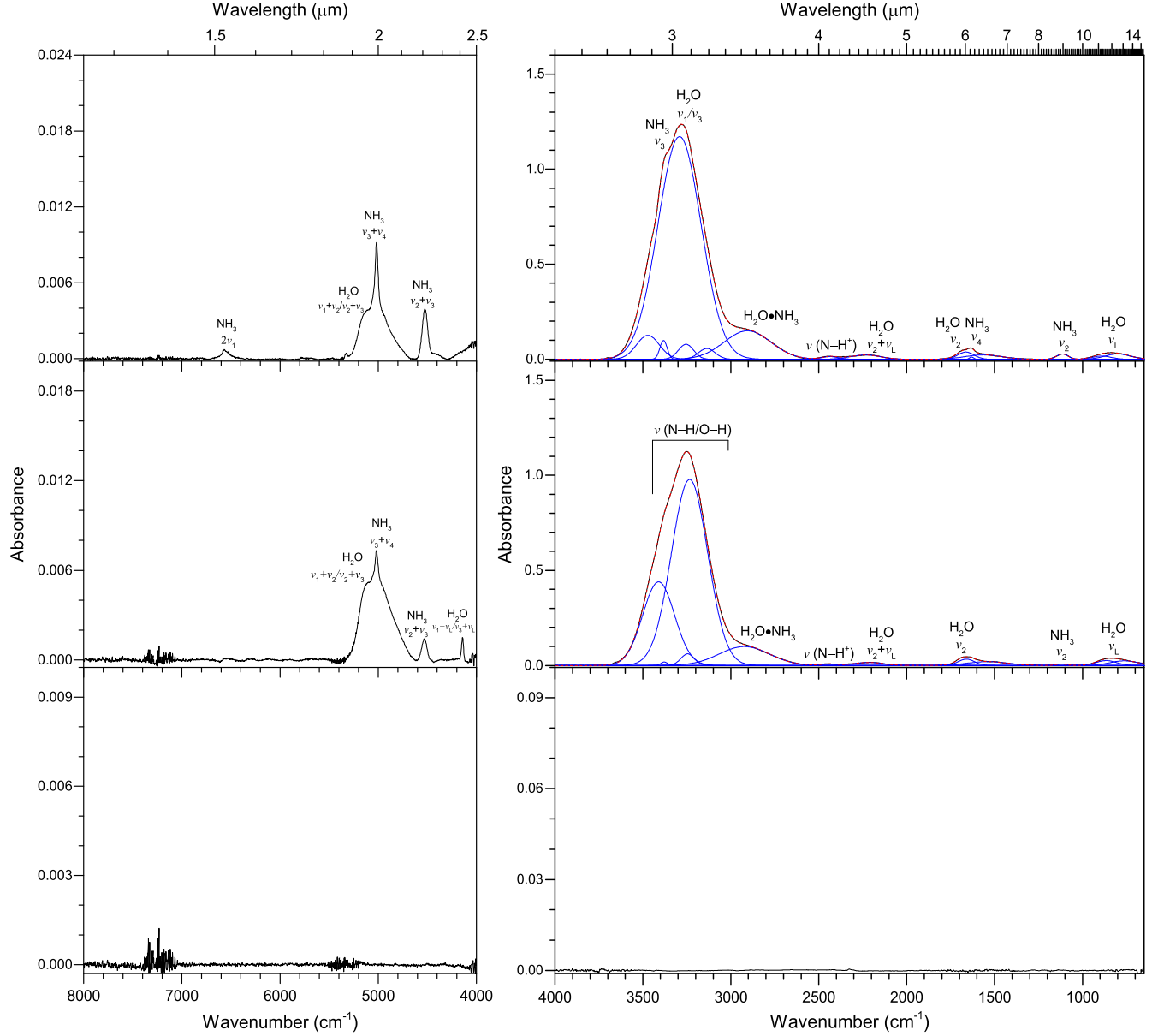


Figure 9. Infrared spectra of water–ammonia ($\text{H}_2\text{O}-\text{NH}_3$) ice mixtures before (top) and after (middle) irradiation at 10 K. The infrared spectra of the irradiated sample warmed up to 320 K are shown at the bottom. The experimental spectra are plotted in black, the deconvoluted peaks are in blue, and the sums are in red. Only noticeable peaks are labeled for clarity, and detailed peak assignments are listed in Table 4. L indicates libration.

Table 5
Infrared Absorption Features of Water–Carbon Monoxide ($\text{H}_2\text{O}-^{13}\text{CO}$) Ice Mixtures before and after Irradiation at 20 and 10 K

20 K			10 K			Assignment	Reference
Before Irradiation	After Irradiation	Residue at 320 K	Before Irradiation	After Irradiation			
Position (cm^{-1})							
5271	5264	...	5250	5255	$v_{d(\text{O}-\text{H})} + v_1 + v_2/v_{d(\text{O}-\text{H})} + v_2 + v_3$ (H_2O)	(1, 2, 3)	
5080	5128	...	5069	5104	$v_1 + v_3/v_2 + v_3$ (H_2O)	(1, 2, 3)	
...	4979	$2v_1 + v_3$ ($^{13}\text{CO}_2$)	(5, 6, 8)	
...	4870	$v_1 + 2v_2 + v_3$ ($^{13}\text{CO}_2$)	(5, 6, 8)	
...	4517	4673, 4515	?	...	
...	4284	$v_3 + v_4$ ($^{13}\text{CH}_4$),	(8, 9)	
4158	4160	...	4156	...	$2v_1$ (^{13}CO)	(7, 8, 11)	
...	4145	$v_1/v_3 + v_L$ (H_2O)	(1, 2, 3, 4)	
3655	3621	...	$v_{d(\text{O}-\text{H})}$	(1, 2, 3)	

Table 5
(Continued)

Before Irradiation	20 K		10 K		Assignment	Reference
	After Irradiation	Residue at 320 K	Before Irradiation	After Irradiation		
	Position (cm^{-1})					
...	3621	3622	$v_1 + v_3 (^{13}\text{CO}_2)$...
3426, 3273	3401, 3242	...	$v_1/v_3 (\text{H}_2\text{O})$	(1, 2, 3)
...	3649, 3527, 3404, 3239, 3098	3447, 3418, 3207, 3026	...	3647, 3443, 3381, 3264, 3229, 3126	O–H stretch	(8, 11)
...	2984, 2841, 2726, 2566	2959, 2926, 2866	...	2973, 2828, 2544	^{13}C –H stretch	(8, 11)
...	2346	2344	$v_3 (\text{CO}_2)$	(5, 6, 8)
...	2273	2272	$v_3 (^{13}\text{CO}_2)$	(5, 6, 8)
2204	2201	...	$v_2 + v_L (\text{H}_2\text{O})$	(1, 2, 3)
...	2166	$^{13}\text{C} \equiv ^{13}\text{C}$ stretch	(7, 8, 11)
2139	2139	...	$v_1 (\text{CO})$	(6, 7, 8, 11)
2090	2090	...	2090	2090	$v_1 (^{13}\text{CO})$	(6, 7, 8, 11)
2039	2038	...	2038	2038	$v_1 (^{13}\text{C}^{18}\text{O})$	(6, 7, 8, 11)
...	1680, 1675, 1633, 1596	1736, 1705	...	1680, 1667, 1621	$^{13}\text{C}=\text{O}$ stretch	(8, 11)
1638	1651	...	$v_2 (\text{H}_2\text{O})$	(1, 2, 3)
...	1499	1499	$v_3 (\text{H}_2^{13}\text{CO})$	(8, 10)
...	1458, 1371, 1274	1507	...	1457, 1476, 1417, 1269, 1201	O–H/ ^{13}C –H deformation	(8, 11)
...	1295	$v_4 (^{13}\text{CH}_4)$	(8, 9)
...	1010	1121, 1000	^{13}C –O stretch	(8, 11)
780	797	...	$v_L (\text{H}_2\text{O})$ libration	(1, 2, 3)

Note. The bands in the residue that remained after the irradiated ice warmed up to 320 K are also listed. ? in column (6) means these peaks are difficult to assign.

References. (1) W. Zheng et al. (2009b); (2) W. Zheng et al. (2006a); (3) V. Buch & J. P. Devlin (1991); (4) C. M. Tonauer et al. (2021); (5) P. A. Gerakines & R. L. Hudson (2015); (6) H. Carrascosa et al. (2019); (7) C. J. Bennett et al. (2009); (8) A. M. Turner et al. (2021a); (9) C. J. Bennett et al. (2006); (10) M. M. Wohar & P. W. Jagodzinski (1991); (11) G. Socrates (2004).

Table 6
Infrared Absorption Features of Water–Carbon Dioxide ($\text{H}_2\text{O}–^{13}\text{CO}_2$) Ice Mixtures before and after Irradiation at 40 and 10 K

Before Irradiation	40 K		10 K		Assignment	Reference
	After Irradiation	Before Irradiation	After Irradiation	After Irradiation		
	Position (cm^{-1})					
6750	...	6735	$2v_1/2v_3 (\text{H}_2\text{O})$	(1, 2, 3, 4)
5279	...	5277	5256	$v_{d(\text{O}-\text{H})} + v_1 + v_2/v_{d(\text{O}-\text{H})} + v_2 + v_3 (\text{H}_2\text{O})$	(1, 2, 3, 4)	
5101	5104	5088	5104	$v_1 + v_3/v_2 + v_3 (\text{H}_2\text{O})$	(1, 2, 3, 4)	
4981	4983	4979	4977	$2v_1 + v_3 (^{13}\text{CO}_2)$	(5, 6)	
4871	4876	4875	4871	$v_1 + 2v_2 + v_3 (^{13}\text{CO}_2)$	(5, 6)	
3649	...	3651	...	$v_{d(\text{O}-\text{H})}$	(1, 2, 3, 4)	
3624	3623	3624	3623	$v_1 + v_3 (^{13}\text{CO}_2)$	(5, 6)	
3426, 3273	...	3401, 3242	...	$v_1/v_3 (\text{H}_2\text{O})$	(1, 2, 3, 4)	
...	3632, 3479, 3396, 3244, 3118	...	3635, 3485, 3386, 3256	O–H stretch	(8, 9)	
...	2934, 2588, 2551	...	2932, 2597, 2578	^{13}C –H stretch	(8, 9)	
2348	2349	2344	2351	$v_3 (\text{CO}_2)$	(5, 6)	
2271	2271	2270	2269	$v_3 (^{13}\text{CO}_2)$	(5, 6)	
2206	...	2207	...	$v_2 + v_L (\text{H}_2\text{O})$	(1, 2, 3, 4)	
...	2092	...	2092	$v_1 (^{13}\text{CO})$	(6, 7)	
...	1665, 1566	...	1655, 1563	$^{13}\text{C}=\text{O}$ stretch	(8, 9)	
1645	...	1643	...	$v_2 (\text{H}_2\text{O})$	(1, 2, 3, 4)	
...	1473, 1371, 1282	...	1467, 1371, 1281	O–H/ ^{13}C –H deformation	(8, 9)	
805	831	803	832	$v_L (\text{H}_2\text{O})$ libration	(1, 2, 3, 4)	
640	...	646	...	$v_2 (^{13}\text{CO}_2)$	(5, 6)	

References. (1) W. Zheng et al. (2009b); (2) W. Zheng et al. (2006a); (3) V. Buch & J. P. Devlin (1991); (4) C. M. Tonauer et al. (2021); (5) P. A. Gerakines & R. L. Hudson (2015); (6) H. Carrascosa et al. (2019); (7) C. J. Bennett et al. (2009); (8) W. Zheng & R. I. Kaiser (2007b); (9) G. Socrates (2004).

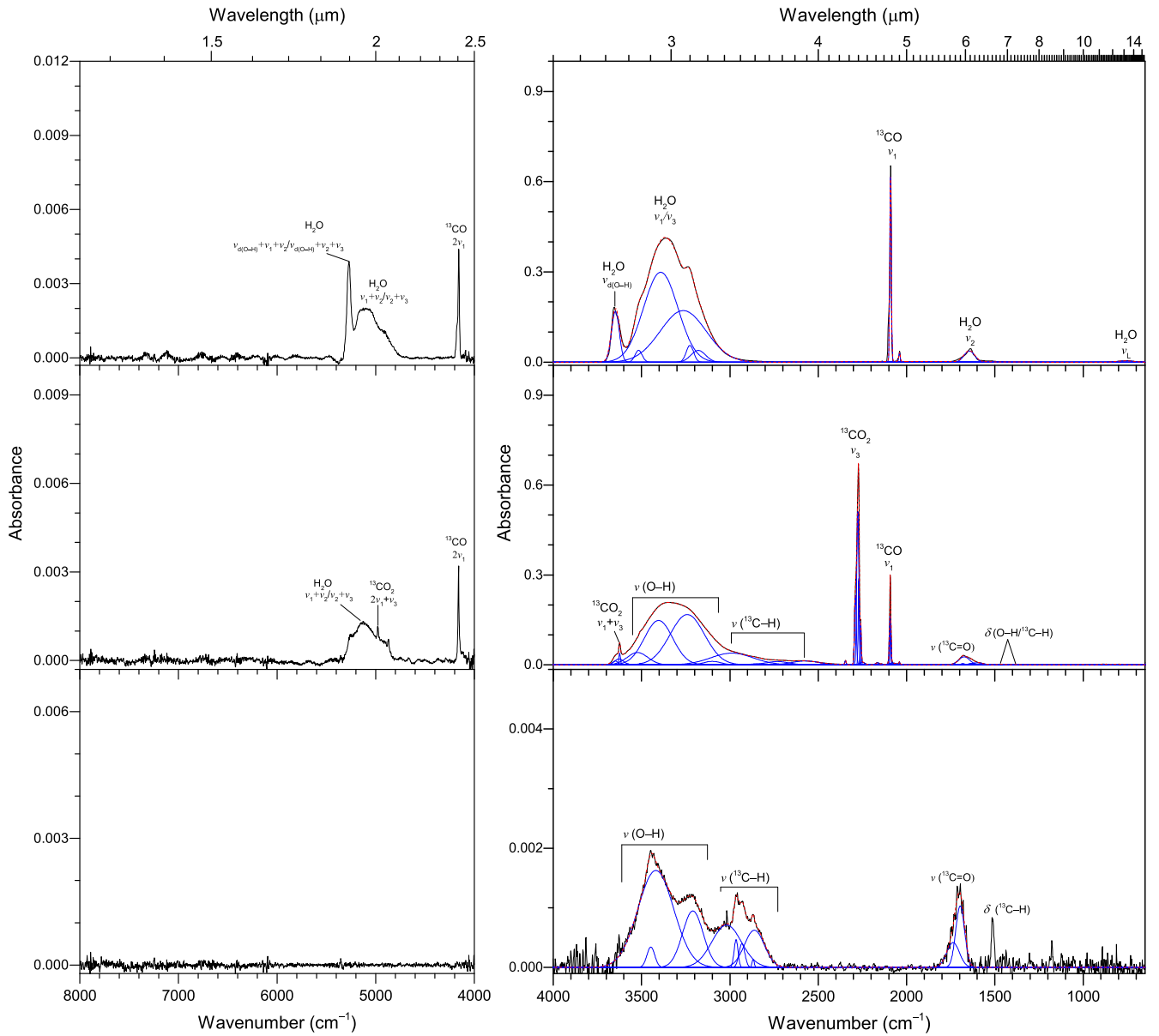


Figure 10. Infrared spectra of water–carbon monoxide (H_2O – ^{13}CO) ice mixtures before (top) and after (middle) irradiation at 20 K. The infrared spectra of the irradiated sample warmed up to 320 K are shown at the bottom. The experimental spectra are plotted in black, the deconvoluted peaks are in blue, and the sums are in red. Only noticeable peaks are labeled for clarity, and detailed peak assignments are listed in Table 5. L and d indicate libration and dangling, respectively.

(CASINO 2.42; D. Drouin et al. 2007), the maximum depths of the electron penetration were determined to be around 600 ± 50 nm, which is less than the ice thickness of 850 ± 50 nm, thus avoiding interaction between high-energy electrons and the silver wafer. The dose accumulation within processed ices was controlled to be 82 ± 10 eV amu $^{-1}$ (C. Zhang et al. 2023b, 2024). Note that, to enable a comparison between our results and the dose accumulation of the TNO surface, we used the unit of the deposited dose in eV amu $^{-1}$, which is widely adopted in the astronomy community (C. J. Bennett et al. 2013; A. Yeghikyan 2017; E. Quirico et al. 2023). This unit can be converted to eV molecule $^{-1}$, used in the astrochemistry community by multiplying the units of eV amu $^{-1}$ by the molecular mass of the reactants, e.g., 18 amu molecule $^{-1}$ for water. Objects in the TNO space undergo continuous exposure to ionizing radiation including

ultraviolet (UV) photons, charged particles originating from solar winds, and GCRs (R. E. Johnson 1991; J. F. Cooper et al. 2003). Among those sources of ionizing radiation, charged particles consist of some 90% protons (H^+) and 1%–10% helium nuclei (He^{2+}), with solar wind particles typically having energies in the range of a few keV and GCR particles reaching energies in the hundreds of MeV (R. E. Johnson 1990; G. J. Golabek & M. Jutzi 2021). The UV radiation exhibits a flux of about 10^3 photons cm $^{-2}$ s $^{-1}$ with energies lower than 20.0 eV (S. S. Prasad & S. P. Tarafdar 1983). The chemistry of small TNO surfaces is predominantly controlled by secondary electrons, generated by ionizing radiation penetrating ices. Essentially, implanted protons transfer their kinetic energy to the electronic system of target molecules, leading to the generation of electrons with energies up to a few keV (G. Strazzulla et al. 2003; C. J. Bennett et al. 2005). The

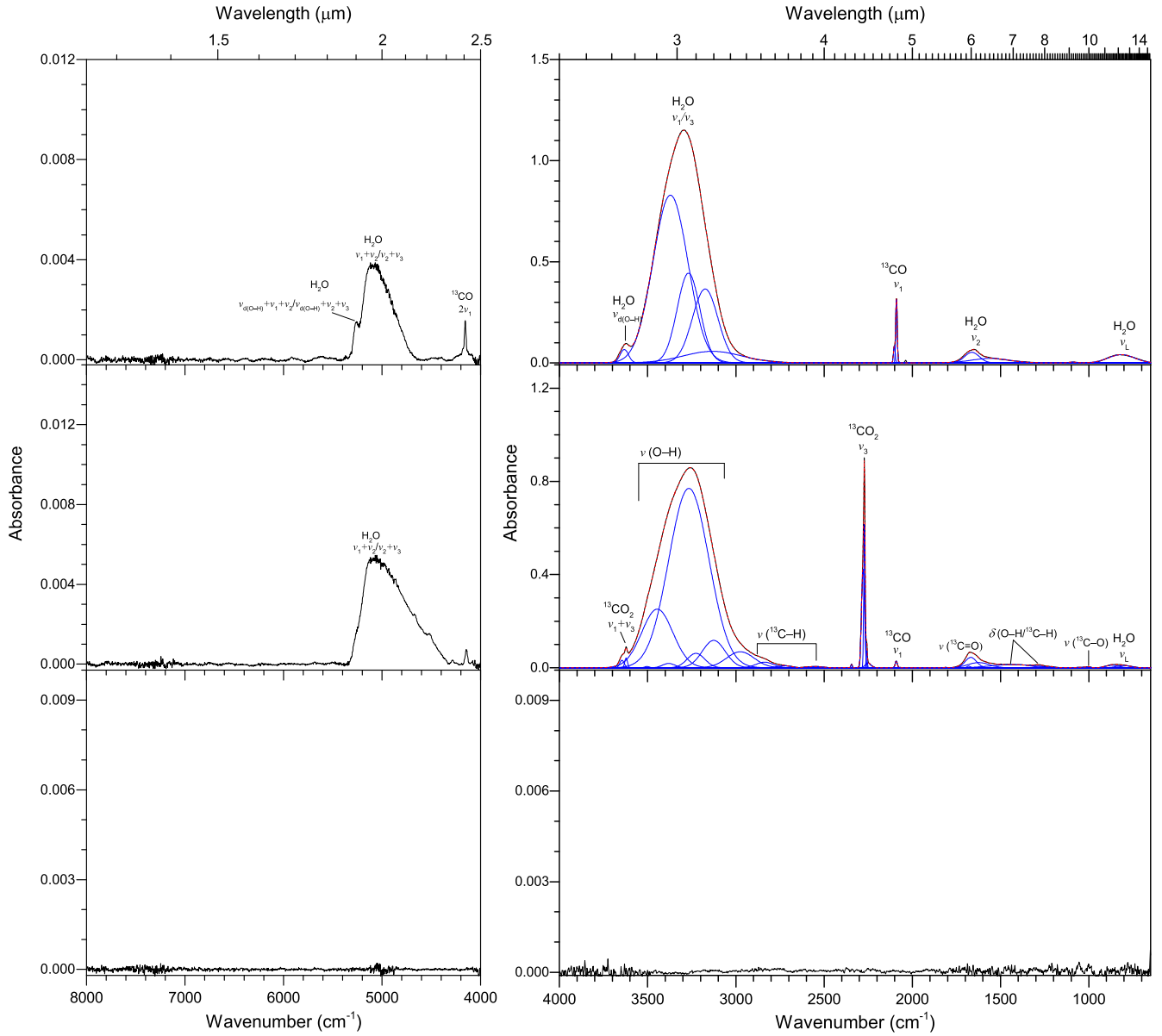


Figure 11. Infrared spectra of water–carbon monoxide (H_2O – ^{13}CO) ice mixtures before (top) and after (middle) irradiation at 10 K. The infrared spectra of the irradiated sample warmed up to 320 K are shown at the bottom. The experimental spectra are plotted in black, the deconvoluted peaks are in blue, and the sums are in red. Only noticeable peaks are labeled for clarity, and detailed peak assignments are listed in Table 5. L and d indicate libration and dangling, respectively.

electronic linear energy transfer of MeV protons to molecules within such ices exhibits a similar value of a few keV μm^{-1} as the 5 keV electrons used in the present experiments (B. M. Jones & R. I. Kaiser 2013). In addition, previous research has shown that the classes of irradiation products from interstellar ices is weakly dependent on the type of radiation source, whether electrons, heavy ions, or UV photons (G. A. Baratta et al. 2002; G. M. Muñoz Caro et al. 2014; M. J. Abplanalp et al. 2018; C. R. Arumainayagam et al. 2019), even though different radiation sources can lead to various relative abundances of products from irradiated interstellar ices (G. M. Muñoz Caro et al. 2014; D. V. Mifsud et al. 2023). Our laboratory experiments mimic the formation of complex products in molecular ices at low temperatures through charged particles via electronic energy-loss processes on airless TNOs.

After the irradiation, temperature-programmed desorption studies were carried out by heating the irradiated ices to 320 K at a rate of 1 K min^{-1} . The functional groups involved in ices and radiolysis products were analyzed by a Fourier transform infrared (FTIR) spectrometer (Thermo Fisher Scientific, Nicolet 6700 Spectrometer, liquid nitrogen-cooled MCTB detector). The FTIR spectrometer was operated in the absorption–reflection–absorption mode with a reflection angle of 45° and monitored the infrared signals in the range of 6000–650 cm^{-1} (1.67–15.38 μm) with a resolution of 4 cm^{-1} . The near-infrared spectra (10,000–2000 cm^{-1} ; 1–5 μm) were also recorded to cover maximum astronomical observations of TNOs. The ratios of mixed ices were obtained by estimating the column densities of individual components from the infrared spectra of pristine ice mixtures through a modified

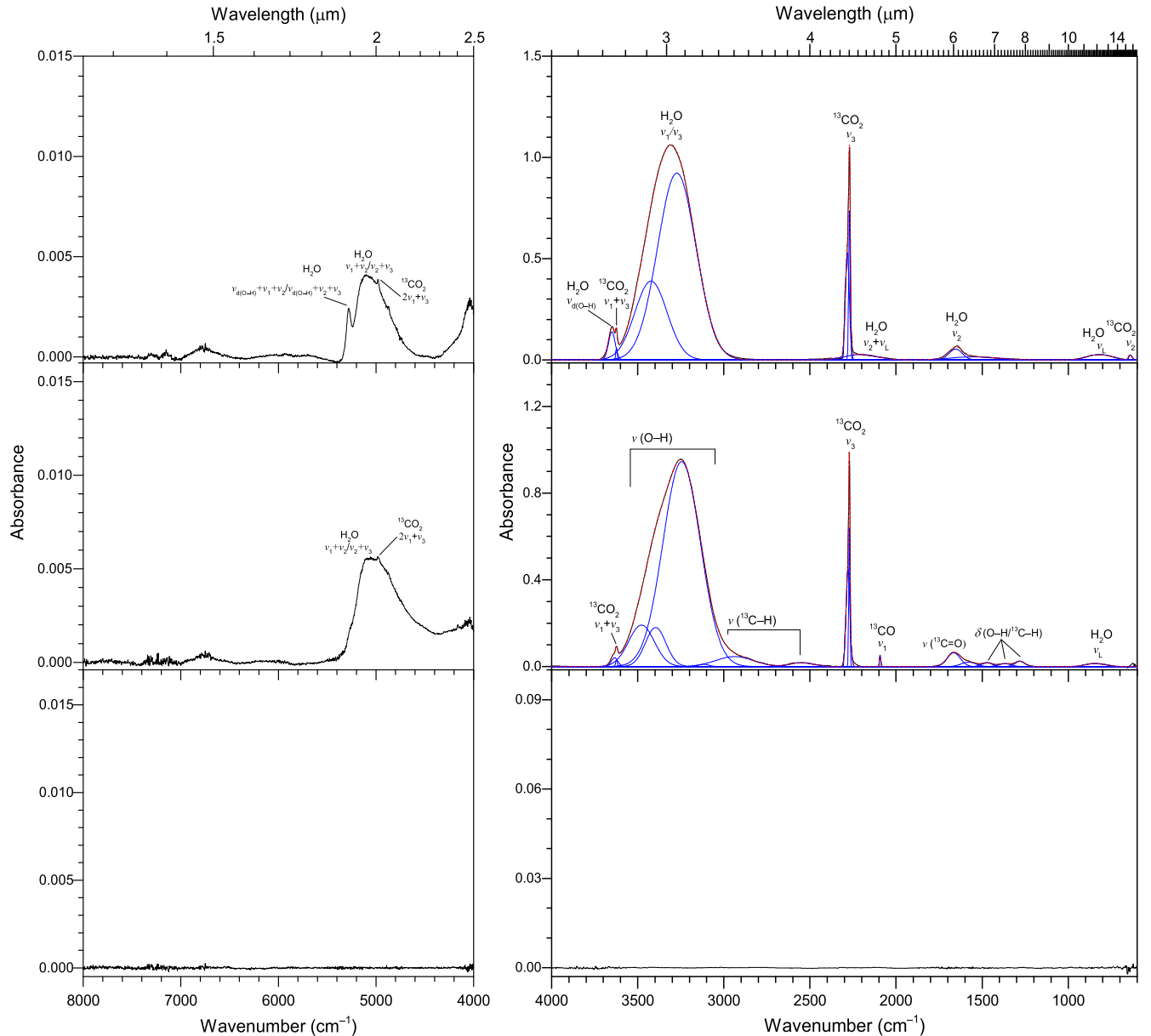


Figure 12. Infrared spectra of water–carbon dioxide (H_2O – $^{13}\text{CO}_2$) ice mixtures before (top) and after (middle) irradiation at 40 K. The infrared spectra of the irradiated sample warmed up to 320 K are shown at the bottom. The experimental spectra are plotted in black, the deconvoluted peaks are in blue, and the sums are in red. Only noticeable peaks are labeled for clarity, and detailed peak assignments are listed in Table 6. L and d indicate libration and dangling, respectively.

Lambert–Beer relationship (J. L. Hollenberg & D. A. Dows 1961; C. J. Bennett et al. 2004). It is important to note that the absorbance of strong bands is not guaranteed to be linear with respect to ice thickness for thicker ice due to the optical interference effect in absorption–reflection–absorption spectroscopy (B. D. Teolis et al. 2007). However, this effect can be circumvented by selecting weak peaks because their band strengths still have a linear relationship with the amount of ice deposited (K. I. Öberg et al. 2009; A. M. Turner et al. 2015). The bands and corresponding absorption coefficients used here are of water (ν_2 at 1664 cm^{-1} , $1.2 \times 10^{-17} \text{ cm molecules}^{-1}$), methane (ν_4 at 1294 cm^{-1} , $8.0 \times 10^{-18} \text{ cm molecules}^{-1}$), ammonia (ν_2 at 1067 cm^{-1} , $1.95 \times 10^{-17} \text{ cm molecules}^{-1}$), carbon monoxide ($2\nu_1$ at 4156 cm^{-1} , $7.4 \times 10^{-20} \text{ cm molecules}^{-1}$), carbon dioxide ($\nu_1 + \nu_3$ at 3624 cm^{-1} , $1.8 \times 10^{-18} \text{ cm molecules}^{-1}$), and

methanol (ν_7 at 1118 cm^{-1} , $1.9 \times 10^{-18} \text{ cm molecules}^{-1}$) (M. Bouilloud et al. 2015; R. L. Hudson et al. 2022, 2024; P. A. Gerakines et al. 2023).

3. Results and Discussion

3.1. Neat Ices

We first present the infrared spectra results of pure H_2O and NH_3 , and the spectra of $^{13}\text{CH}_4$, ^{13}CO , $^{13}\text{CO}_2$, and $^{13}\text{CH}_3\text{OH}$ can be found in our previous reports (C. Zhang et al. 2023b, 2024, 2025b). For the H_2O , before irradiation (ices 1 and 2), both spectra at 40 and 10 K (Figures 2 and 3, Table 2) are dominated by the absorptions of amorphous water, including the broad ν_1/ν_3 bands between 3600 and 3000 cm^{-1} , the asymmetric ν_2 band at

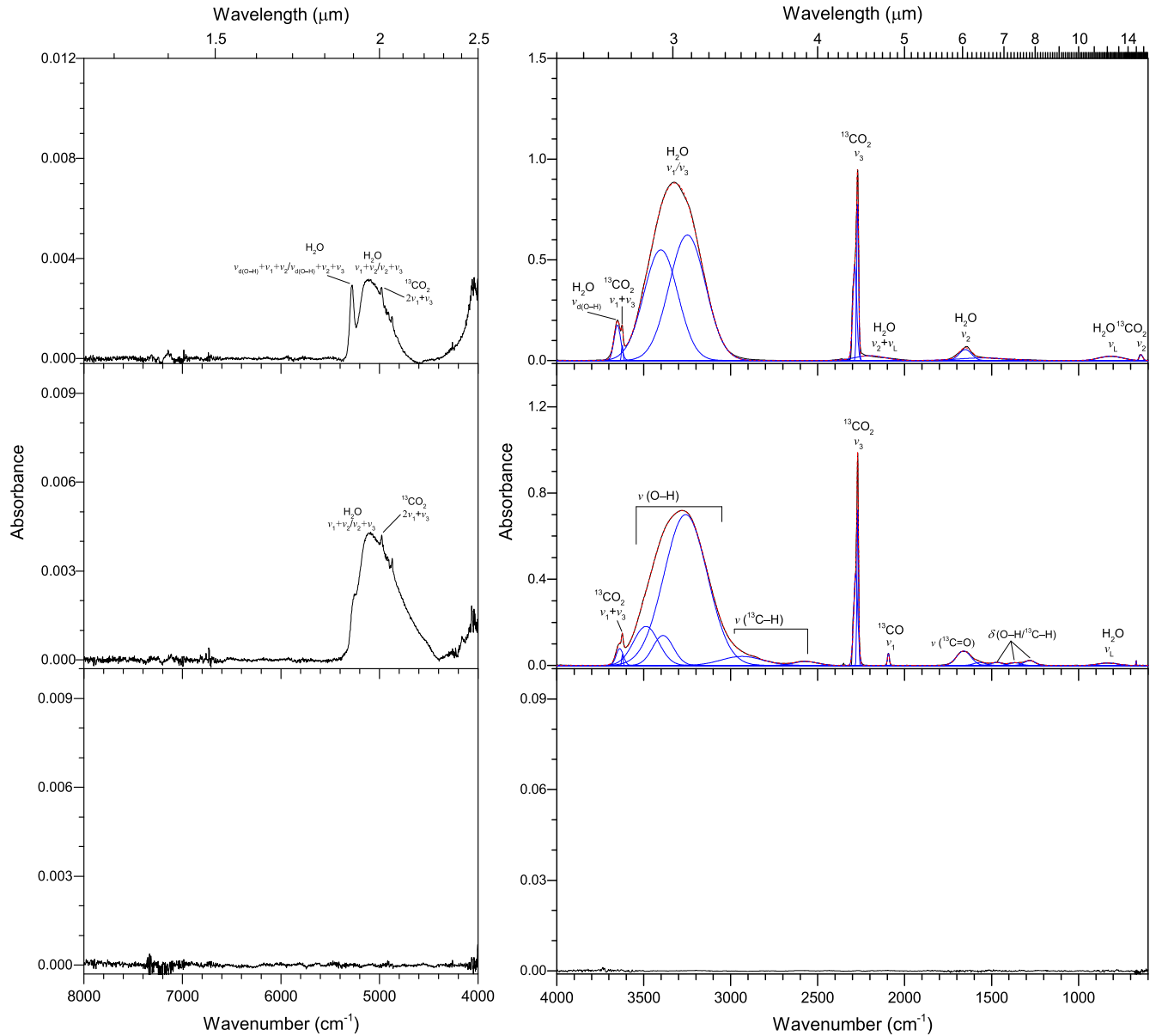


Figure 13. Infrared spectra of water–carbon dioxide (H_2O – $^{13}\text{CO}_2$) ice mixtures before (top) and after (middle) irradiation at 10 K. The infrared spectra of the irradiated sample warmed up to 320 K are shown at the bottom. The experimental spectra are plotted in black, the deconvoluted peaks are in blue, and the sums are in red. Only noticeable peaks are labeled for clarity, and detailed peak assignments are listed in Table 6. L and d indicate libration and dangling, respectively.

1664 cm^{-1} , the ν_L band at 802 cm^{-1} , the overtone $2\nu_1/2\nu_3$ between 7200 and 6000 cm^{-1} , and the combination modes $\nu_1 + \nu_2/\nu_3 + \nu_2$ at 5075 cm^{-1} and $\nu_2 + \nu_L$ at around 2208 cm^{-1} (W. Zheng et al. 2009b; T. Bartels-Rausch et al. 2012; E. F. van Dishoeck et al. 2013; C. M. Tonauer et al. 2021). Weak absorptions from dangling OH bonds at 3716 and 3693 cm^{-1} corresponding to the two-coordinated and three-coordinated oxygen atoms are also observed (V. Buch & J. P. Devlin 1991; J. A. Noble et al. 2024). After irradiation, the one new band at 2851 cm^{-1} belongs to H_2O_2 (W. Zheng et al. 2006a). However, this band is not observable in the 40 K spectrum (ice 1) since the higher irradiation temperature can decrease the yield of H_2O_2 product and lead to an amount lower than the detection limitation (W. Zheng et al. 2006b). No residue appears in the 320 K spectrum because all products

sublimate with solid water at about 180 K (W. Zheng et al. 2006a).

For NH_3 (Figures 4 and 5, Table 2), the fundamental vibration modes appear at 3370 cm^{-1} (ν_3), 3212 cm^{-1} (ν_1), 1626 cm^{-1} (ν_4), and 1074 cm^{-1} (ν_2) along with the overtone at 6514 cm^{-1} ($2\nu_1$), and the combination modes at 6100 ($\nu_2 + \nu_3 + \nu_4$), 4995 ($\nu_3 + \nu_4$), 4476 ($\nu_2 + \nu_3$), and 4334 ($\nu_1 + \nu_2$) (J. S. Holt et al. 2004; W. Zheng & R. I. Kaiser 2007a; A. Zanchet et al. 2013; J. E. Roser et al. 2021; R. L. Hudson et al. 2022). The irradiated NH_3 at both temperatures presents a significant decrease in absorbance. This suggests that most ammonia molecules are destroyed by energetic electron irradiation to form products such as diazene isomers ($\text{cis}-\text{HN}=\text{NH}$, 3048 cm^{-1} ; $\text{N}=\text{NH}_2$, 2774 cm^{-1}), hydrogen azide (HN_3 , 2087 cm^{-1}), and molecular

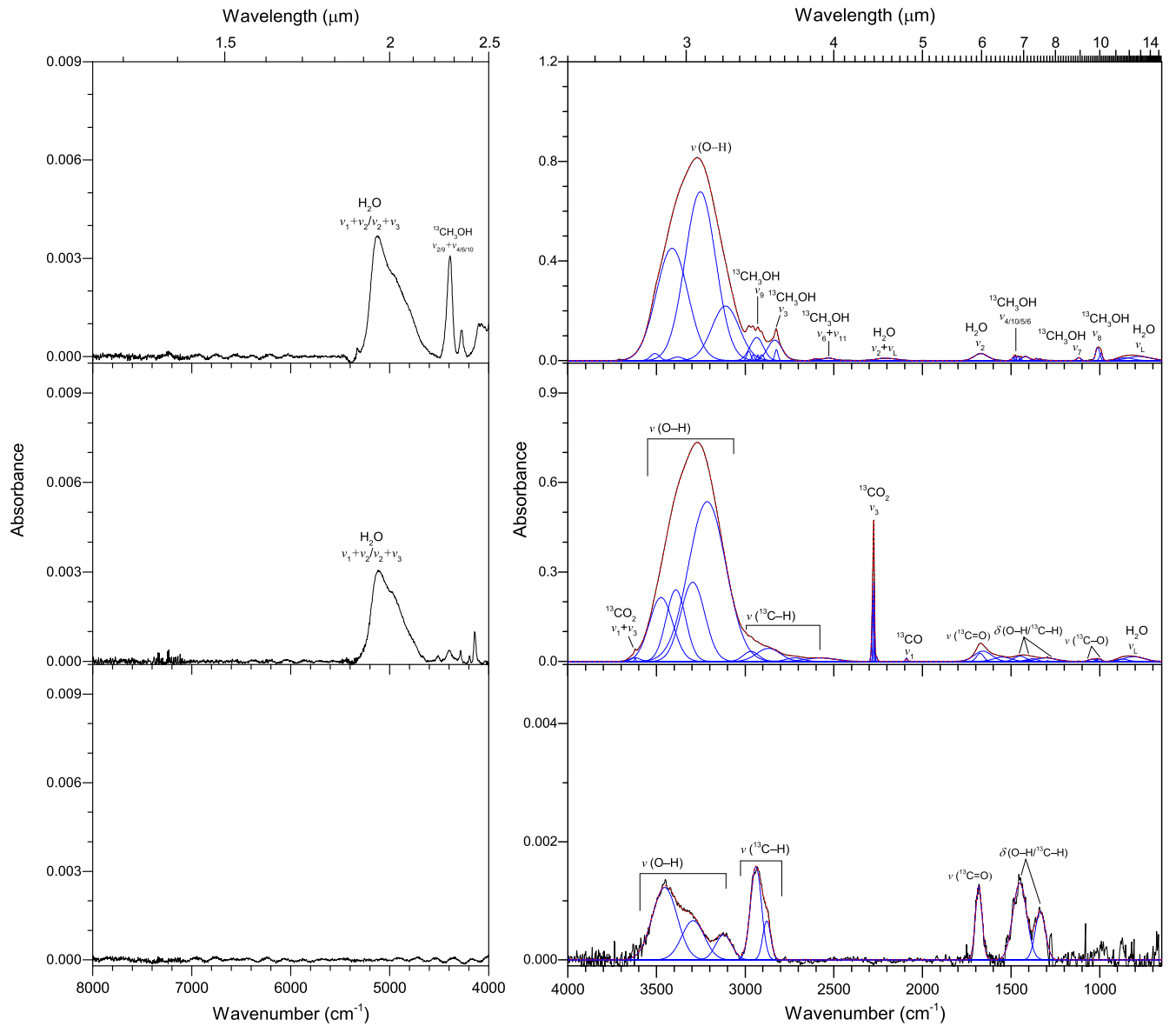


Figure 14. Infrared spectra of water–methanol (H_2O – $^{13}\text{CH}_3\text{OH}$) ice mixtures before (top) and after (middle) irradiation at 40 K. The infrared spectra of the irradiated sample warmed up to 320 K are shown at the bottom. The experimental spectra are plotted in black, the deconvoluted peaks are in blue, and the sums are in red. Only noticeable peaks are labeled for clarity, and detailed peak assignments are listed in Table 7. L indicates libration.

nitrogen (N_2 , 2328 cm^{-1}), as listed in Table 2 (C. S. Jamieson et al. 2005; W. Zheng et al. 2008; P. Parent et al. 2009; M. J. Loeffler & R. A. Baragiola 2010; V. Bordalo et al. 2013; R. Martín-Doménech et al. 2018; D. Torres-Díaz et al. 2024). The presence of hydrazine (N_2H_4) has also been confirmed in the irradiated ammonia ices via mass spectrum without determination here because of the overlap between its bands with ammonia in the infrared spectra (W. Zheng et al. 2008). The N_2 absorption is only observed in the irradiated spectrum at 10 K (ice 4), possibly because this molecule sublimated at 40 K (ice 3; W. Zheng et al. 2011). Similar to water, no residue signal is observed in the 320 K spectra.

3.2. Binary Ice Mixtures

The infrared data of water-bearing binary ice mixtures are shown in Figures 6–15, and the peak assignments are

compiled in Tables 3–7. Adding methane to pure water ice (ices 5 and 6) changes the position of dangling OH bonds from 3716 to 3693 cm^{-1} and 3683 to 3660 cm^{-1} (Figures 6 and 7, Table 3), as supported by M. E. Palumbo (2006), Ó. Gálvez et al. (2009), and J. He et al. (2018). The combination mode $v_{\text{d}(\text{O}-\text{H})} + v_1 + v_2/v_{\text{d}(\text{O}-\text{H})} + v_2 + v_3$ at 5324 shifts to $\sim 5290 \text{ cm}^{-1}$ (P. D. Tribbett et al. 2021). The irradiated ice mixtures appear to produce more complex profiles with identifiable products of carbon dioxide ($^{13}\text{CO}_2$, 2275 cm^{-1}), carbon monoxide (^{13}CO , 2090 cm^{-1}), methanol ($^{13}\text{CH}_3\text{OH}$, $4387/1003 \text{ cm}^{-1}$), and formaldehyde (H_2^{13}CO , 1499 cm^{-1}) along with broad bands of the hydroxyl group ($\text{O}-\text{H}$) between 3700 and 3000 cm^{-1} , the hydrocarbyl group ($^{13}\text{C}-\text{H}$) between 3000 and 2700 cm^{-1} , the carbonyl group ($^{13}\text{C}=\text{O}$) at about 1679 cm^{-1} , and an overlap band of $\text{O}-\text{H}$ bending and $^{13}\text{C}-\text{H}$ deformation between 1500 and 1200 cm^{-1} .

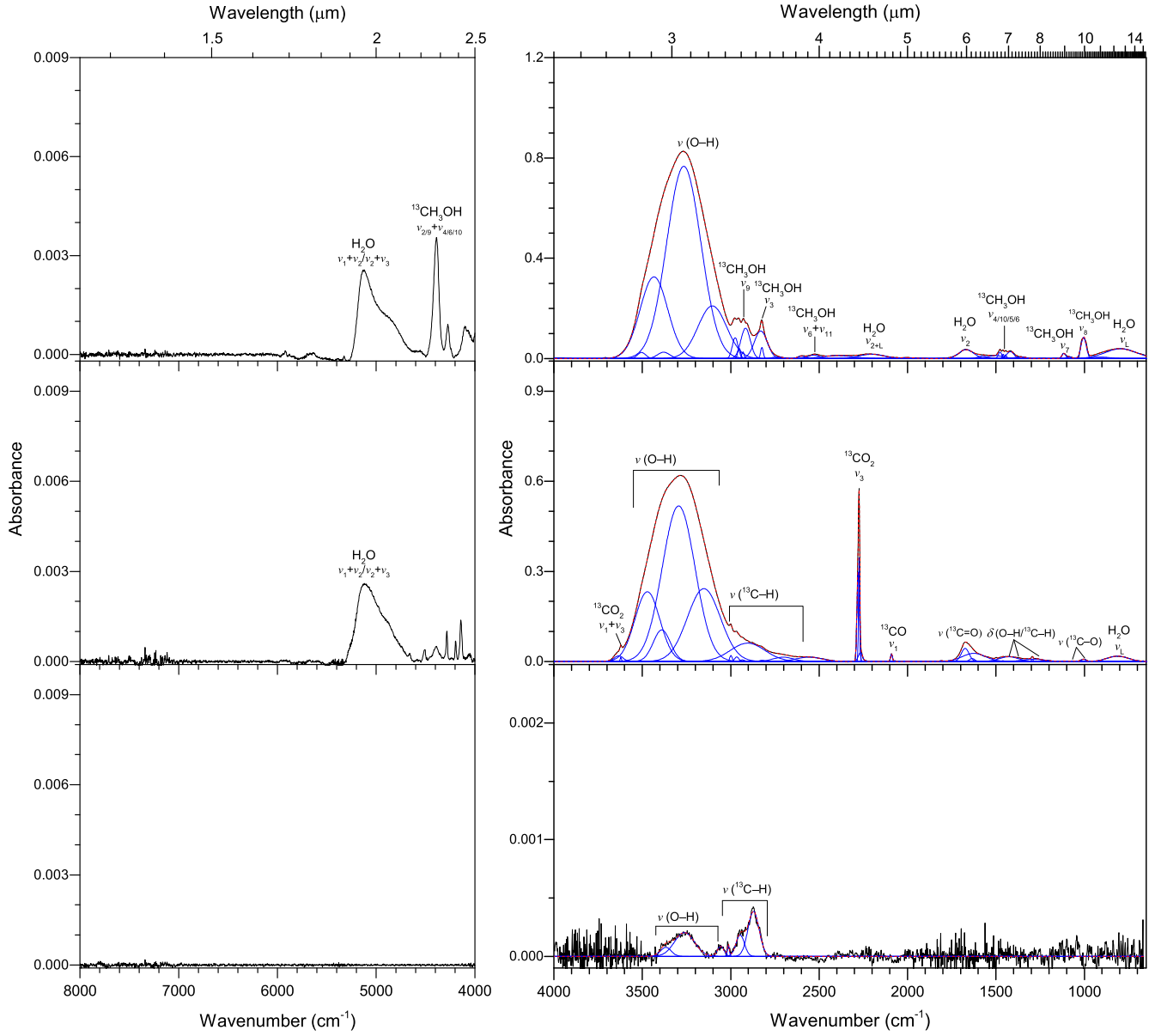


Figure 15. Infrared spectra of water–methanol (H_2O – $^{13}\text{CH}_3\text{OH}$) ice mixtures before (top) and after (middle) irradiation at 10 K. The infrared spectra of the irradiated sample warmed up to 320 K are shown at the bottom. The experimental spectra are plotted in black, the deconvoluted peaks are in blue, and the sums are in red. Only noticeable peaks are labeled for clarity, and detailed peak assignments are listed in Table 7. L indicates libration.

Table 7
Infrared Absorption Features of Water–Methanol (H_2O – $^{13}\text{CH}_3\text{OH}$) Ice Mixtures before and after Irradiation at 40 and 10 K

20 K		10 K			Assignment	Reference
Before Irradiation	After Irradiation	Residue at 320 K	Before Irradiation	After Irradiation		
Position (cm^{-1})						
5117	5087	...	5121	5069	...	$\nu_1 + \nu_2/\nu_2 + \nu_3$ (H_2O)
...	4664	4661, 4512	...	?
4519	4518	$\nu_2 + \nu_3$ ($^{13}\text{CH}_4$)
4392	4405	...	4389	4398	...	$\nu_{2/9} + \nu_{4/6/10}$ ($^{13}\text{CH}_3\text{OH}$)
...	4284	4284	...	$\nu_3 + \nu_4$ ($^{13}\text{CH}_4$)
4276	4274	$\nu_{2/9} + \nu_4$ ($^{13}\text{CH}_3\text{OH}$)
...	4196	4196	...	$\nu_1 + \nu_4$ ($^{13}\text{CH}_4$)
...	4142	4142	...	$\nu_1/\nu_3 + \nu_L$ (H_2O)
...	3621	3621	...	$\nu_1 + \nu_3$ ($^{13}\text{CO}_2$)

Table 7
(Continued)

20 K			10 K			Assignment	Reference
Before Irradiation	After Irradiation	Residue at 320 K	Before Irradiation	After Irradiation	Residue at 320 K		
Position (cm^{-1})							
...	3624, 3473, 3387, 3294, 3212, 2956, 2860, 2714, 2574	3450, 3290, 3123	...	3629, 3468, 3391, 3294, 3146, 2879, 2701, 2556	3370, 3262, 3059	O–H stretch	(4, 5, 11)
3501, 3420, 3382, 3252, 3108	3500, 3430, 3378, 3262, 3104	v (O–H) of water and methanol	(1, 2, 3, 4, 5)
...	2999, 2963, 2927, 2873, 2824	2939, 2870	...	2997, 2962, 2933, 2874, 2820	2949, 2871	^{13}C –H stretch	(4, 5, 11)
2956	2956	v_2 ($^{13}\text{CH}_3\text{OH}$)	(4, 5)
2928	2928	v_9 ($^{13}\text{CH}_3\text{OH}$)	(4, 5)
2908	2910	$2v_4$ ($^{13}\text{CH}_3\text{OH}$)	(4, 5)
2825	2824	v_3 ($^{13}\text{CH}_3\text{OH}$)	(4, 5)
2597	2597	$v_4 + v_{7/11} + v_{4/6/10}$ ($^{13}\text{CH}_3\text{OH}$)	(4, 5)
2526	2526	$v_6 + v_{11}$ ($^{13}\text{CH}_3\text{OH}$)	(4, 5)
2464	2464	$v_6 + v_8$ ($^{13}\text{CH}_3\text{OH}$)	(4, 5)
...	2342	...	2343	v_3 (CO_2)	(5, 6, 7)
...	2275	...	2275	v_3 ($^{13}\text{CO}_2$)	(5, 6, 7)
2226	2228	$2v_{7/11}$ ($^{13}\text{CH}_3\text{OH}$)	(4, 5)
...	2091	2090	...	v_1 (^{13}CO)	(4, 5, 7, 8)
2012	2013	$2v_8$ ($^{13}\text{CH}_3\text{OH}$)	(4, 5)
...	1675, 1656, 1637, 1543	1680	...	1676, 1634, 1619	...	^{13}C =O stretch	(4, 5, 11)
1672	1672	v_2 (H_2O)	(1, 2, 3)
...	1499	1499	...	v_3 (H_2^{13}CO)	(4, 5, 10)
1478	1477	v_4 ($^{13}\text{CH}_3\text{OH}$)	(4, 5)
1461	1460	v_{10} ($^{13}\text{CH}_3\text{OH}$)	(4, 5)
1420	1419	v_5 ($^{13}\text{CH}_3\text{OH}$)	(4, 5)
...	1458, 1418, 1377, 1279	1448, 1337	...	1458, 1421, 1377, 1279	...	$\text{O}-\text{H}/^{13}\text{C}-\text{H}$ deformation	(4, 5, 11)
1340	1338	v_6 ($^{13}\text{CH}_3\text{OH}$)	(4, 5)
...	1295	1295	...	v_4 ($^{13}\text{CH}_4$)	(4, 5, 9)
1118	1116	v_7 ($^{13}\text{CH}_3\text{OH}$)	(4, 5)
...	1117, 1069, 1005	1111, 1062, 1004	...	^{13}C –O stretch	(4, 5, 11)
1008	1007	v_8 ($^{13}\text{CH}_3\text{OH}$)	(4, 5)
833	833	v_{12} ($^{13}\text{CH}_3\text{OH}$)	(4, 5)
...	830	816	...	^{13}C –H out-of-plane deformation	(4, 5, 11)
809	803	v_L (H_2O) libration	(1, 2, 3)

Note. The bands in the residue that remained after the irradiated ice warmed up to 320 K are also listed. ? in column (7) means these peaks are difficult to assign.

References. (1) W. Zheng et al. (2009b); (2) W. Zheng et al. (2006a); (3) C. M. Tonauer et al. (2021); (4) C. J. Bennett et al. (2007); (5) C. Zhu et al. (2020); (6) P. A. Gerakines & R. L. Hudson (2015); (7) H. Carrascosa et al. (2019); (8) C. J. Bennett et al. (2009); (9) C. J. Bennett et al. (2006); (10) M. M. Wohar & P. W. Jagodzinski (1991); (11) G. Socrates (2004).

Table 8
Infrared Absorption Features of Methane–Ammonia ($^{13}\text{CH}_4-\text{NH}_3$) Ice Mixtures before and after Irradiation at 20 and 10 K

20 K			10 K			Assignment	Reference
Before Irradiation	After Irradiation	Residue at 320 K	Before Irradiation	After Irradiation	Residue at 320 K		
Position (cm^{-1})							
6529	6534	$2v_1$ (NH_3)	(3, 4)
5963	5964	$2v_3$ ($^{13}\text{CH}_4$)	(1, 2)
5778	5779	$v_1 + v_3$ ($^{13}\text{CH}_4$)	(1, 2)
5536	5537	$v_3 + 2v_4$ ($^{13}\text{CH}_4$)	(1, 2)
5000	5001	...	5001	5001	...	$v_3 + v_4$ (NH_3)	(3, 4)
4515	4515	$v_2 + v_3$ ($^{13}\text{CH}_4$)	(1, 2)

Table 8
(Continued)

20 K			10 K			Assignment	Reference
Before Irradiation	After Irradiation	Residue at 320 K	Before Irradiation	After Irradiation	Residue at 320 K		
Position (cm^{-1})							
4473	4471	...	4473	4486	...	$v_2 + v_3 (\text{NH}_3)$	(3, 4)
4279	4281	...	4280	4282	...	$v_3 + v_4 (^{13}\text{CH}_4)$	(1, 2)
4191	4191	$v_1 + v_4 (^{13}\text{CH}_4)$	(1, 2)
...	4132	4125	...	$^{13}\text{C}\equiv\text{N}$ overtone	(5, 6)
3825	3825	$3v_4 (^{13}\text{CH}_4)$	(1, 2)
...	3330, 3180	3415, 3331, 3176	...	3435, 3301, 3183	3324, 3200	N–H stretch	(4, 7)
3368	3363	...	3368	3363	...	$v_3 (\text{NH}_3)$	(3, 4)
3208	3208	$v_1 (\text{NH}_3)$	(3, 4)
2996	2997	...	2997	2997	...	$v_3 (^{13}\text{CH}_4)$	(1, 2)
...	2990, 2957, 2932,	2937, 2907, 2896,	...	2962, 2932,	2970, 2954, 2919,	^{13}C –H stretch	(1, 7)
	2888, 2820	2863, 2760		2877, 2728	2863, 2665		
2899	2899	$v_1 (^{13}\text{CH}_4)$	(1, 2)
2806	2806	$v_2 + v_4 (^{13}\text{CH}_4)$	(1, 2)
2577	2577	$2v_4 (^{13}\text{CH}_4)$	(1, 2)
2426	2453	2559, 2420, 2326	2425	2446	2439, 2320	$v (\text{N}-\text{H}^+)$	(4)
...	2158	2127	...	2157	2126	$^{13}\text{C}\equiv\text{N}$ stretch	(5, 6, 7)
...	2100	2091	...	2100	2089	$v (^{13}\text{CN}^-)$	(5, 6, 7)
...	2039	2040	...	2039	2041	$^{13}\text{C}=\text{N}=\text{N}$ stretch	(5, 6, 7)
...	1689	1687	...	$^{13}\text{C}=\text{N}$ stretch	(5, 6, 7)
1628	1627	...	1625	1627	...	$v_4 (\text{NH}_3)$	(3, 4)
...	1593, 1547, 1451	1597, 1546,	...	1593, 1483, 1441	1586, 1483	N–H deformation	(5, 6, 7)
...	1348	1443, 1337	...	1341	1320	^{13}C –H deformation	(5, 6, 7)
1292	1295	...	1290	1295	...	$v_4 (^{13}\text{CH}_4)$	(1, 2)
...	1272, 1060	977	...	1082	1059, 1027	^{13}C –N stretch	(5, 6, 7)
1076	1076	$v_2 (\text{NH}_3)$	(3, 4)
...	813	819	...	^{13}C –H out-of-plane bending	(5, 6, 7)

Note. The bands in the residue that remained after the irradiated ice warmed up to 320 K are also listed.

References. (1) M. J. Apflepal et al. (2018); (2) C. J. Bennett et al. (2006); (3) J. S. Holt et al. (2004); (4) W. Zheng et al. (2008); (5) F. A. Vasconcelos et al. (2020); (6) M. H. Moore & R. L. Hudson (2003); (7) G. Socrates (2004).

Table 9
Infrared Absorption Features of Methane–Carbon Monoxide ($^{13}\text{CH}_4$ – ^{13}CO) Ice Mixtures before and after Irradiation at 20 and 10 K

20 K			10 K			Assignment	Reference
Before Irradiation	After Irradiation	Residue at 320 K	Before Irradiation	After Irradiation	Residue at 320 K		
Position (cm^{-1})							
5971	5971	$2v_3 (^{13}\text{CH}_4)$	(1, 2)
5784	5784	$v_1 + v_3 (^{13}\text{CH}_4)$	(1, 2)
5543	5543	$v_3 + 2v_4 (^{13}\text{CH}_4)$	(1, 2)
...	4851	5131	...	$v_1 + v_2/v_2 + v_3 (\text{H}_2\text{O})$	(9, 10)
...	4650, 4508	4653, 4508	...	?	...
4521	4521	$v_2 + v_3 (^{13}\text{CH}_4)$	(1, 2)
...	4398, 4337	...	$^{13}\text{CH}_3\text{OH}$ combination	(3)
4284	4281	...	4284	4281	...	$v_3 + v_4 (^{13}\text{CH}_4)$	(1, 2)
4194	4192	...	4195	4192	...	$v_1 + v_4 (^{13}\text{CH}_4)$	(1, 2)
4155	4155	$2v_1 (^{13}\text{CO})$	(4)
...	4146, 4137	4148, 4139	...	?	...
3827	3827	$3v_4 (^{13}\text{CH}_4)$	(1, 2)
...	3619	$v_1 + v_3 (^{13}\text{CO}_2)$...
...	3652, 3526, 3401,	3547, 3478,	...	3642, 3521,	3521, 3401,	O–H stretch	(8)
	3281, 3214, 3201,	3380, 3215		3401, 3262	3265, 3116		
...	3072	3065	...	3079	3065	Aromatic ^{13}C –H stretch	(7, 8)
3000	2996	...	3000	2997	...	$v_3 (^{13}\text{CH}_4)$	(1, 2)

Table 9
(Continued)

Before Irradiation	After Irradiation	20 K		10 K		Assignment	Reference
		Residue at 320 K	Position (cm^{-1})	Before Irradiation	After Irradiation		
...	2960, 2930, 2920, 2870, 2830, 2748, 2604	2956, 2922, 2913, 2866, 2853, 2714	...	2960, 2927, 2886, 2870, 2720, 2592	2956, 2940, 2922, 2864, 2876	$^{13}\text{C}-\text{H}$ stretch	(8)
2905	2905	v_1 ($^{13}\text{CH}_4$)	(1, 2)
2808	2809	$v_2 + v_4$ ($^{13}\text{CH}_4$)	(1, 2)
2579	2580	$2v_4$ ($^{13}\text{CH}_4$)	(1, 2)
...	2340	2341	...	v_3 (CO_2)	(5, 6)
...	2274	2274	...	v_3 ($^{13}\text{CO}_2$)	(5, 6)
2137	2137	v_1 (CO)	(4, 6)
2089	2089	v_1 (^{13}CO)	(4, 6)
2038	2038	v_1 ($^{13}\text{C}^{18}\text{O}$)	(4, 6)
...	...	2041	Conjugated $^{13}\text{C} \equiv ^{13}\text{C}$ stretch	(7, 8)
...	1679, 1665, 1584	1677, 1667, 1554	...	1679, 1659, 1569, 1479	1669, 1614	$^{13}\text{C}=\text{O}$ stretch	(8)
...	1458, 1438, 1366	1447, 1367	...	1455, 1435, 1367	1451, 1361	O–H/ $^{13}\text{C}-\text{H}$ deformation	(8)
1292	1294	...	1292	1295	...	v_4 ($^{13}\text{CH}_4$)	(1, 2)
...	1008	1143	...	1002	1152	$^{13}\text{C}-\text{O}$ stretch	(8)
...	827	902	...	$^{13}\text{C}-\text{H}$ out-of-plane bending	(8)

Note. The bands in the residue that remained after the irradiated ice warmed up to 320 K are also listed. ? in column (7) means these peaks are difficult to assign.

References. (1) M. J. Abplanalp et al. (2018); (2) C. J. Bennett et al. (2006); (3) C. Zhang et al. (2024); (4) C. J. Bennett et al. (2009); (5) P. A. Gerakines & R. L. Hudson (2015); (6) H. Carrascosa et al. (2019); (7) M. J. Abplanalp et al. (2019a); (8) G. Socrates (2004); (9) W. Zheng et al. (2009b); (10) C. M. Tonauer et al. (2021).

Table 10
Infrared Absorption Features of Methane–Carbon Dioxide ($^{13}\text{CH}_4-\text{CO}_2$) Ice Mixtures before and after Irradiation at 20 and 10 K

Before Irradiation	After Irradiation	20 K		10 K		Assignment	Reference
		Residue at 320 K	Position (cm^{-1})	Before Irradiation	After Irradiation		
5972	5970	$2v_3$ ($^{13}\text{CH}_4$)	(3, 4)
5784	5783	$v_1 + v_3$ ($^{13}\text{CH}_4$)	(3, 4)
5542	5542	$v_3 + 2v_4$ ($^{13}\text{CH}_4$)	(3, 4)
...	5158	$v_1 + v_2/v_2 + v_3$ (H_2O)	(1, 2)
4979	4977	...	4979	4977	...	$2v_1 + v_3$ ($^{13}\text{CO}_2$)	(7, 8, 9)
4872	4872	...	4872	4868	...	$v_1 + 2v_2 + v_3$ ($^{13}\text{CO}_2$)	(7, 8, 9)
4719	4719	$4v_2 + v_3$ ($^{13}\text{CO}_2$)	(7, 8, 9)
...	4660, 4511	4656, 4512	...	?	...
4523	4523	$v_2 + v_3$ ($^{13}\text{CH}_4$)	(3, 4)
4285	4283	...	4284	4286	...	$v_3 + v_4$ ($^{13}\text{CH}_4$)	(3, 4)
4195	4195	...	4195	4195	...	$v_1 + v_4$ ($^{13}\text{CH}_4$)	(3, 4)
...	4160	4159	...	$2v_1$ (^{13}CO)	(5, 6, 8)
3624	3623	...	3624	3623	...	$v_1 + v_3$ ($^{13}\text{CO}_2$)	(7, 8, 9)
3509	3507	...	3509	3507	...	$2v_2 + v_3$ ($^{13}\text{CO}_2$)	(7, 8, 9)
...	3641, 3510, 3399, 3251, 3075	3517, 3408, 3306, 3100	...	3638, 3527, 3394, 3234, 3080	3508, 3408, 3337, 3107	O–H stretch	(5, 11)
2999	3000	...	2999	3000	...	v_3 ($^{13}\text{CH}_4$)	(3, 4)
...	2968, 2930, 2911, 2830, 2711, 2586	2934, 2872, 2735	...	2964, 2950, 2871, 2836, 2812, 2542	2949, 2882	$^{13}\text{C}-\text{H}$ stretch	(5, 11)
2905	2905	v_1 ($^{13}\text{CH}_4$)	(3, 4)
2811	2810	$v_2 + v_4$ ($^{13}\text{CH}_4$)	(3, 4)
2581	2581	$2v_4$ ($^{13}\text{CH}_4$)	(3, 4)
2348	2348	v_3 (CO_2)	(7, 8, 9)
2297	2297	v_{LO} ($^{13}\text{CO}_2$)	(7, 8, 9)

Table 10
(Continued)

20 K			10 K			Assignment	Reference
Before Irradiation	After Irradiation	Residue at 320 K	Before Irradiation	After Irradiation	Residue at 320 K		
Position (cm^{-1})							
2267	2274	...	2267	2274	...	$v_3 (^{13}\text{CO}_2)$	(7, 8, 9)
...	2091	2091	...	$v_1 (^{13}\text{CO})$	(5, 6, 8)
...	1681, 1665, 1579	1688, 1464	...	1681, 1665, 1629, 1595	1674, 1579	$^{13}\text{C}=\text{O}$ stretch	(5, 11)
...	1499	1499	...	$v_3 (\text{H}_2^{13}\text{CO})$	(5, 10)
...	1262	1370, 1261	...	O-H/ $^{13}\text{C}-\text{H}$ deformation	(5, 11)
1293	1295	1285	1293	1295	...	$v_4 (^{13}\text{CH}_4)$	(3, 4)
...	1003	1005	...	$^{13}\text{C}-\text{O}$ stretch	(5, 11)
651, 637	651, 637	$v_2 (^{13}\text{CO}_2)$	(7, 8, 9)

Note. The bands in the residue that remained after the irradiated ice warmed up to 320 K are also listed. ? in column (7) means these peaks are difficult to assign.

References. (1) W. Zheng et al. (2009b); (2) C. M. Tonauer et al. (2021); (3) M. J. Abplanalp et al. (2018); (4) C. J. Bennett et al. (2006); (5) C. Zhu et al. (2018); (6) C. J. Bennett et al. (2009); (7) P. A. Gerakines & R. L. Hudson (2015); (8) H. Carrascosa et al. (2019); (9) I. R. Cooke et al. (2016); (10) M. M. Wohar & P. W. Jagodzinski (1991); (11) G. Socrates (2004).

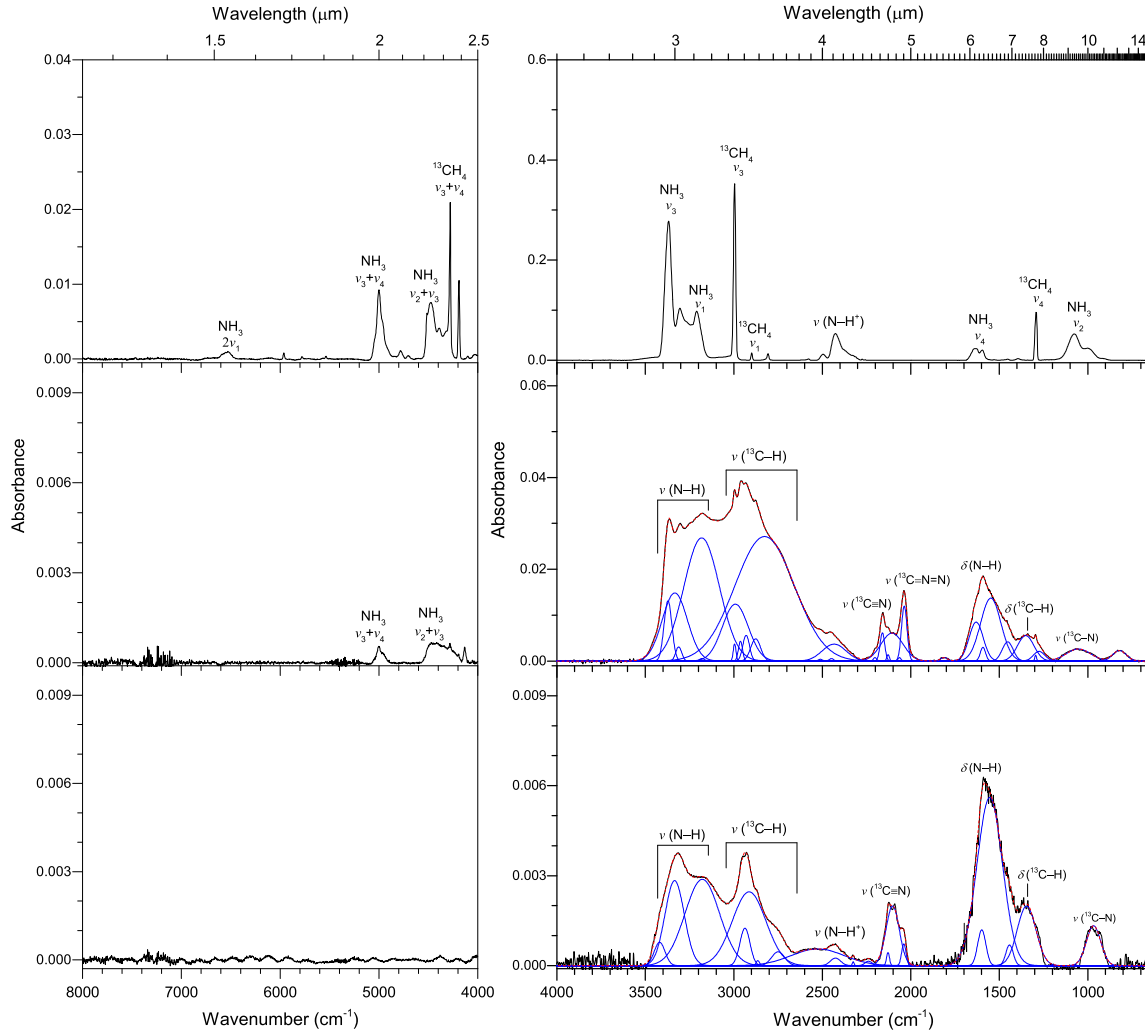


Figure 16. Infrared spectra of methane–ammonia ($^{13}\text{CH}_4-\text{NH}_3$) ice mixtures before (top) and after (middle) irradiation at 20 K. The infrared spectra of the irradiated sample warmed up to 320 K are shown at the bottom. The experimental spectra are plotted in black, the deconvoluted peaks are in blue, and the sums are in red. Only noticeable peaks are labeled for clarity, and detailed peak assignments are listed in Table 8.

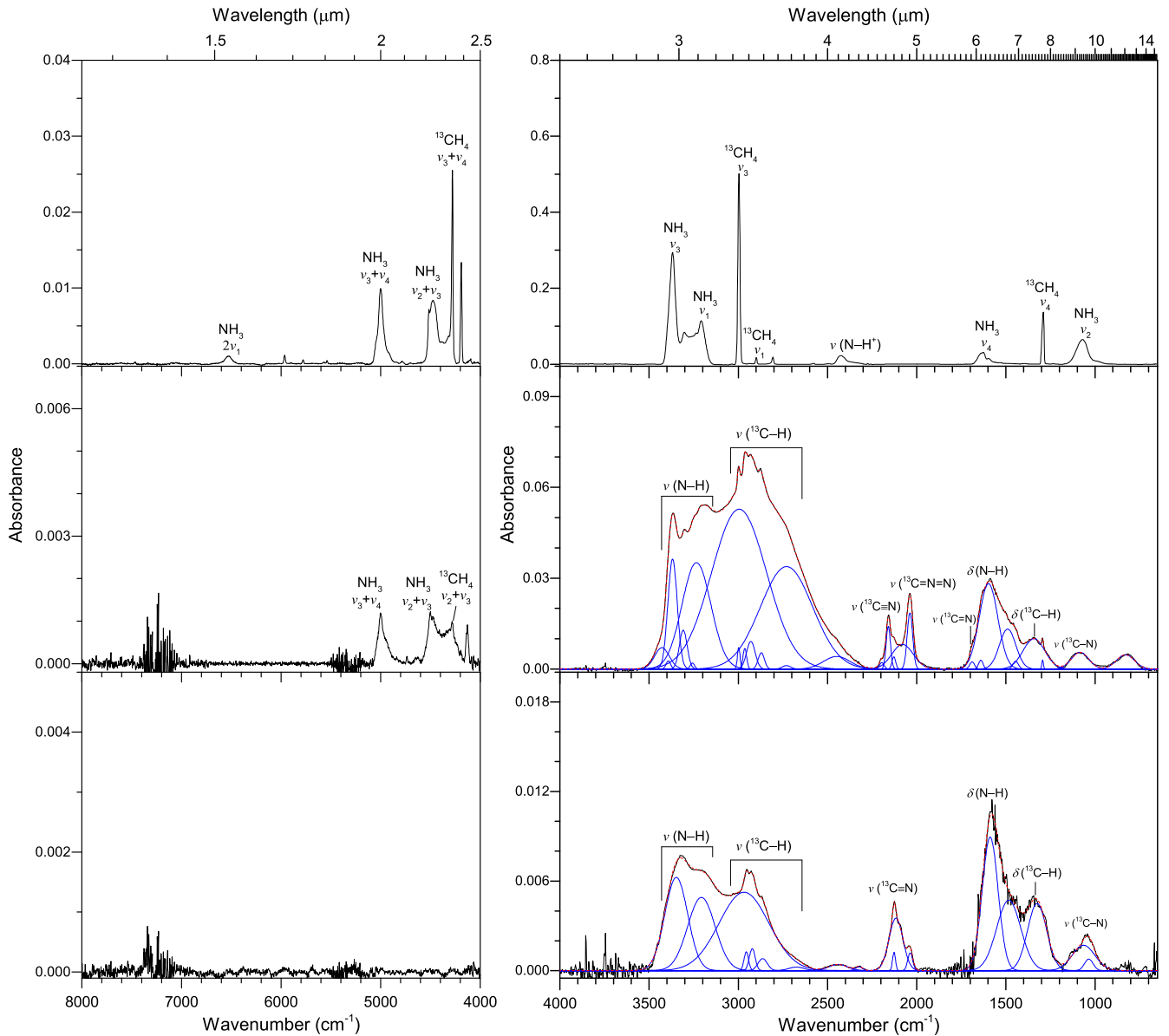


Figure 17. Infrared spectra of methane–ammonia ($^{13}\text{CH}_4\text{--NH}_3$) ice mixtures before (top) and after (middle) irradiation at 10 K. The infrared spectra of the irradiated sample warmed up to 320 K are shown at the bottom. The experimental spectra are plotted in black, the deconvoluted peaks are in blue, and the sums are in red. Only noticeable peaks are labeled for clarity, and detailed peak assignments are listed in Table 8.

These functional groups are potentially from organic molecules, including ethane ($^{13}\text{C}_2\text{H}_6$), ethylene ($^{13}\text{C}_2\text{H}_4$), acetylene ($^{13}\text{C}_2\text{H}_2$), methylacetylene ($^{13}\text{CH}_3^{13}\text{C}\equiv^{13}\text{CH}$), ethyl methyl ether ($^{13}\text{CH}_3\text{O}^{13}\text{CH}_2^{13}\text{CH}_3$), propane ($^{13}\text{C}_3\text{H}_8$), methanol ($^{13}\text{CH}_3\text{OH}$), ethanol ($^{13}\text{CH}_3^{13}\text{CH}_2\text{OH}$), ketene ($\text{H}_2^{13}\text{C}^{13}\text{CO}$), acetaldehyde ($^{13}\text{CH}_3^{13}\text{CHO}$), dimethyl ether ($^{13}\text{CH}_3\text{O}^{13}\text{CH}_3$), and methyl hydroperoxide ($^{13}\text{CH}_3\text{OOH}$) (G. A. Baratta et al. 2003; A. Wada et al. 2006; R. Hudson et al. 2008; A. Bergantini et al. 2017, 2018b; L. Krim & M. Jonusas 2019; C. Mejía et al. 2020; D. V. Mifsdal et al. 2023). These products are volatile under ultrahigh vacuum conditions, and therefore no infrared signal is observed in the 320 K spectra. Except for absorptions of water and ammonia, the $\text{H}_2\text{O--NH}_3$ ice mixtures (ices 7 and 8) display a distinct band at around 2921 cm^{-1} , which is likely from the formation

of a water–ammonia complex ($\text{H}_2\text{O}\cdot\text{NH}_3$) during codeposition (W. Zheng et al. 2009a) (Figures 8 and 9, Table 4). The dangling OH bond in the $\text{H}_2\text{O--NH}_3$ ice mixtures is a broad band centered at 3698 cm^{-1} . After irradiation, the infrared spectra reveal a new band at 1700 cm^{-1} consistent with N–H deformation and is from hydroxylamine (NH_2OH) produced via electron processing (M. H. Moore et al. 2007; W. Zheng et al. 2009a; M. J. Loeffler et al. 2010; W. Zheng & R. I. Kaiser 2010; V. Bordalo et al. 2013).

The spectra of pristine $\text{H}_2\text{O--}^{13}\text{CO}$ ice mixtures (ices 9 and 10) show dominant peaks from ^{13}CO at 2090 cm^{-1} and its overtone ($2\nu_1$) near 4158 cm^{-1} , and absorptions from water ices (Figures 10 and 11, Table 5). The dangling OH bonds in these spectra are broad centered at 3655 and 3621 cm^{-1} at 20 and 10 K, respectively. This band has a higher absorbance at

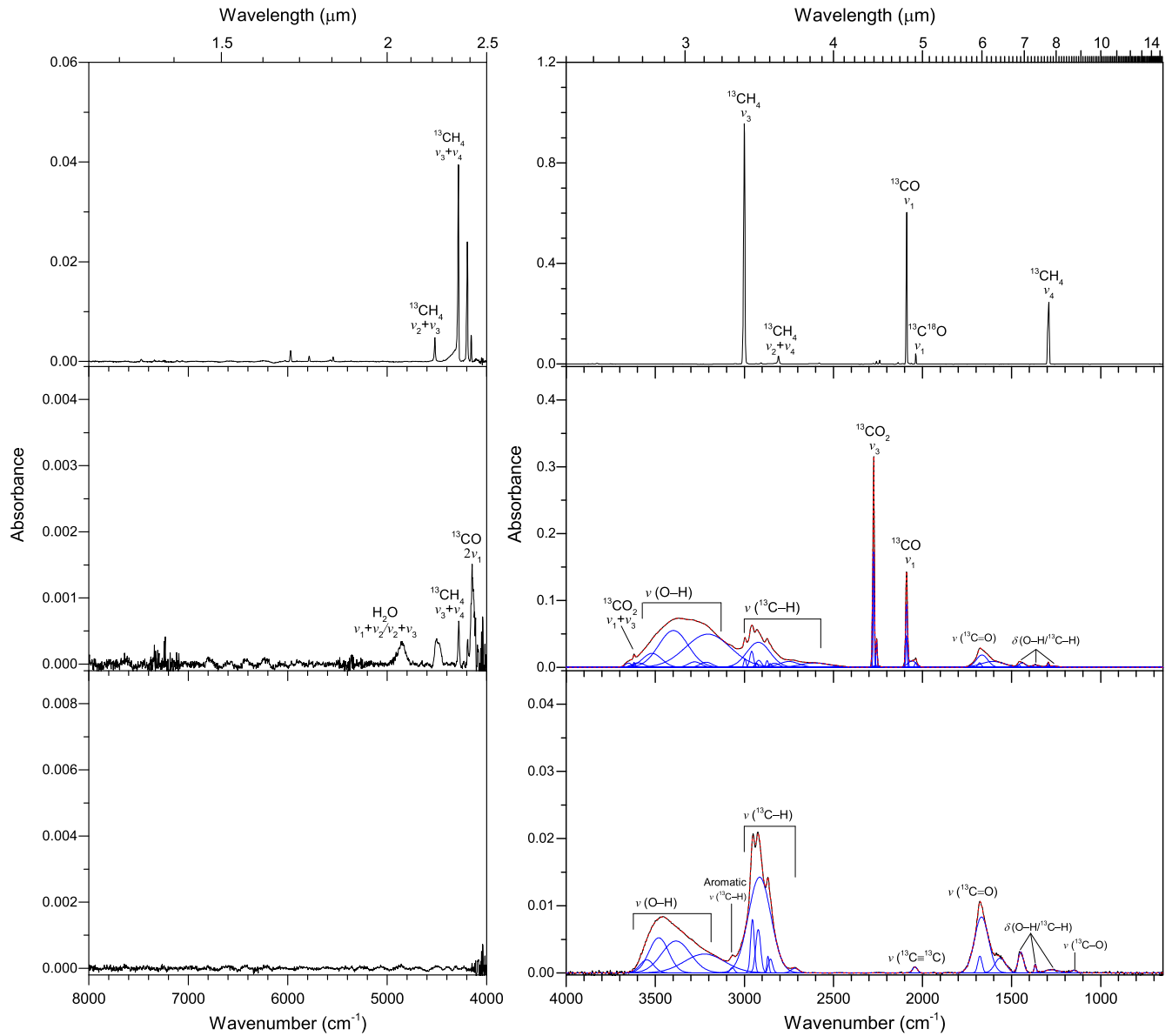


Figure 18. Infrared spectra of methane–carbon monoxide ($^{13}\text{CH}_4$ – ^{13}CO) ice mixtures before (top) and after (middle) irradiation at 20 K. The infrared spectra of the irradiated sample warmed up to 320 K are shown at the bottom. The experimental spectra are plotted in black, the deconvoluted peaks are in blue, and the sums are in red. Only noticeable peaks are labeled for clarity, and detailed peak assignments are listed in Table 9.

20 K than at 10 K due to a larger concentration of carbon monoxide. This finding indicates that carbon monoxide could enhance the absorption of dangling OH, and potential implications on the morphological study of water on the interstellar grain surface considering these two molecules are found to be widespread in interstellar ices (J. Bouwman et al. 2007; A. C. A. Boogert et al. 2015; J. He et al. 2018, 2019; T. Hasegawa et al. 2024; J. A. Noble et al. 2024). After irradiation, the distinct new absorptions are $^{13}\text{CO}_2$ at 2275 and 3621 cm^{-1} , H_2^{13}CO at 1499 cm^{-1} , and $^{13}\text{CH}_4$ at 1295 cm^{-1} . Similar to the processed H_2O – $^{13}\text{CH}_4$ ice mixtures, the infrared spectra display the hydroxyl group (O–H) between 3700 and 3000 cm^{-1} , the hydrocarbyl group ($^{13}\text{C}-\text{H}$) between 3000 and 2500 cm^{-1} , the carbonyl group ($^{13}\text{C}=\text{O}$) at about 1680 cm^{-1} , an overlap band of O–H bending and $^{13}\text{C}-\text{H}$ deformation between 1500 and 1200 cm^{-1} , and a $^{13}\text{C}-\text{O}$ stretch

at about 1010 cm^{-1} (G. Socrates 2004). These groups can be prominent for methanol ($^{13}\text{CH}_3\text{OH}$), ketene ($\text{H}_2^{13}\text{C}^{13}\text{CO}$), ethynol ($^{13}\text{C}_2\text{H}_2\text{O}$), glyoxal ($\text{H}^{13}\text{CO}^{13}\text{CHO}$), glyceraldehyde ($^{13}\text{C}_3\text{H}_6\text{O}_3$), glyoxylic acid ($^{13}\text{C}_2\text{H}_2\text{O}_3$), formic acid (H^{13}COOH), and carbonic acid ($\text{H}_2^{13}\text{CO}_3$) (Z. Awad et al. 2005; C. J. Bennett et al. 2011; A. Jiménez-Escobar et al. 2016; A. K. Eckhardt et al. 2019; F. Schmidt et al. 2019; M. Tsuge et al. 2020; A. M. Turner et al. 2020; A. M. Turner et al. 2021a; C. H. Huang et al. 2022; J. Wang et al. 2024b). Some weak bands corresponding to the O–H, $^{13}\text{C}-\text{H}$, and $^{13}\text{C}=\text{O}$ groups are observed in the 320 K spectra from the ice mixtures processed at 20 K (ice 9). However, the 320 K spectrum from the ices irradiated at 10 K (ice 10) has no signal. This difference is likely because the higher concentration of carbon monoxide can produce unsaturated carbon chain molecules during irradiation, followed by interactions with hydrogen and oxygen atoms within the ice to form complex organic refractory species

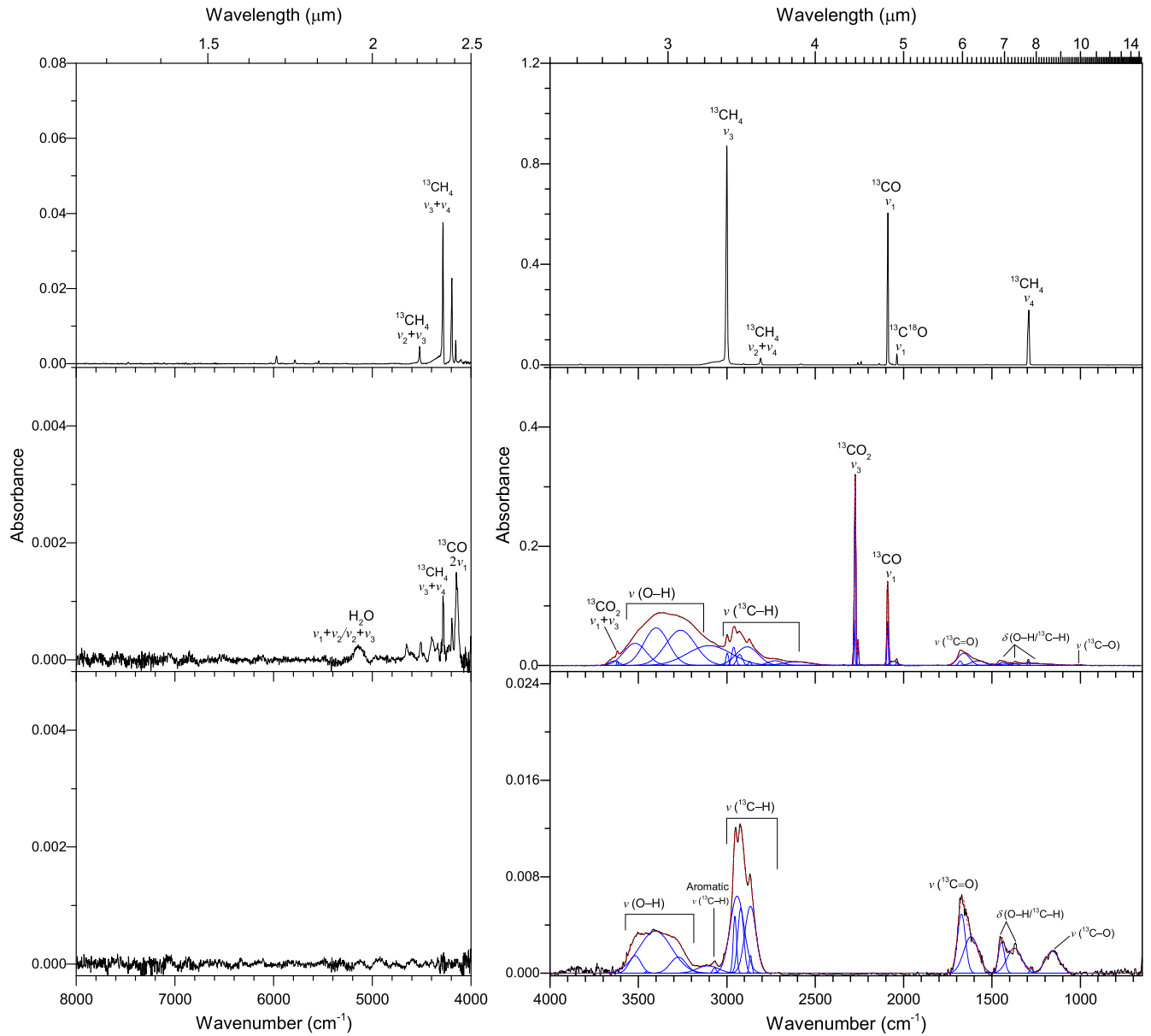


Figure 19. Infrared spectra of methane–carbon monoxide ($^{13}\text{CH}_4$ – ^{13}CO) ice mixtures before (top) and after (middle) irradiation at 10 K. The infrared spectra of the irradiated sample warmed up to 320 K are shown at the bottom. The experimental spectra are plotted in black, the deconvoluted peaks are in blue, and the sums are in red. Only noticeable peaks are labeled for clarity, and detailed peak assignments are listed in Table 9.

(C. J. Bennett et al. 2009). The codeposition of water and carbon dioxide molecules at 40 and 10 K (ices 11 and 12) results in prominent absorptions of these two compounds in the spectra (Figures 12 and 13, Table 6), including a broad peak at 3649 cm^{-1} of the dangling OH bond (K. I. Öberg et al. 2007; W. Zheng & R. I. Kaiser 2007b). The spectra from irradiated H_2O – $^{13}\text{CO}_2$ ices exhibit the absorption of ^{13}CO at 2092 cm^{-1} and functional groups of O–H, ^{13}C –H, ^{13}C =O, and broad overlap bands for O–H and ^{13}C –H (G. Socrates 2004). These groups originate from molecules like carbonic acid ($\text{H}_2^{13}\text{CO}_3$), the hydrocarboxyl radical (HO^{13}CO), H_2^{13}CO , and H^{13}COOH (P. A. Gerakines et al. 2000; C. Y. R. Wu et al. 2003; C. R. Ponciano et al. 2005; W. Zheng & R. I. Kaiser 2007b; Z. Peeters et al. 2010; S. Pilling et al. 2010b; X. Wang & T. Burgi 2021). No signal is observed at the 320 K spectra of water–carbon dioxide ice mixtures. The dangling

OH features are also observed in the irradiated H_2O – ^{13}CO and H_2O – $^{13}\text{CO}_2$ ice mixtures, likely from the residual unirradiated ices due to the energy electron penetration depth being less than the thickness of the pristine ices (see Section 2).

For H_2O – $^{13}\text{CH}_3\text{OH}$ ice mixtures (ices 13 and 14), the spectra before irradiation have noticeable absorptions of these two molecules, including broad bands for the hydroxyl group and the hydrocarbyl group between 3700 and 2600 cm^{-1} (Figures 14 and 15, Table 7). The absence of the dangling OH signal in these spectra is likely a consequence of the high methanol concentration, considering these features can be detected in a more dilute H_2O – CH_3OH ice mixture with a ratio of 10:1 (R. L. Hudson et al. 2024). In addition, the radiation-driven compaction of microporous ice can also decrease the dangling OH absorptions

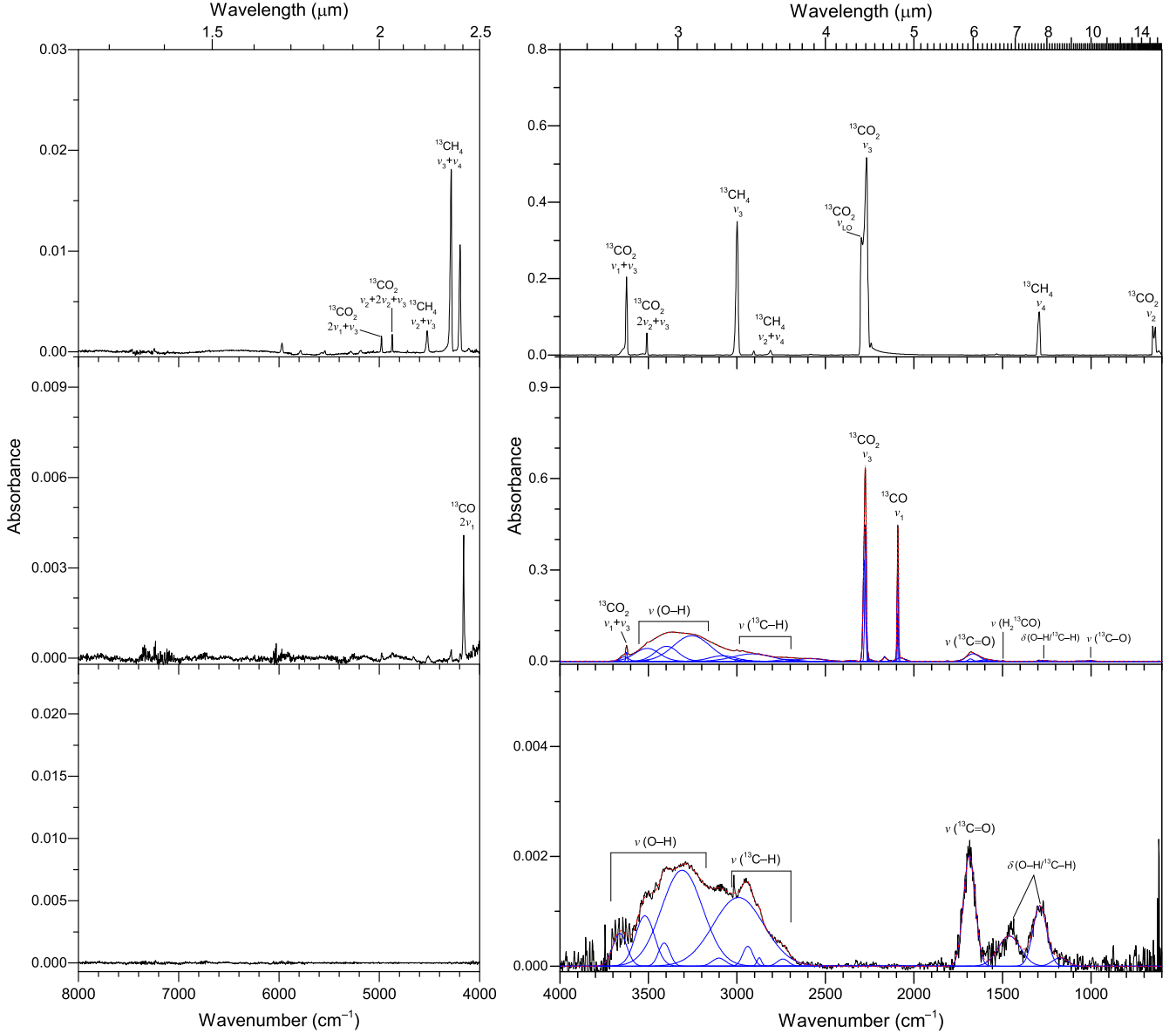


Figure 20. Infrared spectra of methane–carbon dioxide ($^{13}\text{CH}_4$ – $^{13}\text{CO}_2$) ice mixtures before (top) and after (middle) irradiation at 20 K. The 320 K spectra are shown at the bottom. The experimental spectra are plotted in black, the deconvoluted peaks are in blue, and the sums are in red. Only noticeable peaks are labeled for clarity, and detailed peak assignments are listed in Table 10. LO indicates longitudinal mode.

(U. Raut et al. 2008; P. R. Behr et al. 2020). After irradiation, more complex absorptions are observed, resulting from a large number of products including $^{13}\text{CO}_2$, ^{13}CO , $^{13}\text{CH}_4$, and H_2^{13}CO together with functional groups related to O–H, ^{13}C –H, ^{13}C =O, and ^{13}C –O bonds. These functional groups can be combined into complex organic molecules such as polyols and hydroxycarboxylic acids, sugar-related compounds, and so forth (M. H. Moore et al. 1996; C. J. Bennett et al. 2007; A. L. F. de Barros et al. 2014; S. Maity et al. 2015; N. Abou Mrad et al. 2016; N. Sakakibara et al. 2020; C. Zhu et al. 2020; N. E. Soland et al. 2023). Since some products are nonvolatile, related functional groups (hydroxyl group, hydrocarbyl group, and carbonyl group) are also observed in the 320 K spectra. The absorptions of residues at 320 K from processed ice at 40 K show a higher intensity than that from ice irradiated at

10 K, suggesting a temperature-dependence mechanism in the formation of these molecules.

Except for the H_2O – $^{13}\text{CH}_4$ ice mixtures, which are discussed above, the infrared spectra of additional methane-bearing binary ice mixtures are shown in Figures 16–23, along with peak assignments in Tables 8–11. For $^{13}\text{CH}_4$ –NH₃ (ices 15 and 16) before irradiation, spectra at 20 and 10 K (Figures 16 and 17, Table 8) have similar profiles and display peaks from methane at 5963 cm^{-1} ($2\nu_3$), 5778 cm^{-1} ($\nu_1 + \nu_3$), 5536 cm^{-1} ($\nu_3 + 2\nu_4$), 4515 cm^{-1} ($\nu_2 + \nu_3$), 4279 cm^{-1} ($\nu_3 + \nu_4$), 4191 cm^{-1} ($\nu_1 + \nu_4$), 3825 cm^{-1} ($3\nu_4$), 2996 cm^{-1} (ν_3), 2899 cm^{-1} (ν_1), 2806 cm^{-1} ($\nu_2 + \nu_4$), 2577 cm^{-1} ($2\nu_4$), and 1292 cm^{-1} (ν_4) (M. J. Abplanalp et al. 2018; C. Zhang et al. 2023b), together with absorptions of ammonia having shifts in different degrees compared to pure ammonia, as

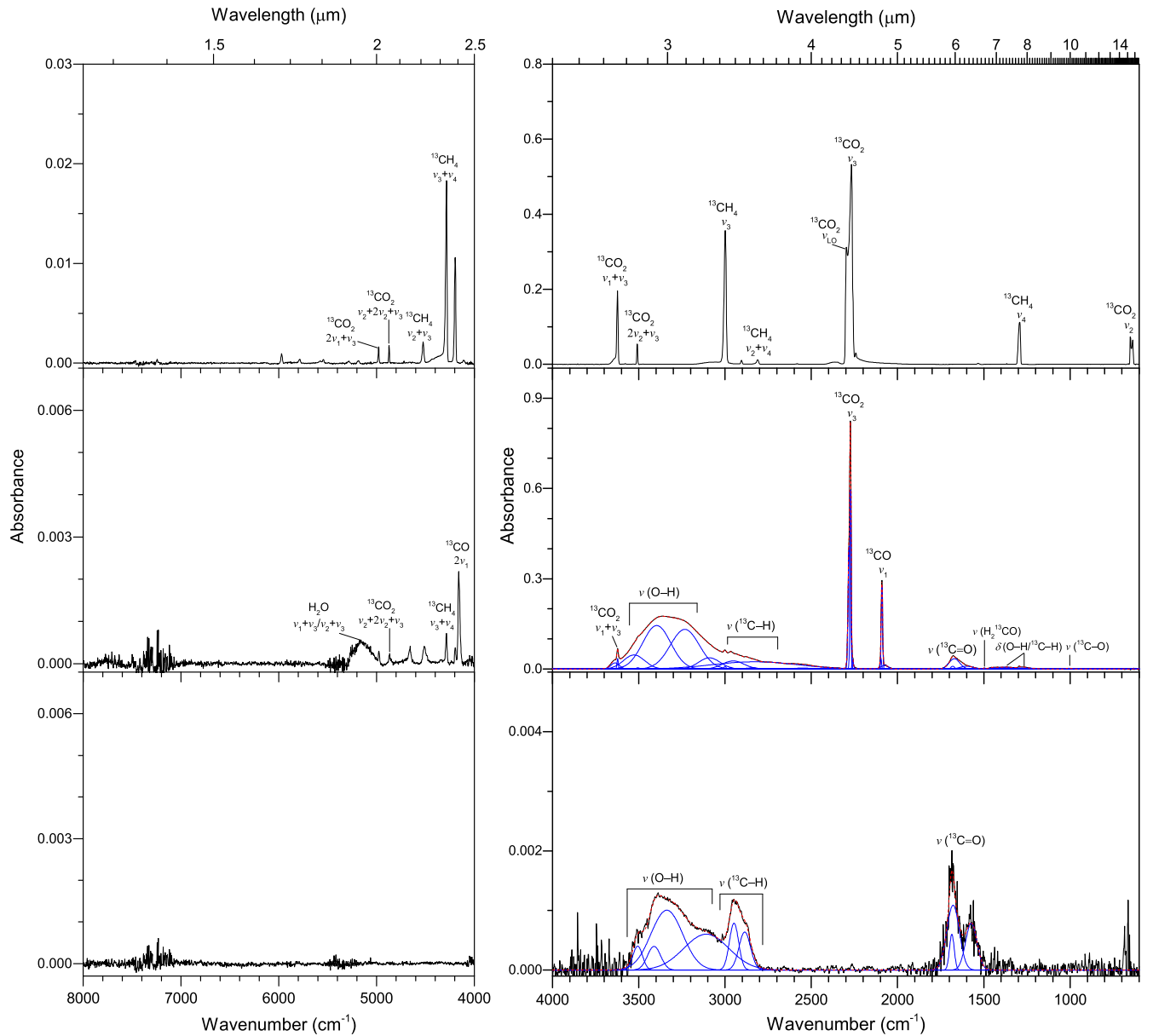


Figure 21. Infrared spectra of methane–carbon dioxide ($^{13}\text{CH}_4$ – $^{13}\text{CO}_2$) ice mixtures before (top) and after (middle) irradiation at 10 K. The 320 K spectra are shown at the bottom. The experimental spectra are plotted in black, the deconvoluted peaks are in blue, and the sums are in red. Only noticeable peaks are labeled for clarity, and detailed peak assignments are listed in Table 10. LO indicates longitudinal mode.

aforementioned. Upon irradiation, the primary bands in the spectra are N–H and ^{13}C –H bonds between 350 and 2500 cm^{-1} along with their deformation vibration modes between 1700 and 1200 cm^{-1} , and weak signals of ^{13}C –N stretch near 1080 cm^{-1} (G. Socrates 2004). The bands at 2158 and 2039 cm^{-1} suggest the formation of nitriles ($^{13}\text{C}\equiv\text{N}$) and diazo ($^{13}\text{C}=\text{N}=\text{N}$) compounds (G. Socrates 2004; F. A. Vasconcelos et al. 2020). The weak broad band between these two peaks centered about 2100 cm^{-1} is from cyanide anion ($^{13}\text{CN}^-$) and azides (N_3^-) (W. Zheng et al. 2008; Y. S. Kim & R. I. Kaiser 2011; F. d. A. Vasconcelos et al. 2017). In addition, a weak shoulder band at about 1689 cm^{-1} from the $^{13}\text{C}=\text{N}$ double bond is also observed (G. Socrates 2004). The formation of these functional groups suggests that complex species such as hydrocarbons, amine, nitriles, imine, and even

nitrogen heteroaromatics are potentially produced through the radiation chemistry within the TNO surface containing methane and ammonia (Y. S. Kim & R. I. Kaiser 2011; M. Förstel et al. 2017; S. Kundu et al. 2017; M. J. Abplanalp et al. 2018, 2019b; F. A. Vasconcelos et al. 2020; A. M. Turner et al. 2021b; A. Canta et al. 2023; C. Zhang et al. 2023a; K. A. Kipfer et al. 2024; J. Wang et al. 2024a). A fraction of these higher molecular weight products remains even warmed up to 320 K, and therefore the absorptions of N–H and ^{13}C –H bonds, the peak at 2158 cm^{-1} of nitriles ($^{13}\text{C}\equiv\text{N}$), and ^{13}C –N stretch bands are observed in their spectra.

The spectra of pristine ice mixtures combining methane with carbon monoxide and carbon dioxide (ices 17–20) only have a few peaks associated with these molecules (Figures 18–21, Tables 9 and 10). After irradiation, these spectra exhibit

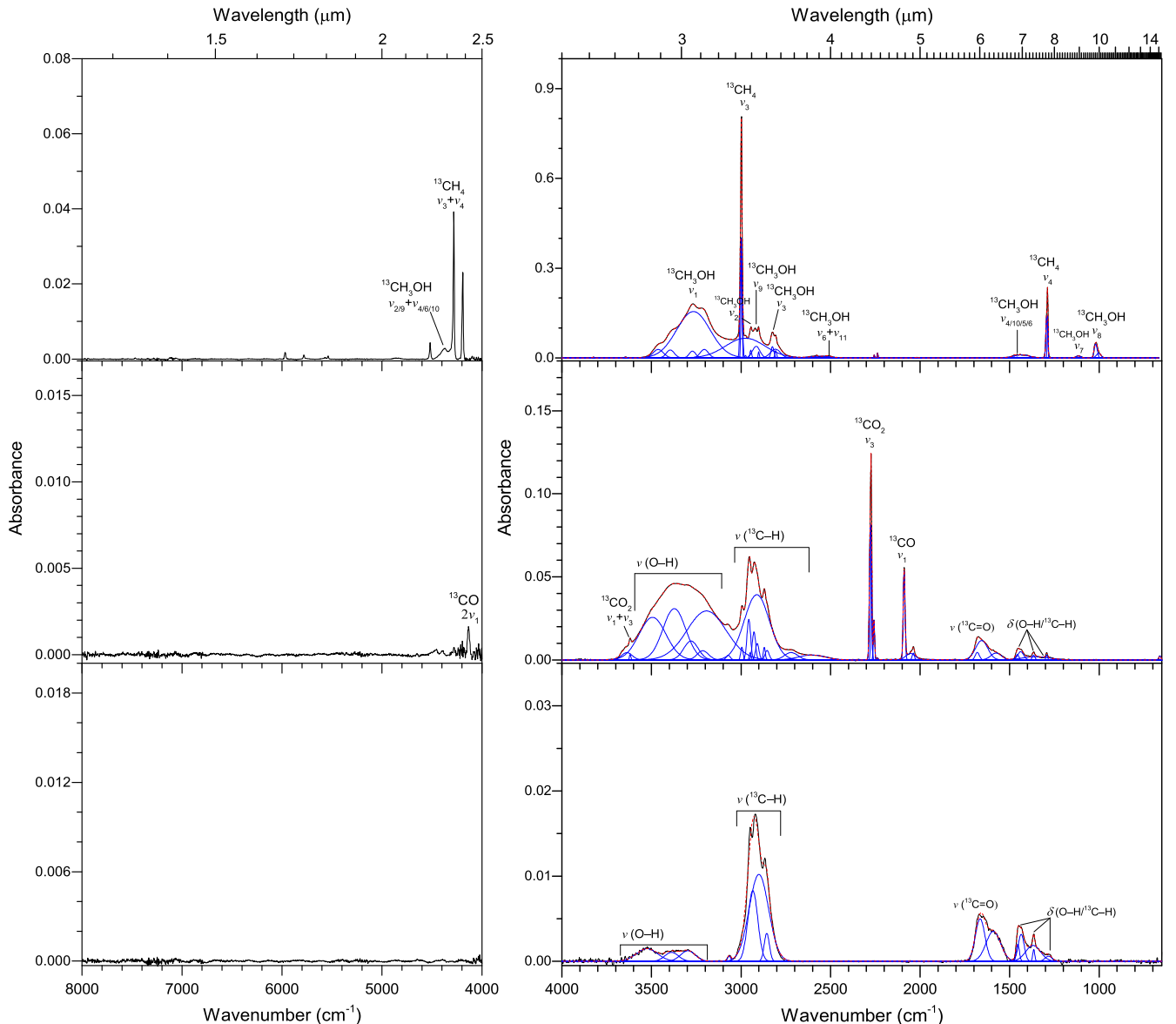


Figure 22. Infrared spectra of methane–methanol ($^{13}\text{CH}_4$ – $^{13}\text{CH}_3\text{OH}$) ice mixtures before (top) and after (middle) irradiation at 20 K. The 320 K spectra are shown at the bottom. The experimental spectra are plotted in black, the deconvoluted peaks are in blue, and the sums are in red. Only noticeable peaks are labeled for clarity, and detailed peak assignments are listed in Table 11.

similar profiles, which is likely because they consist of the same elements: carbon, oxygen, and hydrogen. Except for products of $^{13}\text{CO}_2$ and ^{13}CO , the spectra after irradiation of both systems show a set of products with functional groups of O–H, ^{13}C –H, ^{13}C =O, and ^{13}C –O attached to the long carbon chain bones, referring to compounds of hydrocarbons, alcohols, aldehydes, ketenes, carboxylic acids, acetic acid, esters, and carbohydrates, as in previous reports (C. J. Bennett et al. 2005; C. J. Bennett & R. I. Kaiser 2007a; Y. S. Kim & R. I. Kaiser 2010; R. I. Kaiser et al. 2014; S. Maity et al. 2014a; M. J. Abplanalp et al. 2016b, 2019b; A. Bergantini et al. 2018a, 2018d; C. Zhu et al. 2018; C. Zhu et al. 2021; N. F. Kleimeier & R. I. Kaiser 2022). However, the irradiation dose used here is much higher than that in prior studies, leading to more complex products, which are not desorbed even when heating these products to 320 K. Therefore, the relevant functional groups, including O–H, ^{13}C –H,

^{13}C =O, and ^{13}C –O, are also detected in the spectra at 320 K. It is worth noting that the absorbance ratio of ^{13}C –H to O–H bond-stretching vibrations in the residues from the irradiated $^{13}\text{CH}_4$ – ^{13}CO system (ices 17 and 18) is higher than that in the irradiated $^{13}\text{CH}_4$ – $^{13}\text{CO}_2$ mixtures (ices 19 and 20), and the ^{13}C –H feature of aromatic-related molecules are only detected in the $^{13}\text{CH}_4$ – ^{13}CO system. Here, the irradiated carbon monoxide generated unsaturated, long carbon-chained molecules, which facilitates the formation of hydrocarbon molecules through incorporating hydrogen atoms in the ices (C. S. Jamieson et al. 2006b). In contrast, the products of irradiated carbon dioxide are mainly high-order carbon oxides that form O–H bonds by interreacting with hydrogen atoms (C. J. Bennett et al. 2004, 2014; C. S. Jamieson et al. 2006a, 2007b, 2007a, 2008; R. I. Kaiser & A. M. Mebel 2008; C. Zhang et al. 2025b). Although the $^{13}\text{CH}_4$ – $^{13}\text{CH}_3\text{OH}$ system (ices 21 and 22) have the same elements as ices composed of

Table 11
Infrared Absorption Features of Methane–Methanol ($^{13}\text{CH}_4$ – $^{13}\text{CH}_3\text{OH}$) Ice Mixtures before and after Irradiation at 20 and 10 K

20 K		10 K				Assignment	Reference
Before Irradiation	After Irradiation	Residue at 320 K	Before Irradiation	After Irradiation	Residue at 320 K		
Position (cm^{-1})							
5969	5964	$2v_3$ ($^{13}\text{CH}_4$)	(2, 3)
5781	5779	$v_1 + v_3$ ($^{13}\text{CH}_4$)	(2, 3)
5539	5538	$v_3 + 2v_4$ ($^{13}\text{CH}_4$)	(2, 3)
...	5143	...	$v_1 + v_2/v_2 + v_3$ (H_2O)	(1, 12)
...	4648	4738, 4657	...	?	...
4519	4518	4504	...	$v_2 + v_3$ ($^{13}\text{CH}_4$)	(2, 3)
4372	4380	$v_{2/9} + v_{4/6/10}$ ($^{13}\text{CH}_3\text{OH}$)	(4, 5)
4281	4283	...	4280	4283	...	$v_3 + v_4$ ($^{13}\text{CH}_4$)	(2, 3)
4192	4195	...	4192	4195	...	$v_1 + v_4$ ($^{13}\text{CH}_4$)	(2, 3)
...	4134	4147	...	$2v_1$ (^{13}CO)	(4, 5, 6, 8)
...	3619	3619	...	$v_1 + v_3$ ($^{13}\text{CO}_2$)	(4, 5, 7, 8)
...	3636, 3469, 3370, 3277, 3211, 3191	3521, 3388, 3294	...	3651, 3521, 3395, 3294, 3236, 3196	3550, 3468, 3391, 3192	O–H stretch	(2, 5, 10)
3491, 3468, 3405, 3271, 3089	3405, 3253, 3068,	v_1 ($^{13}\text{CH}_3\text{OH}$)	(4, 5)
...	3070	3065	Aromatic ^{13}C –H stretch	(11)
2998	2998	v_3 ($^{13}\text{CH}_4$)	(2, 3)
...	2994, 2952, 2926, 2870	2946, 2920, 2866	...	2999, 2962, 2928, 2870	2995, 2955, 2924, 2863, 2838	^{13}C –H stretch	(2, 5, 10)
2943	2943	v_2 ($^{13}\text{CH}_3\text{OH}$)	(4, 5)
2918	2920	v_9 ($^{13}\text{CH}_3\text{OH}$)	(4, 5)
2901	2901	v_1 ($^{13}\text{CH}_4$)	(2, 3)
2815	2815	v_3 ($^{13}\text{CH}_3\text{OH}$)	(4, 5)
2610	2597	$v_4 + v_{7/11} + v_{4/6/10}$ ($^{13}\text{CH}_3\text{OH}$)	(4, 5)
2511	2511	$v_6 + v_{11}$ ($^{13}\text{CH}_3\text{OH}$)	(4, 5)
2464	2464	$v_6 + v_8$ ($^{13}\text{CH}_3\text{OH}$)	(4, 5)
...	2343	2340	...	v_3 (CO_2)	(4, 5, 7, 8)
...	2274	2274	...	v_3 ($^{13}\text{CO}_2$)	(4, 5, 7, 8)
2238	2238	$2v_{7/11}$ ($^{13}\text{CH}_3\text{OH}$)	(4, 5)
...	2089	2090	...	v_1 (^{13}CO)	(4, 5, 6, 8)
...	2038	2039	...	v_1 ($^{13}\text{C}^{18}\text{O}$)	(4, 5, 6, 8)
2021	1897	$2v_8$ ($^{13}\text{CH}_3\text{OH}$)	(4, 5)
...	1680, 1653, 1589, 1569	1669, 1593	...	1678, 1665, 1614, 1556	1685, 1677, 1552, 1510	$^{13}\text{C}=\text{O}$ stretch	(2, 5, 10)
...	1499	1499	...	v_3 (H_2^{13}CO)	(4, 5, 9)
1472	1473	v_4 ($^{13}\text{CH}_3\text{OH}$)	(4, 5)
1458	1458	v_{10} ($^{13}\text{CH}_3\text{OH}$)	(4, 5)
1439	1420	v_5 ($^{13}\text{CH}_3\text{OH}$)	(4, 5)
...	1457, 1435, 1365, 1255	1453, 1434, 1365, 1281	...	1459, 1435, 1365, 1259	1450, 1365	O–H/ ^{13}C –H deformation	(2, 5, 10)
1407	1400	v_6 ($^{13}\text{CH}_3\text{OH}$)	(4, 5)
1289	1293	...	1290	1294	...	v_4 ($^{13}\text{CH}_4$)	(2, 3)
1111	1114	v_7 ($^{13}\text{CH}_3\text{OH}$)	(4, 5)
...	1036, 1009	...	^{13}C –O stretch	(2, 5, 10)
1026	1025	v_{11} ($^{13}\text{CH}_3\text{OH}$)	(4, 5)
1008	1001	v_8 ($^{13}\text{CH}_3\text{OH}$)	(4, 5)
833	833	v_{12} ($^{13}\text{CH}_3\text{OH}$)	(4, 5)
...	821	...	^{13}C –H out-of-plane deformation	(2, 5, 10)

Note. The bands in the residue that remained after the irradiated ice warmed up to 320 K are also listed. ? in column (7) means these peaks are difficult to assign.

References. (1) W. Zheng et al. (2009b); (2) M. J. Abplanalp et al. (2018); (3) C. J. Bennett et al. (2006); (4) C. J. Bennett et al. (2007); (5) C. Zhu et al. (2020); (6) C. J. Bennett et al. (2009); (7) P. A. Gerakines & R. L. Hudson (2015); (8) H. Carrascosa et al. (2019); (9) M. M. Wohar & P. W. Jagodzinski (1991); (10) G. Socrates (2004); (11) M. J. Abplanalp et al. (2019a); (12) C. M. Tonauer et al. (2021).

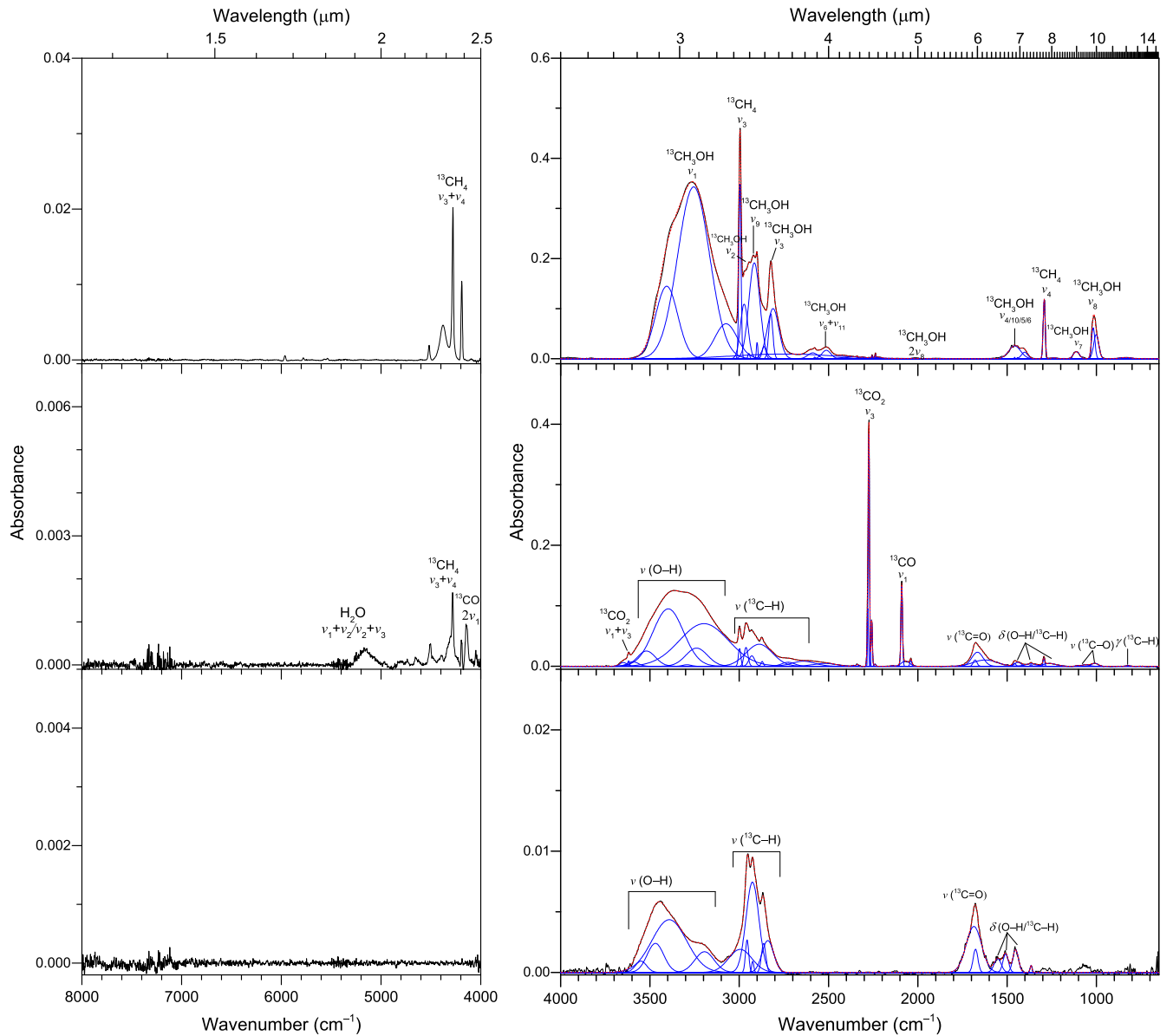


Figure 23. Infrared spectra of methane–methanol ($^{13}\text{CH}_4$ – $^{13}\text{CH}_3\text{OH}$) ice mixtures before (top) and after (middle) irradiation at 10 K. The 320 K spectra are shown at the bottom. The experimental spectra are plotted in black, the deconvoluted peaks are in blue, and the sums are in red. Only noticeable peaks are labeled for clarity, and detailed peak assignments are listed in Table 11.

Table 12
Infrared Absorption Features of Ammonia–Carbon Monoxide ($\text{NH}_3\text{--}^{13}\text{CO}$) Ice Mixtures before and after Irradiation at 20 and 10 K

20 K			10 K			Assignment	Reference
Before Irradiation	After Irradiation	Residue at 320 K	Before Irradiation	After Irradiation	Residue at 320 K		
Position (cm^{-1})							
6545	6545	$2v_1 (\text{NH}_3)$	(1, 2)
...	5095	...	$v_1 + v_3 / v_2 + v_3 (\text{H}_2\text{O})$	(3, 13)
5002	5010	...	5011	5010	...	$v_3 + v_4 (\text{NH}_3)$	(1, 2)
4470	4509	...	4470	4512	...	$v_2 + v_3 (\text{NH}_3)$	(1, 2)
...	4285	4288	...	$v_3 + v_4 (^{13}\text{CH}_4)$	(4)
...	4195	4197	...	$v_1 + v_4 (^{13}\text{CH}_4)$	(4)
4156	4159	4159	...	$2v_1 (^{13}\text{CO})$	(6, 7)
...	3621	3621	...	$v_1 + v_3 (^{13}\text{CO}_2)$	(5, 6)
...	3448, 3321, 3218, 3115	3327, 3196, 3141	...	3573, 3455, 3319, 3228, 3080, 3036	3444, 3347, 3214, 3040	N–H/O–H stretch	(10)

Table 12
(Continued)

20 K			10 K			Assignment	Reference
Before Irradiation	After Irradiation	Residue at 320 K	Before Irradiation	After Irradiation	Residue at 320 K		
Position (cm^{-1})							
3370	3370	...	3371	3372	...	$v_3 (\text{NH}_3)$	(1, 2)
3305,	3307,	$v_1 (\text{NH}_3)$	(1, 2)
3244, 3211			3243, 3210				
...	2930, 2869, 2564	2944, 2871, 2471	...	2996, 2907, 2820, 2728, 2622	2946, 2851	$^{13}\text{C}-\text{H}$ stretch	(10)
...	2343	2343	...	$v_3 (\text{CO}_2)$	(5, 6)
...	2275	2275	...	$v_3 (^{13}\text{CO}_2)$	(5, 6)
...	2178	2179	...	$^{13}\text{C}\equiv\text{N}$ stretch	(8, 9, 10)
...	2108	2101	...	2108	2100	$v (\text{O}^{13}\text{CN}^-)$	(11)
2088	2093	...	2088	2092	...	$v_1 (^{13}\text{CO})$	(6, 7)
2039	2039	$v_1 (^{13}\text{C}^{18}\text{O})$	(6, 7)
...	2042	2042	...	$^{13}\text{C}=\text{N}=\text{N}$ stretch	(8, 9, 10)
1627	1627	$v_4 (\text{NH}_3)$	(1, 2)
...	1656, 1590, 1541	1697, 1652	...	1663, 1596	1689, 1652, 1626, 1549,	$^{13}\text{C}=\text{O}/^{13}\text{C}=\text{N}/\text{N}=\text{O}$ stretch	(10)
...	1498	1497	...	$v_3 (\text{H}^{13}\text{CO})$	(12)
...	1486, 1468, 1381, 1324	1560, 1371, 1296	...	1486, 1381	1510, 1448, 1374, 1311	$\text{O}-\text{H}/\text{N}-\text{H}/^{13}\text{C}-\text{H}$ deformation	(10)
...	1297	1297	...	$v_4 (^{13}\text{CH}_4)$	(4)
1062	1064	$v_2 (\text{NH}_3)$	(1, 2)
...	1122, 1046	1105, 1007	...	$^{13}\text{C}-\text{N}/^{13}\text{C}-\text{O}$ stretch	(10)
...	867, 763	$^{13}\text{C}-\text{H}$ out-of-plane deformation	(10)

Note. The bands in the residue that remained after the irradiated ice warmed up to 320 K are also listed.

References. (1) J. S. Holt et al. (2004); (2) W. Zheng et al. (2008); (3) W. Zheng et al. (2009b); (4) C. J. Bennett et al. (2006); (5) P. A. Gerakines & R. L. Hudson (2015); (6) H. Carrascosa et al. (2019); (7) C. J. Bennett et al. (2009); (8) F. A. Vasconcelos et al. (2020); (9) M. H. Moore & R. L. Hudson (2003); (10) G. Socrates (2004); (11) C. J. Bennett et al. (2010); (12) M. M. Wohar & P. W. Jagodzinski (1991); (13) C. M. Tonauer et al. (2021).

Table 13
Infrared Absorption Features of Ammonia–Carbon Dioxide ($\text{NH}_3-^{13}\text{CO}_2$) Ice Mixtures before and after Irradiation at 40 and 10 K

40 K		10 K		Assignment	Reference
Before Irradiation	After Irradiation	Before Irradiation	After Irradiation		
Position (cm^{-1})					
7244	...	7251	...	$2v_1 + 2v_3 (^{13}\text{CO}_2)$	(4, 5)
6577	...	6578	...	$2v_1 (\text{NH}_3)$	(1, 2)
...	5097	...	5123	$v_1 + v_3/v_2 + v_3 (\text{H}_2\text{O})$	(3, 11)
5023	...	5025	...	$v_3 + v_4 (\text{NH}_3)$	(1, 2)
4977	4984	4979	4980	$2v_1 + v_3 (^{13}\text{CO}_2)$	(4, 5)
4870	4878	4872	4874	$v_1 + 2v_2 + v_3 (^{13}\text{CO}_2)$	(4, 5)
4491	...	4493	...	$v_2 + v_3 (\text{NH}_3)$	(1, 2)
...	4159	...	4164	$2v_1 (^{13}\text{CO})$	(5, 6)
3622	3628	3622	3625	$v_1 + v_3 (^{13}\text{CO}_2)$	(4, 5)
3507	3507	3507	3507	$2v_2 + v_3 (^{13}\text{CO}_2)$	(4, 5)
3412, 3381	...	3414, 3383	...	$v_3 (\text{NH}_3)$	(1, 2)
3312, 3249, 3220	...	3312, 3249, 3221	...	$v_1 (\text{NH}_3)$	(1, 2)
...	3639, 3442, 3370, 3245, 3085	...	3638, 3505, 3367, 3218, 3171	N–H/O–H stretch	(9)
...	2882, 2574	...	2888, 2728, 2561	$^{13}\text{C}-\text{H}$ stretch	(9)
2344	2343	2344	2345	$v_3 (\text{CO}_2)$	(4, 5)
2302	...	2304	...	$v_L (^{13}\text{CO}_2)$	(4, 5)
2266	2273	2266	2272	$v_3 (^{13}\text{CO}_2)$ crystalline/amorphous	(4, 5)
...	2183	...	2182	$^{13}\text{C}\equiv\text{N}$ stretch	(7, 8, 9)
...	2108	$v (\text{O}^{13}\text{CN}^-)$	(10)
...	2093	...	2092	$v_1 (^{13}\text{CO})$	(5, 6)
...	1669, 1588	...	1665, 1590	$^{13}\text{C}=\text{O}$ stretch	(9)
1629	...	1629	...	$v_4 (\text{NH}_3)$	(1, 2)

Table 13
(Continued)

40 K		10 K		Assignment	Reference
Before Irradiation	After Irradiation	Before Irradiation	After Irradiation		
Position (cm^{-1})					
...	1496, 1477, 1431, 1380, 1341, 1287	...	1471, 1370, 1354, 1290, 1261	O–H/N–H/ ^{13}C –H deformation	(9)
1068	...	1068	...	v_2 (NH_3)	(1, 2)
...	1043	...	1043	...	(5)
...	1019	...	1107, 1005	^{13}C –N/ ^{13}C –O stretch	(9)
...	835	...	835	^{13}C –H out-of-plane deformation	(9)
651/638	642	652/637	645	v_2 ($^{13}\text{CO}_2$)	(4, 5)

References. (1) J. S. Holt et al. (2004); (2) W. Zheng et al. (2008); (3) W. Zheng et al. (2009b); (4) P. A. Gerakines & R. L. Hudson (2015); (5) H. Carrascosa et al. (2019); (6) C. J. Bennett et al. (2009); (7) F. A. Vasconcelos et al. (2020); (8) M. H. Moore & R. L. Hudson (2003); (9) G. Socrates (2004); (10) C. J. Bennett et al. (2010); (11) C. M. Tonauer et al. (2021).

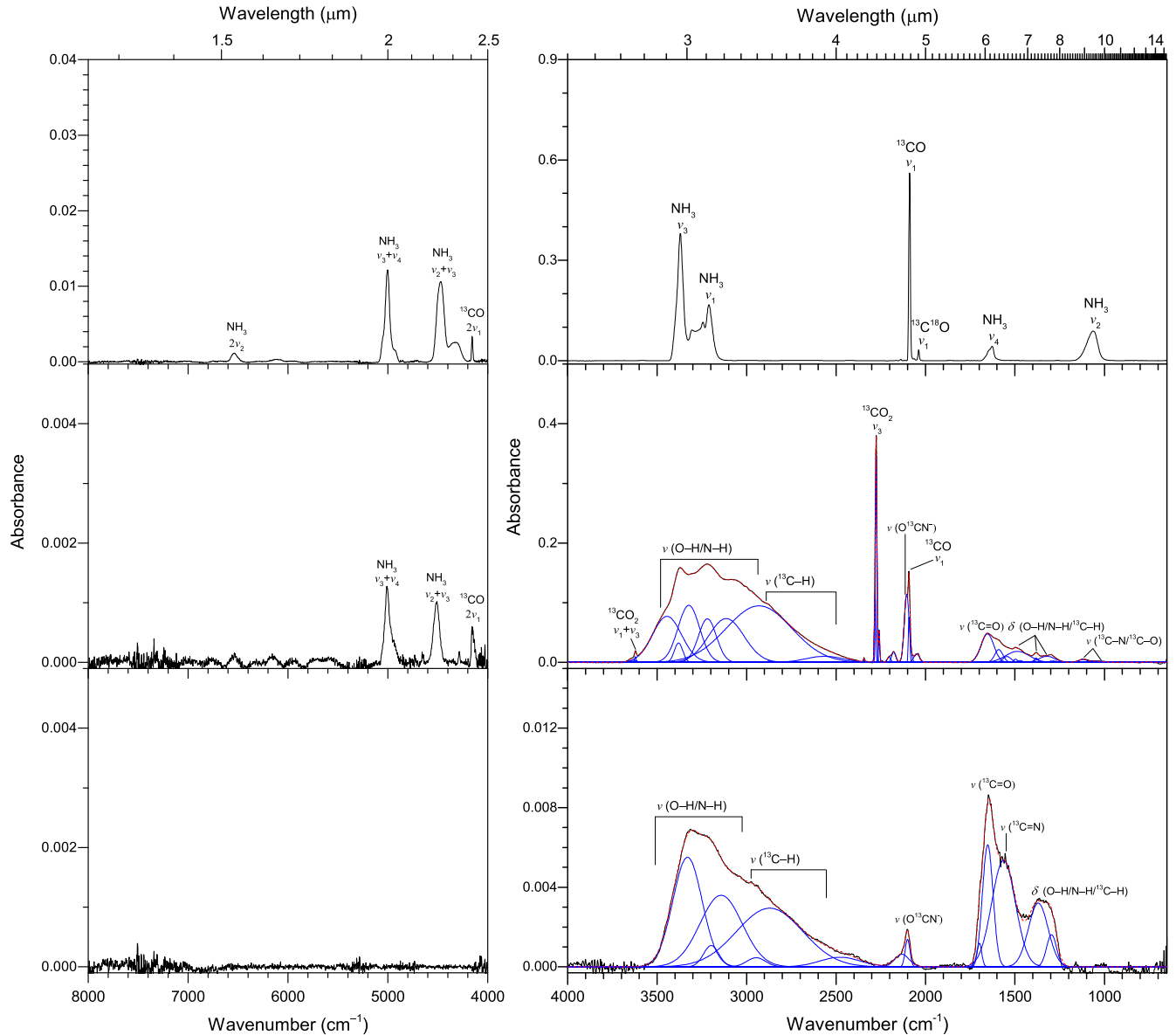


Figure 24. Infrared spectra of ammonia–carbon monoxide (NH_3 – ^{13}CO) ice mixtures before (top) and after (middle) irradiation at 20 K. The 320 K spectra are shown at the bottom. The experimental spectra are plotted in black, the deconvoluted peaks are in blue, and the sums are in red. Only noticeable peaks are labeled for clarity, and detailed peak assignments are listed in Table 12.

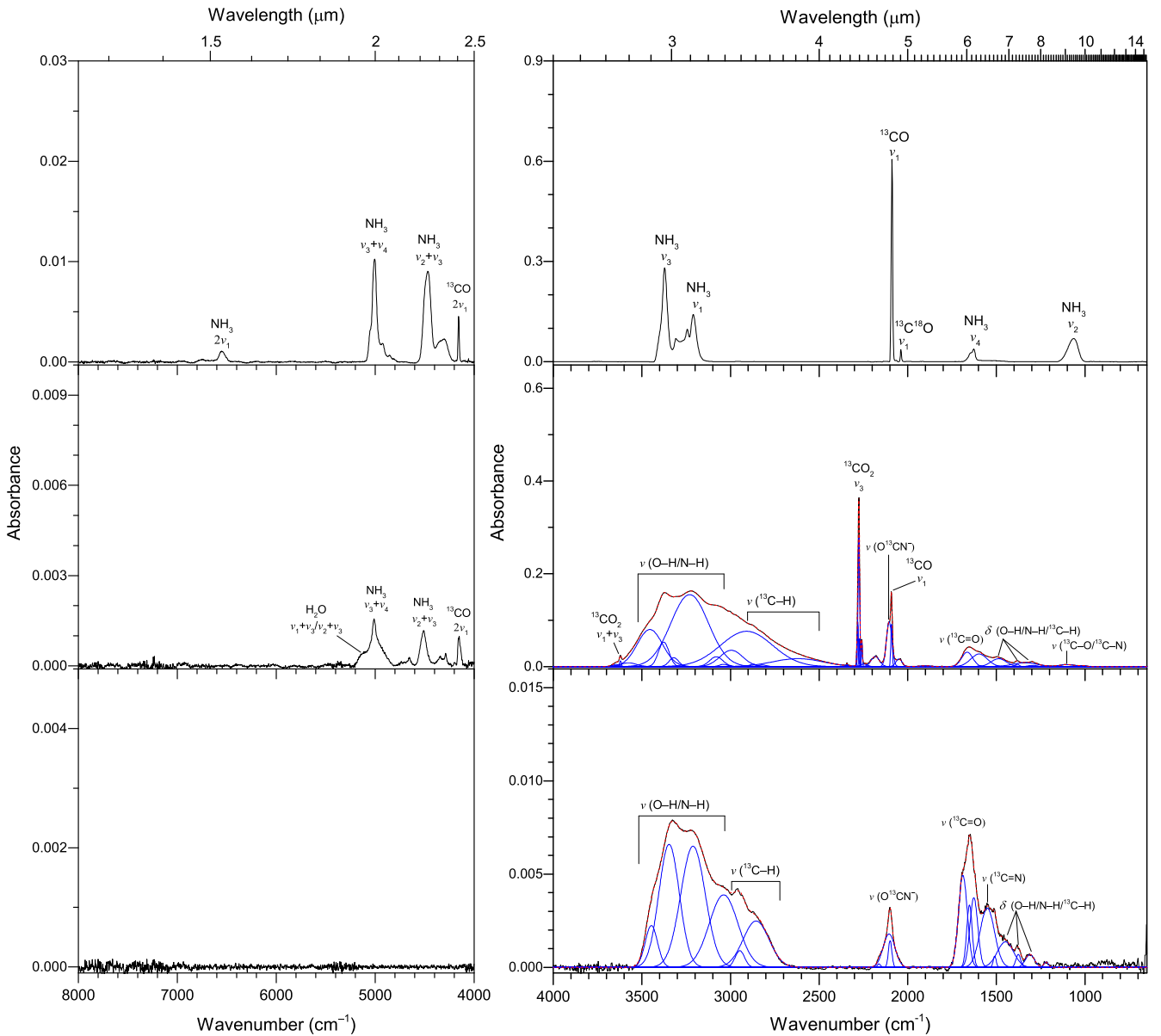


Figure 25. Infrared spectra of ammonia–carbon monoxide (NH_3 – ^{13}CO) ice mixtures before (top) and after (middle) irradiation at 10 K. The 320 K spectra are shown at the bottom. The experimental spectra are plotted in black, the deconvoluted peaks are in blue, and the sums are in red. Only noticeable peaks are labeled for clarity, and detailed peak assignments are listed in Table 12.

methane, carbon monoxide, and carbon dioxide, the pristine spectra are more complex considering the broad bands of the hydroxyl group and the hydrocarbyl group from methanol molecules (Figures 22 and 23, Table 11). After irradiation, except for simple molecules $^{13}\text{CO}_2$, ^{13}CO , and H_2^{13}CO , a variety of products carrying O–H, ^{13}C –H, ^{13}C =O, and ^{13}C –O functional groups are also observed in the spectra, which can result from carriers of hydrocarbons, ethanol, dimethyl ether, sugar-related compounds, and so on (M. J. Abplanalp et al. 2018, 2019a, 2019b; A. Bergantini et al. 2018c; P. V. Zasimov et al. 2023; C. Zhang et al. 2024). Some of the products are refractory and are detected in the 320 K spectra. Note that, because the ices deposited at 20 K (ice 21) have a higher concentration of methane, the residues reveal a higher fraction of the ^{13}C –H groups, and the absorptions of aromatic compounds from irradiated methane are also observed (M. J. Abplanalp et al. 2018; C. Zhang et al. 2023b).

The spectra data of ammonia ices combined ammonia with carbon monoxide, carbon dioxide, and methanol at different temperatures are displayed in Figures 24–29, and the assignments of absorptions are listed in Tables 12–14. The spectra collected from the NH_3 – ^{13}CO system (ices 23 and 24) before irradiation present sharp absorptions from these two molecules (Figures 24 and 25, Table 12). Upon irradiation, the spectra identify simple products of $^{13}\text{CO}_2$, O^{13}CN^- , and H_2^{13}CO along with H_2O ($\sim 5123 \text{ cm}^{-1}$) and a set of new absorptions including broad bands between 3700 and 2500 cm^{-1} associated with N–H, O–H, and ^{13}C –H bonds, as well as their deformation modes between 1500 and 1200 cm^{-1} (G. Socrates 2004). In addition, the bands of the $^{13}\text{C}\equiv\text{N}$, $^{13}\text{C}=\text{N}=\text{N}$, $^{13}\text{C}=\text{O}$, $\text{N}=\text{O}$, $^{13}\text{C}=\text{N}$, and $^{13}\text{C}=\text{O}$ groups are also observed. These groups indicate that complex products have formed as a result of high-energy electron bombardment, such as formamide ($\text{H}^{13}\text{CONH}_2$), carbamic

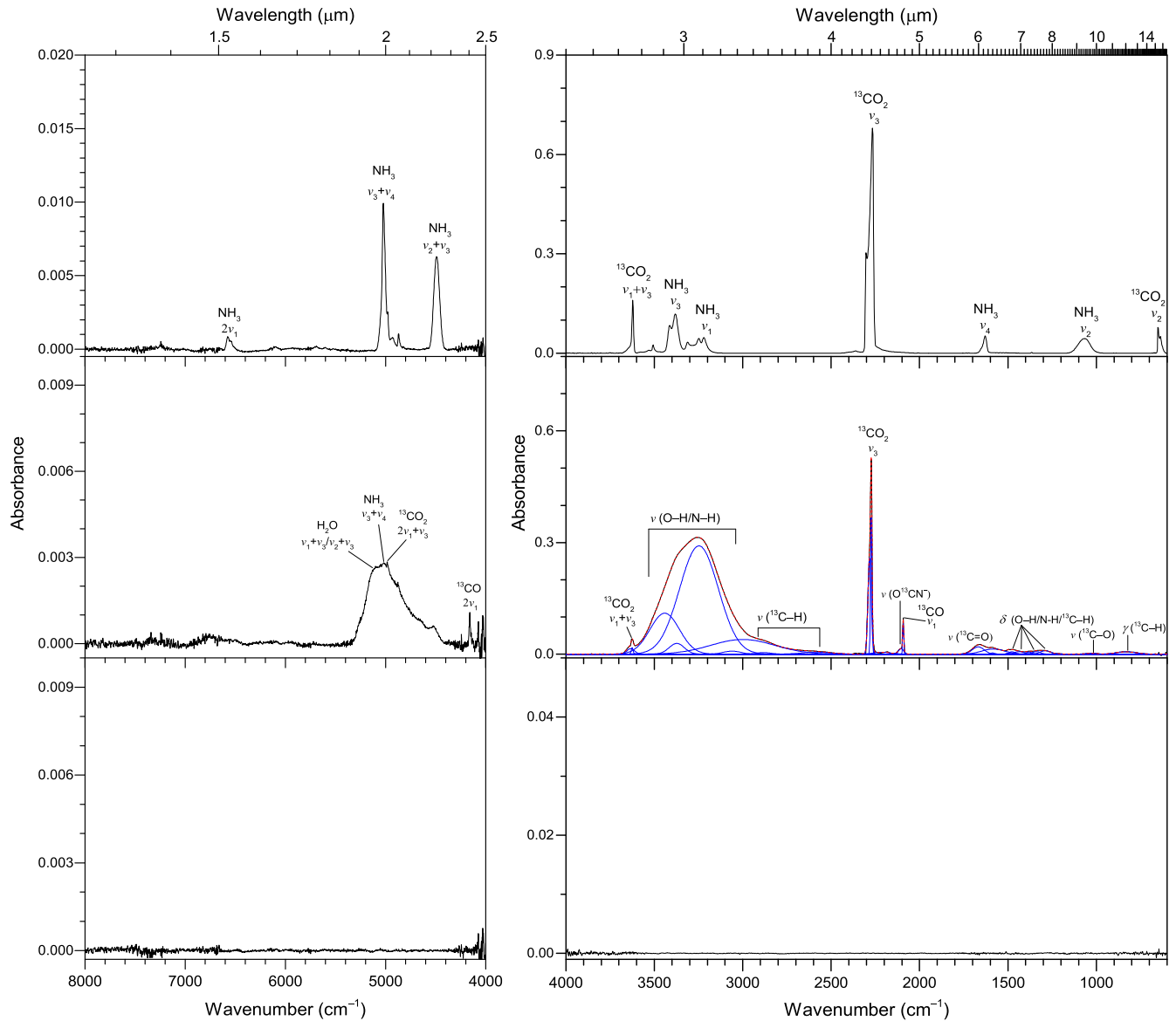


Figure 26. Infrared spectra of ammonia–carbon dioxide ($\text{NH}_3\text{--}^{13}\text{CO}_2$) ice mixtures before (top) and after (middle) irradiation at 40 K. The infrared spectra of the irradiated sample warmed up to 320 K are shown at the bottom. The experimental spectra are plotted in black, the deconvoluted peaks are in blue, and the sums are in red. Only noticeable peaks are labeled for clarity, and detailed peak assignments are listed in Table 13.

acid ($\text{H}_2\text{N}^{13}\text{COOH}$), zwitterionic glycine ($\text{H}_3\text{N}^{+13}\text{CH}_2^{13}\text{COO}^-$), and ammonium carbamate ($([\text{NH}_4]\text{NH}_2^{13}\text{CO}_2)$) (C. J. Bennett et al. 2010; S. Pilling et al. 2010a; R. Martinez et al. 2014; M. Förstel et al. 2016; J. H. Bredehöft et al. 2017; A. L. F. de Barros et al. 2020; A. D. Volosatova et al. 2022). Many of these products remain observable even after being warmed up to 320 K and appear in the spectra in the form of N–H, O–H, ^{13}C –H, $^{13}\text{C}\equiv\text{N}$, and $^{13}\text{C}=\text{O}$ groups (G. Socrates 2004). For the $\text{NH}_3\text{--}^{13}\text{CO}_2$ ice mixtures (ices 25 and 26), the unprocessed spectra only present absorption bands of these two molecules (Figures 26 and 27, Table 13). The irradiated spectra have similar profiles of processed $\text{NH}_3\text{--}^{13}\text{CO}$ ices and detect functional groups of N–H, O–H, ^{13}C –H, $^{13}\text{C}\equiv\text{N}$, and $^{13}\text{C}=\text{O}$ involved in molecules, for example, formamide ($\text{H}^{13}\text{CONH}_2$), carbamic acid ($\text{H}_2\text{N}^{13}\text{COOH}$) and its dimer, ammonium carbamate ($([\text{NH}_4]\text{NH}_2^{13}\text{CO}_2)$, and ammonium formate ($\text{NH}_4\text{H}^{13}\text{CO}_2$) (Y. J. Chen et al. 2007; J. B. Bossa et al. 2008a, 2008b; M. Bertin et al. 2009;

S. Jheeta et al. 2012; X. Y. Lv et al. 2014; J. A. Noble et al. 2014; Y. Rodríguez-Lazcano et al. 2014; Z. Altun et al. 2019; R. L. James et al. 2020, 2021; A. Potapov et al. 2022; J. H. Marks et al. 2023b). However, the signal of $^{13}\text{C}=\text{N}=\text{N}$ and H_2^{13}CO is too low to be identified, and the O^{13}CN^- compounds are only observed in the 40 K spectra. All products sublime when heating to 320 K, which is distinct from the $\text{NH}_3\text{--}^{13}\text{CO}$ system. This suggests that carbon dioxide molecules may not be an effective precursor for producing refractory species in the solar system or interstellar ices. The last ammonia-bearing systems are $\text{NH}_3\text{--}^{13}\text{CH}_3\text{OH}$ mixtures (ices 27 and 28), whose spectra are dominated by the fundamental vibration modes of methanol and ammonia (Figures 28 and 29, Table 14). After being processed by energetic electrons, except for functional groups of hydroxyls, amines, and hydrocarbons, a set of new absorptions resulting from products of $^{13}\text{CO}_2$, ^{13}CO , O^{13}CN^- , H_2^{13}CO , and $^{13}\text{CH}_4$ together with bands of $^{13}\text{C}\equiv\text{N}$, $^{13}\text{C}=\text{N}=\text{N}$, $^{13}\text{C}=\text{O}$, $\text{N}=\text{O}$,

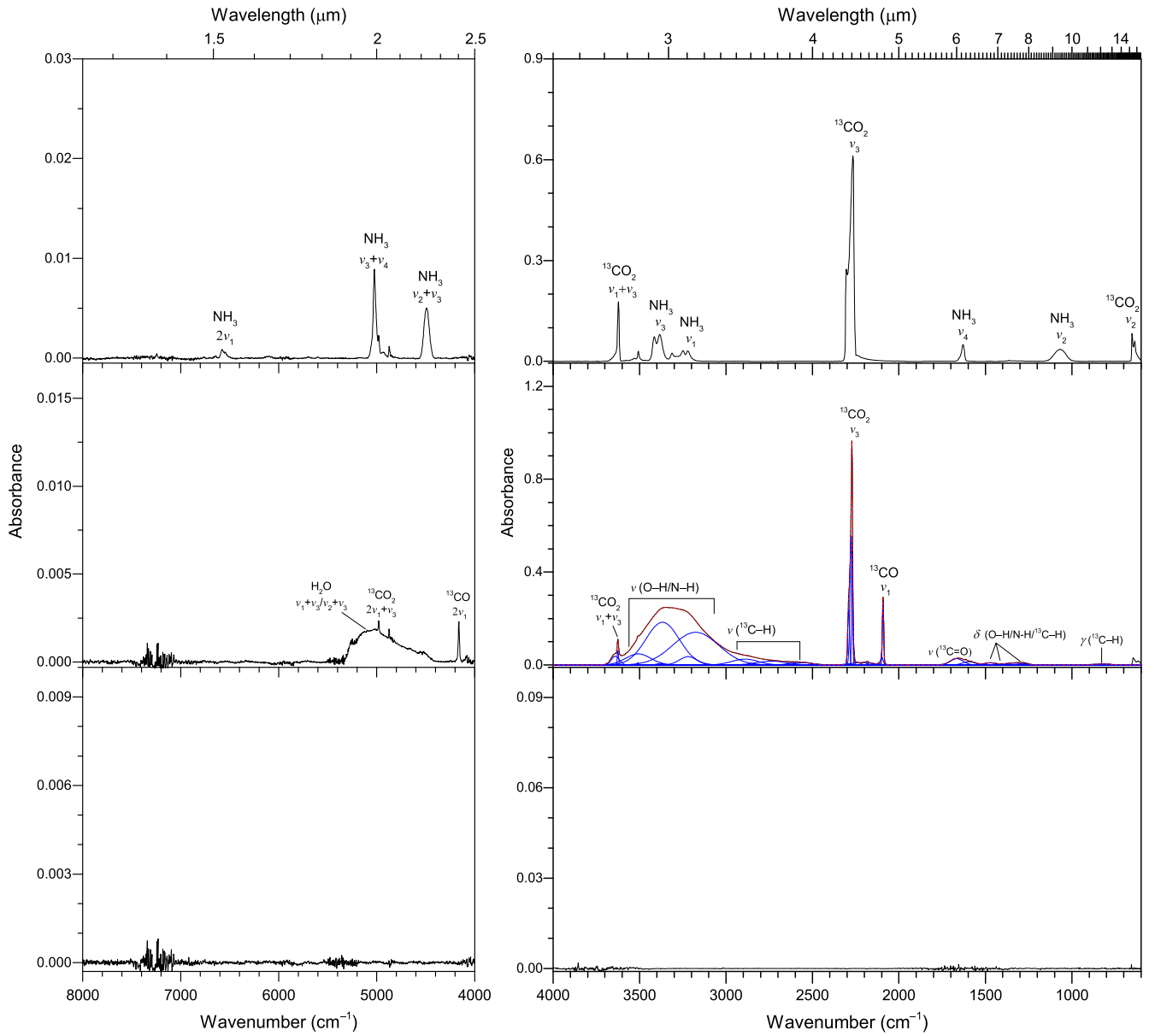


Figure 27. Infrared spectra of ammonia–carbon dioxide ($\text{NH}_3-\text{^{13}CO}_2$) ice mixtures before (top) and after (middle) irradiation at 10 K. The infrared spectra of the irradiated sample warmed up to 320 K are shown at the bottom. The experimental spectra are plotted in black, the deconvoluted peaks are in blue, and the sums are in red. Only noticeable peaks are labeled for clarity, and detailed peak assignments are listed in Table 13.

$^{13}\text{C}-\text{N}$, and $^{13}\text{C}-\text{O}$ stretching vibrations are detected (G. Socrates 2004). These groups can be linked to a suite of species like aldehyde, ketone, sugar-related compounds, carboxylic acid salts, polyoxymethylene, glycolic acid, glycerol, and hexamethylenetetramine (K. I. Öberg et al. 2009; M. Nuevo et al. 2010, 2018; G. Danger et al. 2013; S. Jheeta et al. 2013; V. Vinogradoff et al. 2013; G. M. Muñoz Caro et al. 2014; P. de Marcellus et al. 2015; C. Meinert et al. 2016; M. Farnik et al. 2018; R. G. Urso et al. 2020). Some of them are refractory and are therefore detected in the 320 K spectra.

The infrared spectra of samples composed of carbon monoxide and carbon dioxide (ices 29 and 30) are less complex (Figures 30 and 31, Table 15). Upon irradiation, the spectra reveal products associated with higher-order carbon oxides ($^{13}\text{CO}_x$, $x = 3-6$), similar to those observed

in processed pure carbon dioxide ices (C. Zhang et al. 2025b), which then disappear during heating to 320 K. The infrared spectra of carbon monoxide and carbon dioxide mixed with methanol (ices 31–34) are displayed in Figures 32–35 accompanied by absorption assignments listed in Tables 16–17. Both pristine spectra consist of the absorptions of these three molecules. After being exposed to energetic electrons, their spectra exhibit absorptions from products of $^{13}\text{CO}_2$, ^{13}CO , H^{13}CO , H_2^{13}CO , and $^{13}\text{CH}_4$, along with several intensity bands associated with the O–H, $^{13}\text{C}-\text{H}$, $^{13}\text{C}=\text{O}$, and $^{13}\text{C}-\text{O}$ groups. These groups are potentially combined into many products, including glycolaldehyde, methyl formate, glycolic acid, ester, and so on (C. J. Bennett & R. I. Kaiser 2007b; K. I. Öberg et al. 2009; P. Modica & M. E. Palumbo 2010; S. Maity et al. 2014b, 2015; M. Bertin et al. 2016; N. F. W. Ligterink et al. 2018;

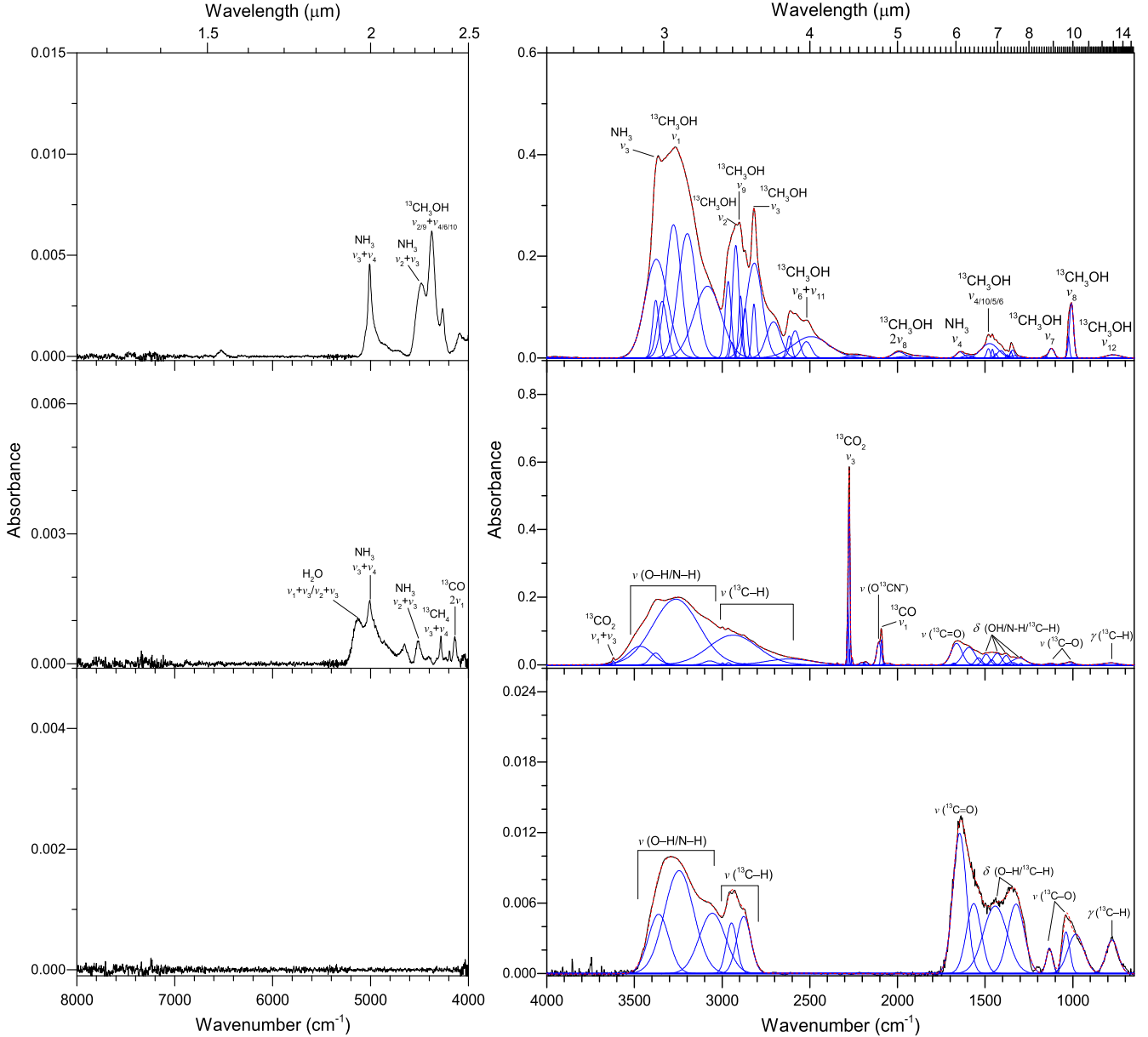


Figure 28. Infrared spectra of ammonia–methanol ($\text{NH}_3-\text{CH}_3\text{OH}$) ice mixtures before (top) and after (middle) irradiation at 40 K. The infrared spectra of processed ices at 320 K are shown at the bottom. The experimental spectra are plotted in black, the deconvoluted peaks are in blue, and the sums are in red. Only noticeable peaks are labeled for clarity, and detailed peak assignments are listed in Table 14.

E. Dartois et al. 2020; F. Schmidt et al. 2021, 2022; J. H. Marks et al. 2023a), which agrees with the detection of broader O–H bands due to this bond in carboxylic acid products participating in hydrogen bonding (G. Socrates 2004). The products from processed $^{13}\text{CO}_2-\text{CH}_3\text{OH}$ ices get lost in the 320 K spectra, but some from $^{13}\text{CO}-\text{CH}_3\text{OH}$ residues are still observed in the spectra. This suggests that, although the products from radiation chemistry in these two systems lead to similar infrared spectra, i.e., similar functional groups, the products are different to some extent. To specifically identify the difference in these products, further research employing in situ mass spectrometry with isomer-selective abilities is necessary and scheduled.

4. Conclusions and Astrophysical Implications

The current study presents comprehensive in situ infrared spectra of TNO-analog ices processed by GCR proxies. This study focuses on the functional groups involved in complex organic products containing carbon, hydrogen, oxygen, and nitrogen resulting from radiation chemistry within ices, which have important implications for interpreting the surface compositions of TNOs derived from telescope data such as Spitzer and JWST (D. P. Cruikshank et al. 2015; W. M. Grundy et al. 2020; C. Lisicki et al. 2020; J. P. Emery et al. 2024; M. N. De Prá et al. 2025; J. Licandro et al. 2025; N. Pinilla-Alonso et al. 2025; S. Protopapa et al. 2024; A. C. Souza-Feliciano et al. 2024), and providing deep insights into the formation and evolution of our solar system.

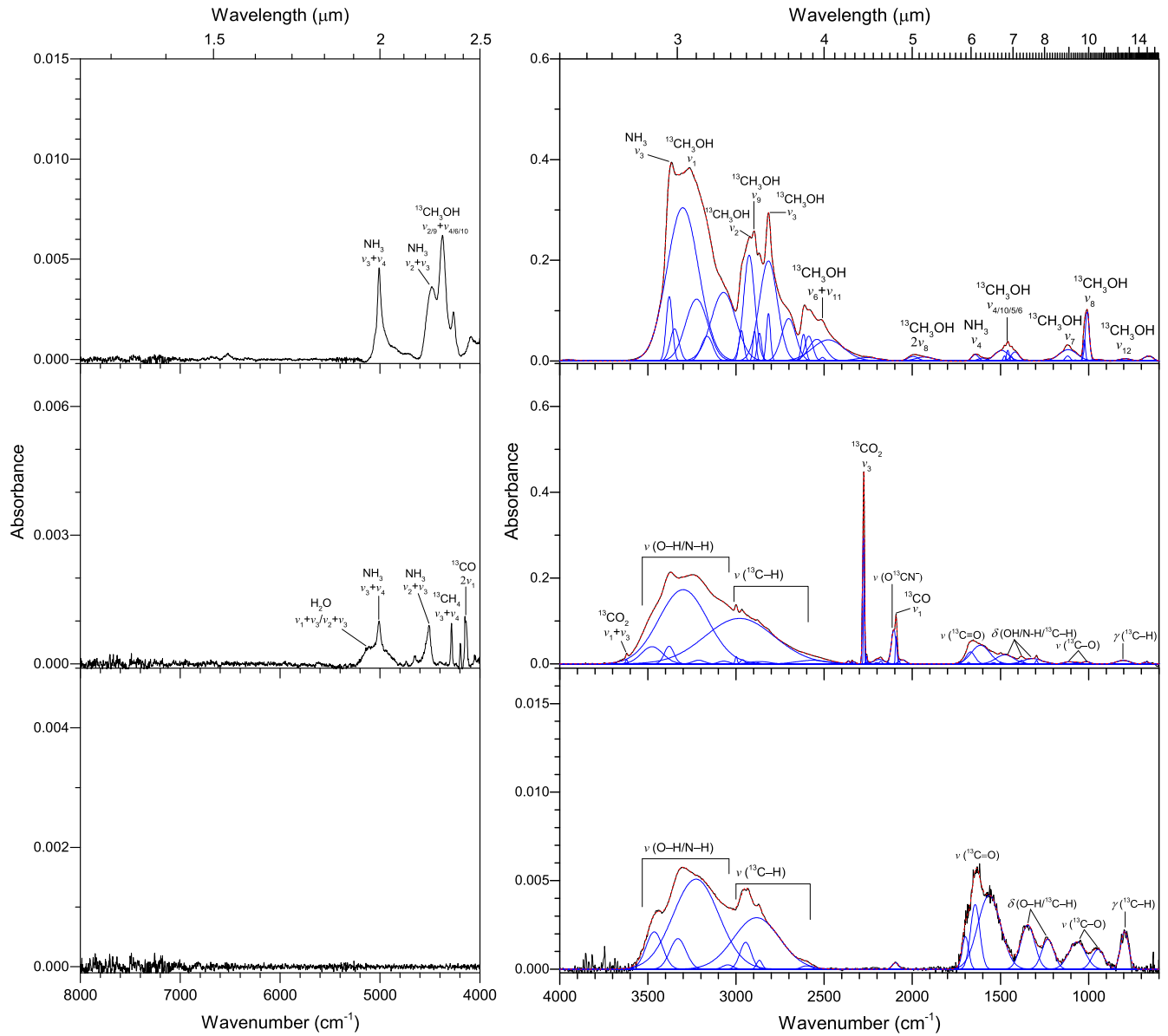


Figure 29. Infrared spectra of ammonia–methanol ($\text{NH}_3-\text{CH}_3\text{OH}$) ice mixtures before (top) and after (middle) irradiation at 10 K. The infrared spectra of processed ices at 320 K are shown at the bottom. The experimental spectra are plotted in black, the deconvoluted peaks are in blue, and the sums are in red. Only noticeable peaks are labeled for clarity, and detailed peak assignments are listed in Table 14.

First, the spectra of water-containing ice mixtures offer compelling evidence that adding different molecules to the water can significantly change the water molecules' order state, as proved by the shifted and broadened absorptions of the dangling OH bond, extending the content of previous similar studies (M. E. Palumbo 2006; M. E. Palumbo et al. 2010; J. He et al. 2018). Second, our results reveal how complex organic species are synthesized by exposing simple carbon-bearing ice mixtures to ionizing irradiation under TNO conditions by identifying related functional groups in the processed infrared spectra. More importantly, a series of functional groups of hydrocarbons ($^{13}\text{C}-\text{H}$), hydroxyl ($\text{O}-\text{H}$), amine ($\text{N}-\text{H}$), carbonyl ($^{13}\text{C}=\text{O}$), imine ($^{13}\text{C}=\text{N}$), cyanate (OCN), nitrile ($^{13}\text{C}\equiv\text{N}$), azide (N_3), diazo ($^{13}\text{C}=\text{N}=\text{N}$), and nitro (NO_2) are formed from irradiated simple molecules (Figure 36) and have access to combine into many potential

species like alcohols, aldehydes, ketones, carboxylic acids, esters, amines, amides, cyanates, and nitriles, among others. These precursors can transfer into more complex species, including important prebiotic molecules like sugar and amino acids, with further reactions to generate macromolecules such as carbohydrates, lipids, nucleic acids, etc. These species are not only relevant to the origin of life but also play an essential role in producing the color diversity of TNOs, considering the formation of large numbers of PAHs and the possible caramelization of sugar-related compounds.

The findings in this study serve as a starting point to fully understand complex compositions and evolutionary processes on the surfaces of TNOs and interstellar grains coated with molecular ices. However, infrared spectroscopy can only detect the presence of new functional groups in deep space ice analogs without sufficient information for identifying specific

Table 14
Infrared Absorption Features of Ammonia–Methanol (NH_3 – $^{13}\text{CH}_3\text{OH}$) Ice Mixtures before and after Irradiation at 40 and 10 K

40 K		10 K				Assignment	Reference
Before Irradiation	After Irradiation	Residue at 320 K	Before Irradiation	After Irradiation	Residue at 320 K		
Position (cm^{-1})							
6525	6526	$2v_1 (\text{NH}_3)$	(1, 2)
...	5150	5108	...	$v_1 + v_2/v_2 + v_3 (\text{H}_2\text{O})$	(3, 15)
5009	5007	...	5009	5010	...	$v_3 + v_4 (\text{NH}_3)$	(1, 2)
...	4653	4740, 4656	...	?	...
4484	4513	...	4484	4509	...	$v_2 + v_3 (\text{NH}_3)$	(1, 2)
4374	4372	$v_{2/9} + v_{4/6/10} (^{13}\text{CH}_3\text{OH})$	(6, 7)
...	4281	4285	...	$v_3 + v_4 (^{13}\text{CH}_4)$	(6, 7, 9)
...	4192	4196	...	$v_1 + v_4 (^{13}\text{CH}_4)$	(6, 7, 9)
4265	4261	$v_{2/9} + v_4 (^{13}\text{CH}_3\text{OH})$	(6, 7)
...	4139	4148	...	$2v_1 (^{13}\text{CO})$	(5, 6, 7, 8)
...	3620	3620	...	$v_1 + v_3 (^{13}\text{CO}_2)$	(4, 5, 6, 7)
...	3473, 3259, 3065	3360, 3242, 3049	...	3478, 3210, 3070, 2973	3467, 3328, 3237	N–H/O–H stretch	(13)
3364	3378	...	3366	3370	...	$v_3 (\text{NH}_3)$	(1, 2)
3342, 3278, 3197, 3083	3345, 3301, 3224, 3068	$v_1 (^{13}\text{CH}_3\text{OH})$	(6, 7)
...	2998, 2966, 2932, 2878, 2605	2957, 2930, 2873	...	2999, 2966, 2879, 2815	2961, 2933, 2873, 2599	$^{13}\text{C}–\text{H}$ stretch	(13)
2964	2973	$v_2 (^{13}\text{CH}_3\text{OH})$	(6, 7)
2921	2920	$v_9 (^{13}\text{CH}_3\text{OH})$	(6, 7)
2819	2815	$v_3 (^{13}\text{CH}_3\text{OH})$	(6, 7)
2699	2696	$2v_6 (^{13}\text{CH}_3\text{OH})$	(6, 7)
2613	2613	$v_4 + v_{7/11} + v_{4/6/10} (^{13}\text{CH}_3\text{OH})$	(6, 7)
2518	2514	$v_6 + v_{11} (^{13}\text{CH}_3\text{OH})$	(6, 7)
2464	2464	$v_6 + v_8 (^{13}\text{CH}_3\text{OH})$	(6, 7)
...	2342	2342	...	$v_3 (\text{CO}_2)$	(4, 5, 6, 7)
...	2275	2275	...	$v_3 (^{13}\text{CO}_2)$	(4, 5, 6, 7)
2238	2238	$2v_{7/11} (^{13}\text{CH}_3\text{OH})$	(6, 7)
...	2180	2180	...	$^{13}\text{C}\equiv\text{N}$ stretch	(11, 12, 13)
...	2105	2105	...	$v (\text{O}^{13}\text{CN}^-)$	(6, 7, 14)
...	2092	2092	2092	$v_1 (^{13}\text{CO})$	(5, 6, 7, 8)
...	2052	2052	...	$^{13}\text{C}=\text{N}=\text{N}$ stretch	(11, 12, 13)
1990	1990	$2v_8 (^{13}\text{CH}_3\text{OH})$	(6, 7)
1640	1641	$v_4 (\text{NH}_3)$	(1, 2)
...	1680, 1662, 1589, 1534	1686, 1527	...	1683, 1668, 1610, 1540	1676, 1587	$^{13}\text{C}=\text{O}/^{13}\text{C}=\text{N}/\text{N}=\text{O}$ stretch	(13)
...	1496	1499	...	$v_3 (\text{H}^{13}\text{CO})$	(6, 7, 10)
1479	1479	$v_4 (^{13}\text{CH}_3\text{OH})$	(6, 7)
1459	1459	$v_{10} (^{13}\text{CH}_3\text{OH})$	(6, 7)
1438	1438	$v_5 (^{13}\text{CH}_3\text{OH})$	(6, 7)
...	1463, 1427, 1378, 1335	1318, 1274	...	1465, 1381, 1323	1346, 1229	O–H/N–H/ ^{13}C –H deformation	(13)
1351	1351	$v_6 (^{13}\text{CH}_3\text{OH})$	(6, 7)
...	1296	1296	...	$v_4 (^{13}\text{CH}_4)$	(6, 7, 9)
1120	1120	$v_7 (^{13}\text{CH}_3\text{OH})$	(6, 7)
...	1013	1033, 985	...	1114, 1082	1066, 950	$^{13}\text{C}–\text{O}$ stretch	(13)
1024	1024	$v_{11} (^{13}\text{CH}_3\text{OH})$	(6, 7)
1008	1009	$v_8 (^{13}\text{CH}_3\text{OH})$	(6, 7)
833	833	$v_{12} (^{13}\text{CH}_3\text{OH})$	(6, 7)
...	778	767	...	819	795	^{13}C –H out-of-plane deformation	(13)

Note. The bands in the residue that remained after the irradiated ice warmed up to 320 K are also listed. ? in column (7) means these peaks are difficult to assign.

References. (1) J. S. Holt et al. (2004); (2) W. Zheng et al. (2008); (3) W. Zheng et al. (2009b); (4) P. A. Gerakines & R. L. Hudson (2015); (5) H. Carrascosa et al. (2019); (6) C. J. Bennett et al. (2007); (7) C. Zhu et al. (2020); (8) C. J. Bennett et al. (2009); (9) C. J. Bennett et al. (2006); (10) M. M. Wohar & P. W. Jagodzinski (1991); (11) F. A. Vasconcelos et al. (2020); (12) M. H. Moore & R. L. Hudson (2003); (13) G. Socrates (2004); (14) C. J. Bennett et al. (2010); (15) C. M. Tonauer et al. (2021).

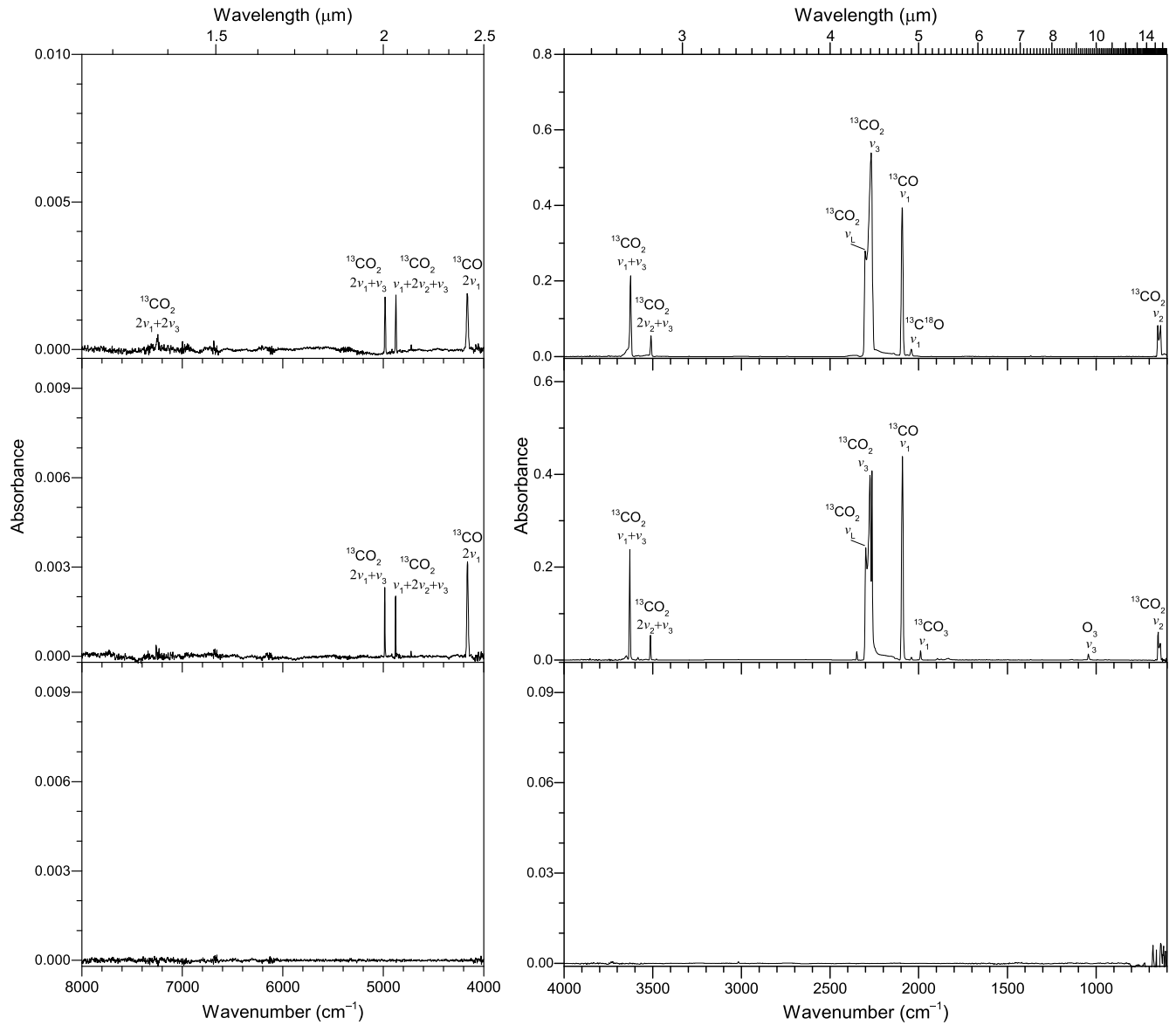


Figure 30. Infrared spectra of monoxide–carbon dioxide ($^{13}\text{CO}-^{13}\text{CO}_2$) ice mixtures before (top) and after (middle) irradiation at 20 K. The infrared spectra of the irradiated sample warmed up to 320 K are also shown at the bottom. Only noticeable peaks are labeled for clarity, and detailed peak assignments are listed in Table 15. L indicates longitudinal.

Table 15
Infrared Absorption Features of Carbon Monoxide–Carbon Dioxide (^{13}CO – $^{13}\text{CO}_2$) Ice Mixtures before and after Irradiation at 20 and 10 K

20 K		10 K		Assignment	Reference
Before Irradiation	After Irradiation	Before Irradiation	After Irradiation		
Position (cm^{-1})					
7244	...	7251	...	$2\nu_1 + 2\nu_3 (^{13}\text{CO}_2)$	(1, 2, 3)
4982	4985	4982	4985	$2\nu_1 + \nu_3 (^{13}\text{CO}_2)$	(1, 2, 3)
4874	4878	4874	4878	$\nu_1 + 2\nu_2 + \nu_3 (^{13}\text{CO}_2)$	(1, 2, 3)
4721	4721	4721	4723	$4\nu_2 + \nu_3 (^{13}\text{CO}_2)$	(1, 2, 3)
4164	4162	4163	4161	$2\nu_1 (^{13}\text{CO})$	(2, 4)
3626	3630	3626	3630	$\nu_1 + \nu_3 (^{13}\text{CO}_2)$	(1, 2, 3)
3510	3513	3510	3514	$2\nu_2 + \nu_3 (^{13}\text{CO}_2)$	(1, 2, 3)
2349	2349	2349	2349	$\nu_3 (\text{CO}_2)$	(1, 2, 3)
2302	2299	2301	2298	$\nu_L (^{13}\text{CO}_2)$	(1, 2, 3)
2268	2274/2264	2268	2274/2264	$\nu_3 (^{13}\text{CO}_2)$ crystalline/amorphous	(1, 2, 3)
2094	2092	2094	2092	$\nu_1 (^{13}\text{CO})$	(2, 4)
2042	2042	2042	2041	$\nu_1 (^{13}\text{C}^{18}\text{O})$	(2, 4)
...	1990	...	1990	$\nu_1 (^{13}\text{CO}_3)$	(3, 5)
...	1894	...	1894	$\nu_1 (^{13}\text{CO}_4)$	(3, 6)

Table 15
(Continued)

20 K		10 K		Assignment	Reference
Before Irradiation	After Irradiation	Before Irradiation	After Irradiation		
Position (cm^{-1})					
...	1874	...	1874	$v_1 (^{13}\text{CO}_5)$	(3, 7)
...	1832	...	1832	$v_1 (^{13}\text{CO}_6)$	(3, 8)
...	1043	...	1043	$v_3 (\text{O}_3)$	(2, 3)
652/637	650/637	651/637	650/636	$v_2 (^{13}\text{CO}_2)$	(1, 2, 3)

References. (1) P. A. Gerakines & R. L. Hudson (2015); (2) H. Carrascosa et al. (2019); (3) C. J. Bennett et al. (2014); (4) C. J. Bennett et al. (2009); (5) C. J. Bennett et al. (2004); (6) C. S. Jamieson et al. (2007b); (7) C. S. Jamieson et al. (2007a); (8) C. S. Jamieson et al. (2008).

Table 16
Infrared Absorption Features of Carbon Monoxide–Methanol ($^{13}\text{CO}-^{13}\text{CH}_3\text{OH}$) Ice Mixtures before and after Irradiation at 20 and 10 K

20 K		10 K				Assignment	Reference
Before Irradiation	After Irradiation	Residue at 320 K	Before Irradiation	After Irradiation	Residue at 320 K		
Position (cm^{-1})							
...	5153	...	$v_1 + v_2/v_2 + v_3 (\text{H}_2\text{O})$	(1, 11)
...	4657	4740, 4657	...	?	...
4386	4383	$v_{2/9} + v_{4/6/10}$ ($^{13}\text{CH}_3\text{OH}$)	(5, 6)
...	4285	4285	...	$v_3 + v_4 (^{13}\text{CH}_4)$	(5, 6, 8)
...	4193	4193	...	$v_1 + v_4 (^{13}\text{CH}_4)$	(5, 6, 8)
4274	4240	$v_{2/9} + v_4 (^{13}\text{CH}_3\text{OH})$	(5, 6)
4153	4159	...	4153	4159	...	$2v_1 (^{13}\text{CO})$	(3, 5, 6, 7)
...	3622	3621	...	$v_1 + v_3 (^{13}\text{CO}_2)$	(2, 3, 4)
...	3648, 3518, 3382, 3236, 3135	3463, 3371, 3238	...	3643, 3493, 3397, 3269, 3068	3444, 3288, 3075	O–H stretch	(10)
3467, 3397, 3255, 3085	3464, 3395, 3268, 3065	$v_1 (^{13}\text{CH}_3\text{OH})$	(5, 6)
...	2999, 2973, 2966, 2932, 2870, 2831, 2731, 2571	2957, 2930, 2870	...	2999, 2973, 2966, 2932, 2879, 2815, 2754, 2552	2946, 2924, 2870	$^{13}\text{C}-\text{H}$ stretch	(10)
2947	2947	$v_2 (^{13}\text{CH}_3\text{OH})$	(5, 6)
2921	2920	$v_9 (^{13}\text{CH}_3\text{OH})$	(5, 6)
2824	2824	$v_3 (^{13}\text{CH}_3\text{OH})$	(5, 6)
2790	2798	$2v_6 (^{13}\text{CH}_3\text{OH})$	(5, 6)
2581	2581	$v_4 + v_{7/11} + v_{4/6/10}$ ($^{13}\text{CH}_3\text{OH}$)	(5, 6)
2511	2512	$v_6 + v_{11} (^{13}\text{CH}_3\text{OH})$	(5, 6)
...	2343	2342	...	$v_3 (\text{CO}_2)$	(2, 3, 4)
...	2275	2274	...	$v_3 (^{13}\text{CO}_2)$	(2, 3, 4)
2208	2208	$2v_{7/11} (^{13}\text{CH}_3\text{OH})$	(5, 6)
...	2166	$^{13}\text{C}\equiv^{13}\text{C}$ stretch	(10)
2137	2137	$v_1 (\text{CO})$	(3, 5, 6, 7)
2088	2093	...	2088	2091	...	$v_1 (^{13}\text{CO})$	(3, 5, 6, 7)
2037	2041	...	2037	2040	...	$v_1 (^{13}\text{C}^{18}\text{O})$	(3, 5, 6, 7)
...	1808	1809	...	$v (\text{H}^{13}\text{CO})$	(5, 6)
...	1677, 1661, 1570	1686, 1527	...	1680, 1668,
1584, 1540	1676, 1587	$^{13}\text{C}=\text{O}$ stretch	10
...	1499	1498	...	$v_3 (\text{H}_2^{13}\text{CO})$	(5, 6, 9)
1474	1474	$v_4 (^{13}\text{CH}_3\text{OH})$	(5, 6)
1460	1459	$v_{10} (^{13}\text{CH}_3\text{OH})$	(5, 6)
1420	1417	$v_5 (^{13}\text{CH}_3\text{OH})$	(5, 6)
...	1453, 1424, 1368	...	1453, 1424, 1368	1448, 1390	...	O–H/ ^{13}C –H deformation	(10)
1407	1407	$v_6 (^{13}\text{CH}_3\text{OH})$	(5, 6)
...	1296	1295	...	$v_4 (^{13}\text{CH}_4)$	(5, 6, 8)
1114	1117	$v_7 (^{13}\text{CH}_3\text{OH})$	(5, 6)

Table 16
(Continued)

20 K			10 K			Assignment	Reference
Before Irradiation	After Irradiation	Residue at 320 K	Before Irradiation	After Irradiation	Residue at 320 K		
Position (cm^{-1})							
...	1261, 1108, 1066, 1009	1261, 1108, 1066, 1009	1278, 1106, 1056	$^{13}\text{C}-\text{O}$ stretch	(10)
1011	1010	v_8 ($^{13}\text{CH}_3\text{OH}$)	(5, 6)
835	833	v_{12} ($^{13}\text{CH}_3\text{OH}$)	(5, 6)
...	761	...		796	...	$^{13}\text{C}-\text{H}$ out-of-plane deformation	(10)

Note. The bands in the residue that remained after the irradiated ice warmed up to 320 K are also listed. ? in column (7) means these peaks are difficult to assign.

References. (1) W. Zheng et al. (2009b); (2) P. A. Gerakines & R. L. Hudson (2015); (3) H. Carrascosa et al. (2019); (4) C. J. Bennett et al. (2014); (5) C. J. Bennett et al. (2007); (6) C. Zhu et al. (2020); (7) C. J. Bennett et al. (2009); (8) C. J. Bennett et al. (2006); (9) M. M. Wohar & P. W. Jagodzinski (1991); (10) G. Socrates (2004); (11) C. M. Tonauer et al. (2021).

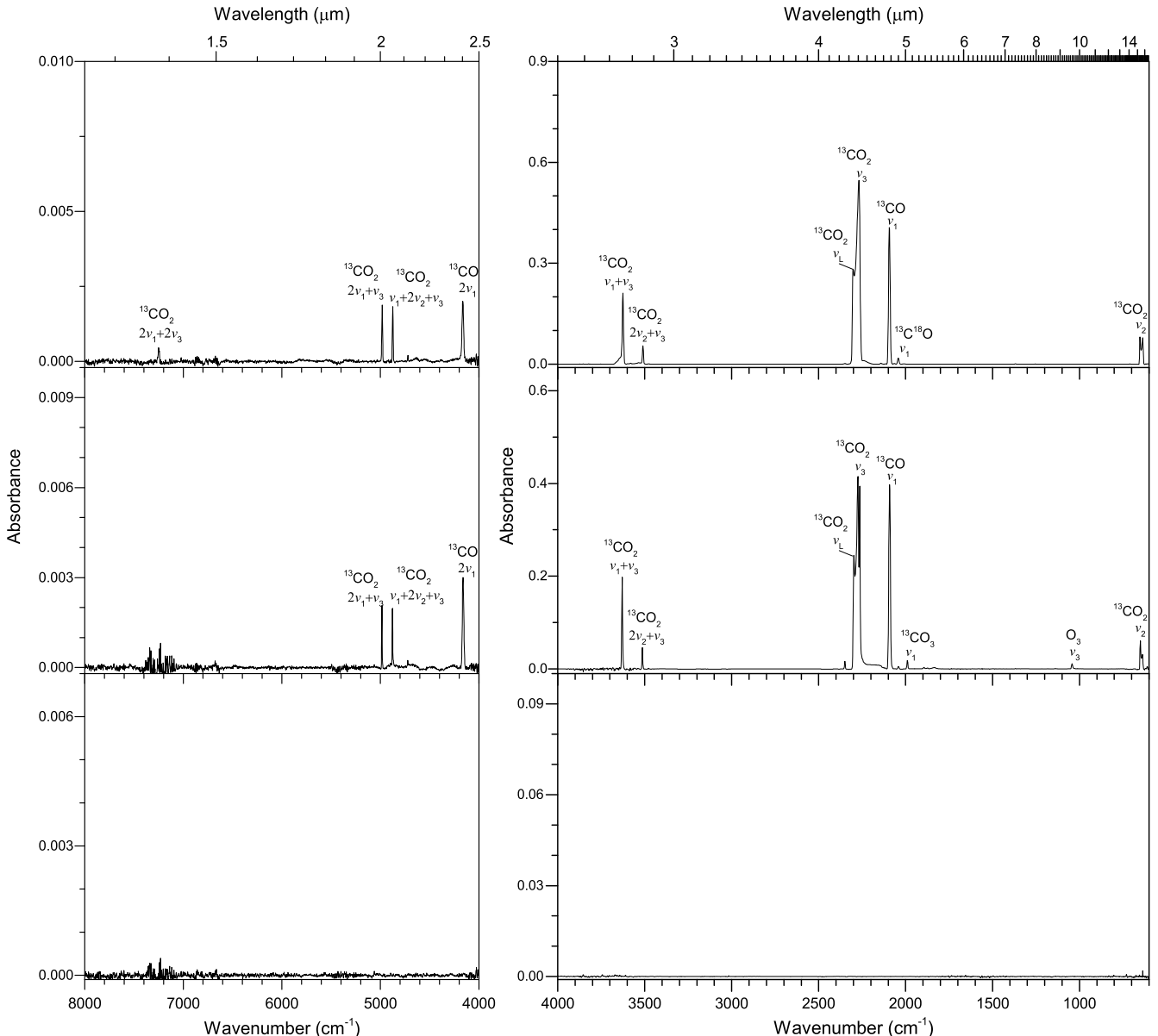


Figure 31. Infrared spectra of monoxide–carbon dioxide ($^{13}\text{CO}-^{13}\text{CO}_2$) ice mixtures before (top) and after (middle) irradiation at 10 K. The infrared spectra of the irradiated sample warmed up to 320 K are also shown at the bottom. Only noticeable peaks are labeled for clarity, and detailed peak assignments are listed in Table 15. L indicates longitudinal.

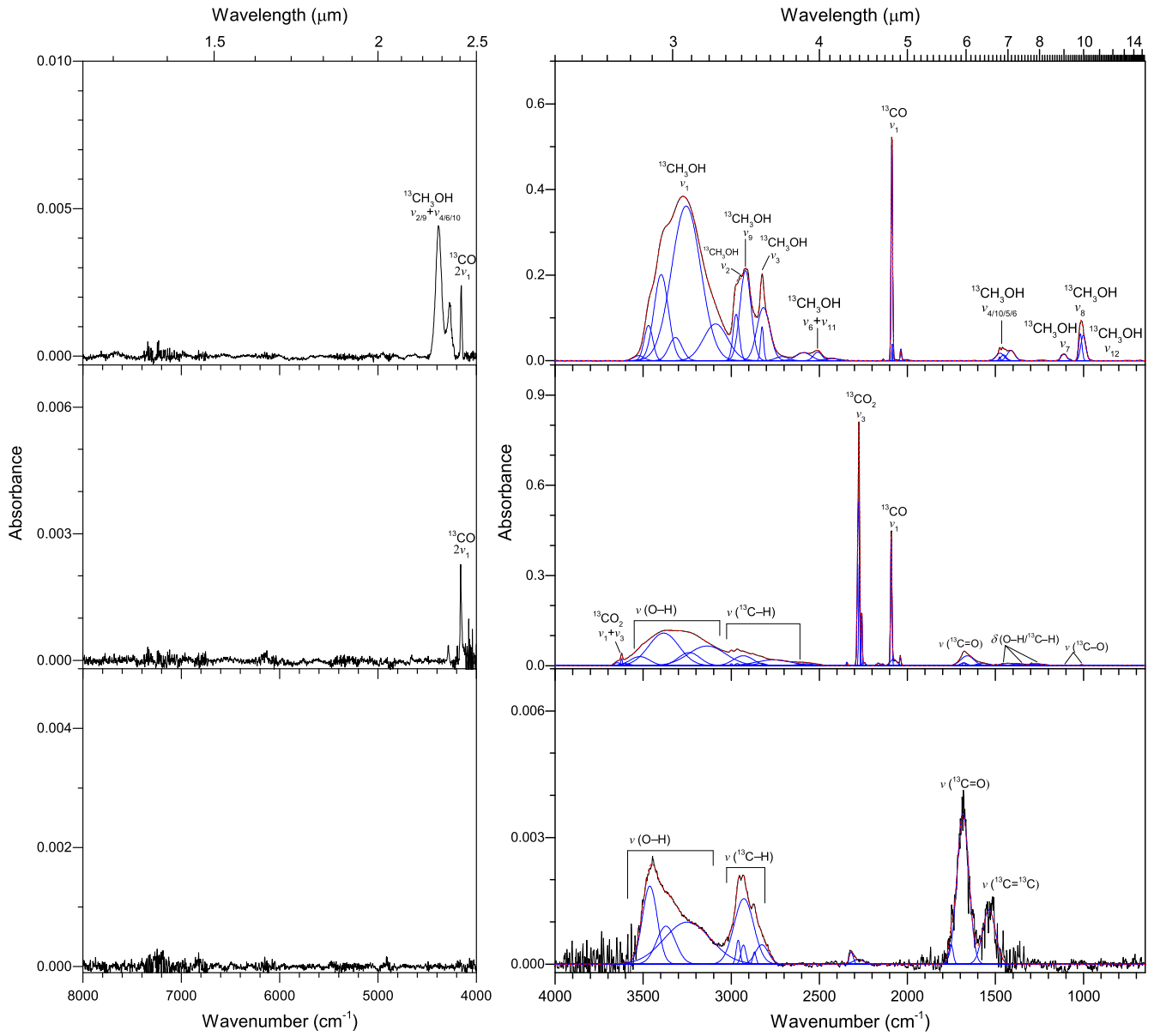


Figure 32. Infrared spectra of carbon monoxide–methanol (^{13}CO — $^{13}\text{CH}_3\text{OH}$) ice mixtures before (top) and after (middle) irradiation at 20 K. The infrared spectra of the irradiated sample warmed up to 320 K are also shown at the bottom. The experimental spectra are plotted in black, the deconvoluted peaks are in blue, and the sums are in red. Only noticeable peaks are labeled for clarity, and detailed peak assignments are listed in Table 16.

molecular products. Consequently, more sensitive experiments are necessary, such as isomer-selective photoionization reflectron time-of-flight mass spectrometry and gas chromatography (C. Meinert & U. J. Meierhenrich 2012; A. M. Turner & R. I. Kaiser 2020). By combining these techniques, further studies have access to catalog compounds from the processed TNO ices at the molecular level, and quantitative analysis of the evolution of key functional groups and molecules is also required to untangle the formation mechanisms of those products.

On the surface of airless TNOs, which have low temperatures ranging from 30 to 50 K, molecules such as water, methane, ammonia, carbon monoxide, carbon dioxide, and methanol have been detected in condensation form (S. Fornasier et al. 2009; M. E. Brown 2012). The long-term irradiation on these small airless objects naturally leads to a set

of complex chemical reactions followed by miscellaneous poorly characterized products. Investigation of radiation chemistry on TNO-analog ices is crucial for understanding the distribution of organics in our solar system, as well as having direct implications for explaining telescope observations, for example, color diversity along with underlying compositions of TNOs (D. C. Jewitt & J. X. Luu 2001; M. A. Barucci et al. 2005; M. E. Brown et al. 2011; A. C. Souza-Feliciano et al. 2024; M. N. De Prá et al. 2025; N. Pinilla-Alonso et al. 2025). The visible reflectance spectral gradient has demonstrated a broad range of colors of TNOs from neutral to ultrared, which is associated with the presence of particular compounds with chromophores, i.e., functional groups of matter responsible for their colors. Previous studies revealed that ionizing radiation exposure on TNO-analog ices results in residues with various colors from neutral to orange

Table 17
Infrared Absorption Features of Carbon Dioxide–Methanol ($^{13}\text{CO}_2$ – $^{13}\text{CH}_3\text{OH}$) Ice Mixtures before and after Irradiation at 40 and 10 K

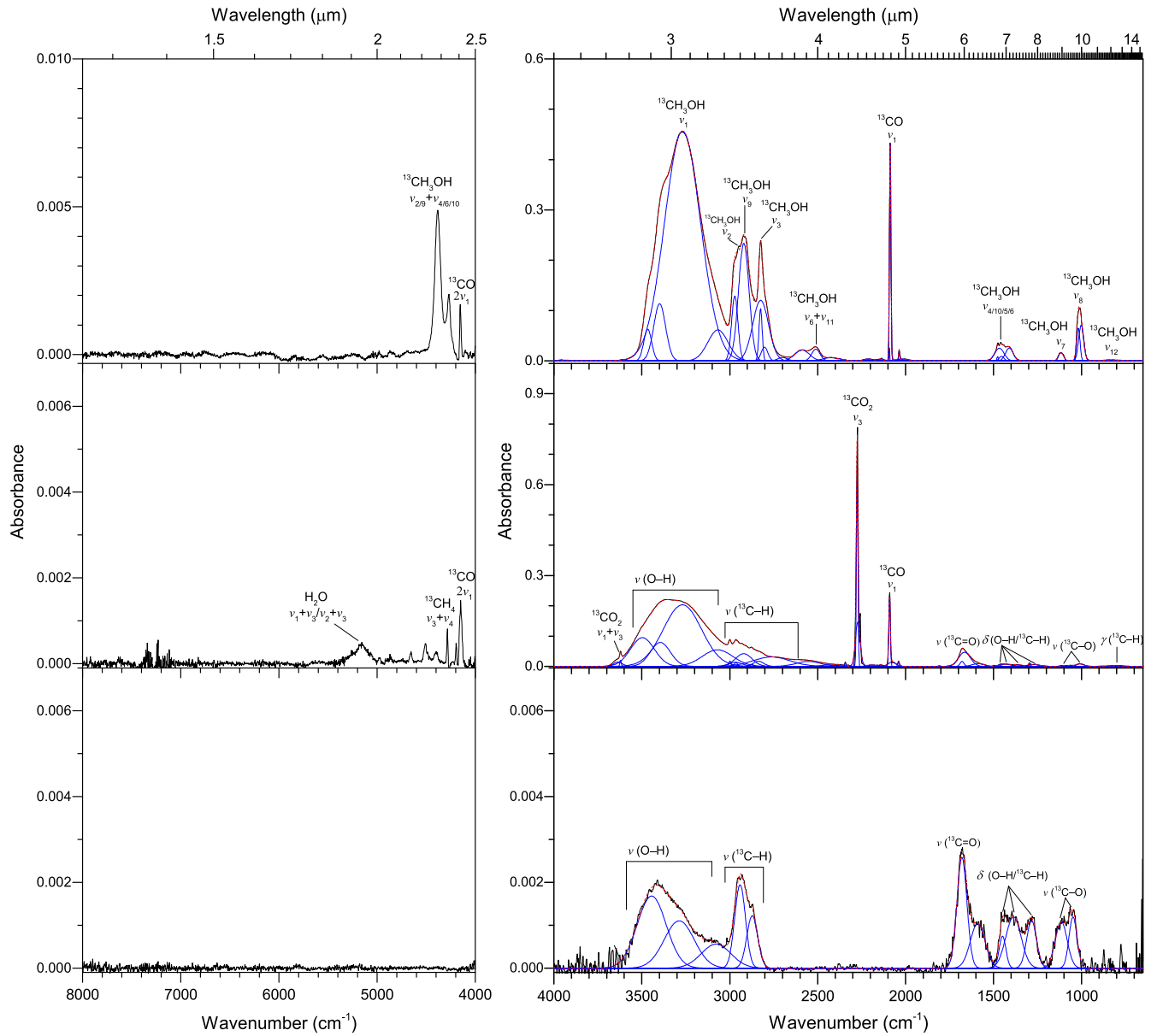
40 K		10 K		Assignment	Reference
Before Irradiation	After Irradiation	Before Irradiation	After Irradiation		
Position (cm^{-1})					
...	5105	...	5119	$v_1 + v_2/v_2 + v_3$ (H_2O)	(1, 2)
...	4665, 4510	...	4662, 4510	?	...
4974	4984	4974	4984	$2v_1 + v_3$ ($^{13}\text{CO}_2$)	(3, 4, 5)
4862	4877	4867	4877	$v_1 + 2v_2 + v_3$ ($^{13}\text{CO}_2$)	(3, 4, 5)
4389	...	4388	...	$v_{2/9} + v_{4/6/10}$ ($^{13}\text{CH}_3\text{OH}$)	(6, 7)
...	4287	$v_3 + v_4$ ($^{13}\text{CH}_4$)	(6, 7, 9)
...	4159	...	4160	$2v_1$ (^{13}CO)	(4, 6, 7, 8)
4278	...	4247	...	$v_{2/9} + v_4$ ($^{13}\text{CH}_3\text{OH}$)	(6, 7)
3621	3627	3621	3623	$v_1 + v_3$ ($^{13}\text{CO}_2$)	(3, 4, 5)
3507	3511	3509	3510	$2v_2 + v_3$ ($^{13}\text{CO}_2$)	(3, 4, 5)
...	3649, 3455, 3388, 3267	...	3639, 3524, 3389, 3240, 3113	O–H stretch	(11)
3405, 3269, 3085	...	3401, 3273, 3205	...	v_1 ($^{13}\text{CH}_3\text{OH}$)	(6, 7)
...	2964, 2892, 2709, 2602, 2562	...	2999, 2966, 2948, 2841, 2551	^{13}C –H stretch	(11)
2978	...	2980	...	v_2 ($^{13}\text{CH}_3\text{OH}$)	(6, 7)
...	...	2952	...	v_4 ($^{13}\text{CH}_3\text{OH}$)	(6, 7)
2923	...	2923	...	v_9 ($^{13}\text{CH}_3\text{OH}$)	(6, 7)
2828	...	2828	...	v_3 ($^{13}\text{CH}_3\text{OH}$)	(6, 7)
2790	...	2798	...	$2v_6$ ($^{13}\text{CH}_3\text{OH}$)	(6, 7)
2580	...	2579	...	$v_4 + v_{7/11} + v_{4/6/10}$ ($^{13}\text{CH}_3\text{OH}$)	(6, 7)
2512	...	2512	...	$v_6 + v_{11}$ ($^{13}\text{CH}_3\text{OH}$)	(6, 7)
2345	2346	2345	2344	v_3 (CO_2)	(3, 4, 5)
2268	2274	2267	2273	v_3 ($^{13}\text{CO}_2$)	(3, 4, 5)
...	2093	...	2091	v_1 (^{13}CO)	(4, 6, 7, 8)
...	2041	...	2040	v_1 ($^{13}\text{C}^{18}\text{O}$)	(4, 6, 7, 8)
2006	...	2008	...	$2v_8$ ($^{13}\text{CH}_3\text{OH}$)	(6, 7)
...	1811	...	1812	v (H^{13}CO)	(6, 7)
...	1678, 1633, 1621	...	1680, 1665, 1585	$^{13}\text{C}=\text{O}/^{13}\text{C}=^{13}\text{C}$ stretch	(11)
...	1499	...	1499	v_3 (H_2^{13}CO)	(6, 7, 10)
1475	...	1475	...	v_4 ($^{13}\text{CH}_3\text{OH}$)	(6, 7)
1461	...	1461	...	v_{10} ($^{13}\text{CH}_3\text{OH}$)	(6, 7)
1418	...	1417	...	v_5 ($^{13}\text{CH}_3\text{OH}$)	(6, 7)
...	1460, 1368, 1277	...	1457, 1377, 1261	O–H/ ^{13}C –H deformation	(11)
1336	...	1336	...	v_6 ($^{13}\text{CH}_3\text{OH}$)	(6, 7)
...	1296	v_4 ($^{13}\text{CH}_4$)	(6, 7, 9)
1114	...	1114	...	v_7 ($^{13}\text{CH}_3\text{OH}$)	(6, 7)
...	1069, 1007	...	1111, 1062, 1009	^{13}C –O stretch	(11)
1009	...	1009	...	v_8 ($^{13}\text{CH}_3\text{OH}$)	(6, 7)
...	862, 791	...	833	^{13}C –H out-of-plane deformation	(11)
835	...	835	...	v_{12} ($^{13}\text{CH}_3\text{OH}$)	(6, 7)
648	...	648	...	v_2 ($^{13}\text{CO}_2$)	(3, 4, 5)

Note. ? in column (5) means these peaks are difficult to assign.

References: (1) W. Zheng et al. (2009b); (2) C. M. Tonauer et al. (2021); (3) P. A. Gerakines & R. L. Hudson (2015); (4) H. Carrascosa et al. (2019); (5) C. J. Bennett et al. (2014); (6) C. J. Bennett et al. (2007); (7) C. Zhu et al. (2020); (8) C. J. Bennett et al. (2009); (9) C. J. Bennett et al. (2006); (10) M. M. Wohar & P. W. Jagodzinski (1991); (11) G. Socrates (2004).

and even dark with different irradiation levels and starting compositions, implying the crucial role of radiation chemistry in producing the color diversity of TNOs (R. Brunetto et al. 2006; M. J. Poston et al. 2018; N. Sakakibara et al. 2020; E. Quirico et al. 2023; C. Zhang et al. 2023b, 2024). Recently, Quirico et al. (2023) employed high-energy heavy ions to process methanol ice to search for the compounds responsible for the reddish surface of Arrokoth and found that the presence of conjugated olefinic groups, which have $\pi \rightarrow \pi^*$ electronic transitions, control the absorption of short wavelengths in the visible spectrum, resulting in the reddish color. Therefore, knowledge of the functional groups on

TNOs is an important step to shed light on corresponding compositions and to constrain a hypothesis for their color diversity (J. Luu & D. Jewitt 1996; R. Gil-Hutton 2002; M. A. Barucci et al. 2005; M. E. Brown et al. 2011). On the other hand, the laboratory exposure time of these ices can be scaled to the time of the radiation processing of a TNO surface; for example, the irradiation dose used here corresponds to some 1800 million years of GCR exposure on the top few hundred nanometers of airless TNOs (J. F. Cooper et al. 2003; M. J. Loeffler et al. 2020; E. Quirico et al. 2023). Therefore, this study provides a detailed data set of functional groups from a complex radiation chemistry



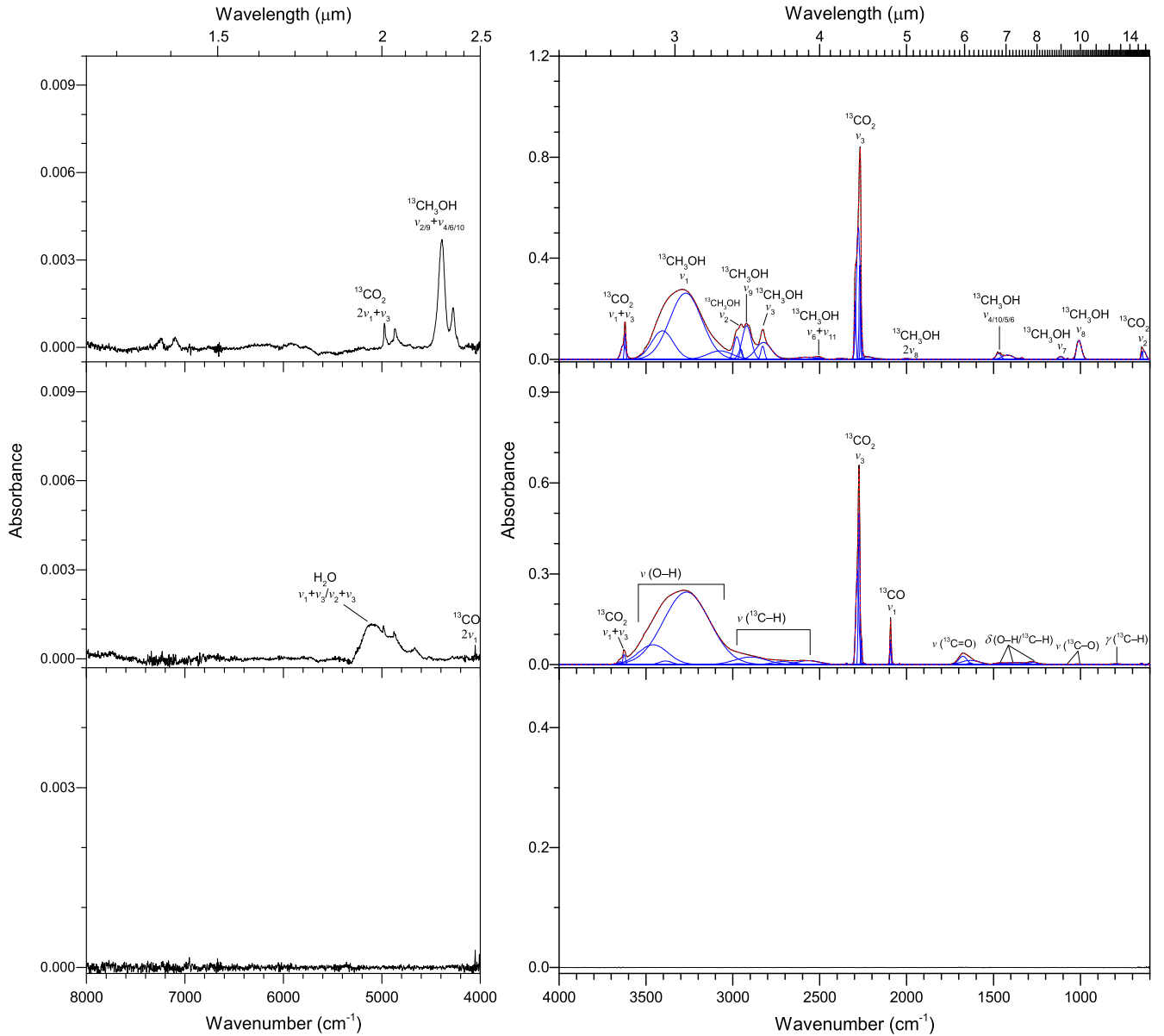


Figure 34. Infrared spectra of carbon dioxide–methanol ($^{13}\text{CO}_2$ – $^{13}\text{CH}_3\text{OH}$) ice mixtures before (top) and after (middle) irradiation at 40 K. The infrared spectra of the irradiated sample warmed up to 320 K are also shown at the bottom. The experimental spectra are plotted in black, the deconvoluted peaks are in blue, and the sums are in red. Only noticeable peaks are labeled for clarity, and detailed peak assignments are listed in Table 17.

and silicate at some TNOs has been reported (J. R. Brucato et al. 2003; M. Fulle 2017; T. Seccull et al. 2018, 2024; A. Mahjoub et al. 2021). Ice mixtures containing H_2S will produce complex sulfur-bearing functional groups of newly formed molecules such as $\text{C}-\text{S}$, $\text{C}=\text{S}$, $\text{C}(\text{O})\text{SH}$, $\text{C}(\text{S})\text{OH}$, and sulfur heteroaromatic species, and, in some scenarios, silicates can facilitate radiation chemical reactions within ices as a catalyst to form macromolecules (T. Seccull et al. 2024;

V. Vinogradoff et al. 2024). Therefore, further experiments are warranted to probe ices mixed with hydrogen sulfide or silicates to catalog compounds on TNOs and underlying formation pathways. These synergistic studies are expected to develop the concept of how complex molecules were synthesized in the outer solar system, ultimately leading to a better understanding of the origin and evolution of our solar system.

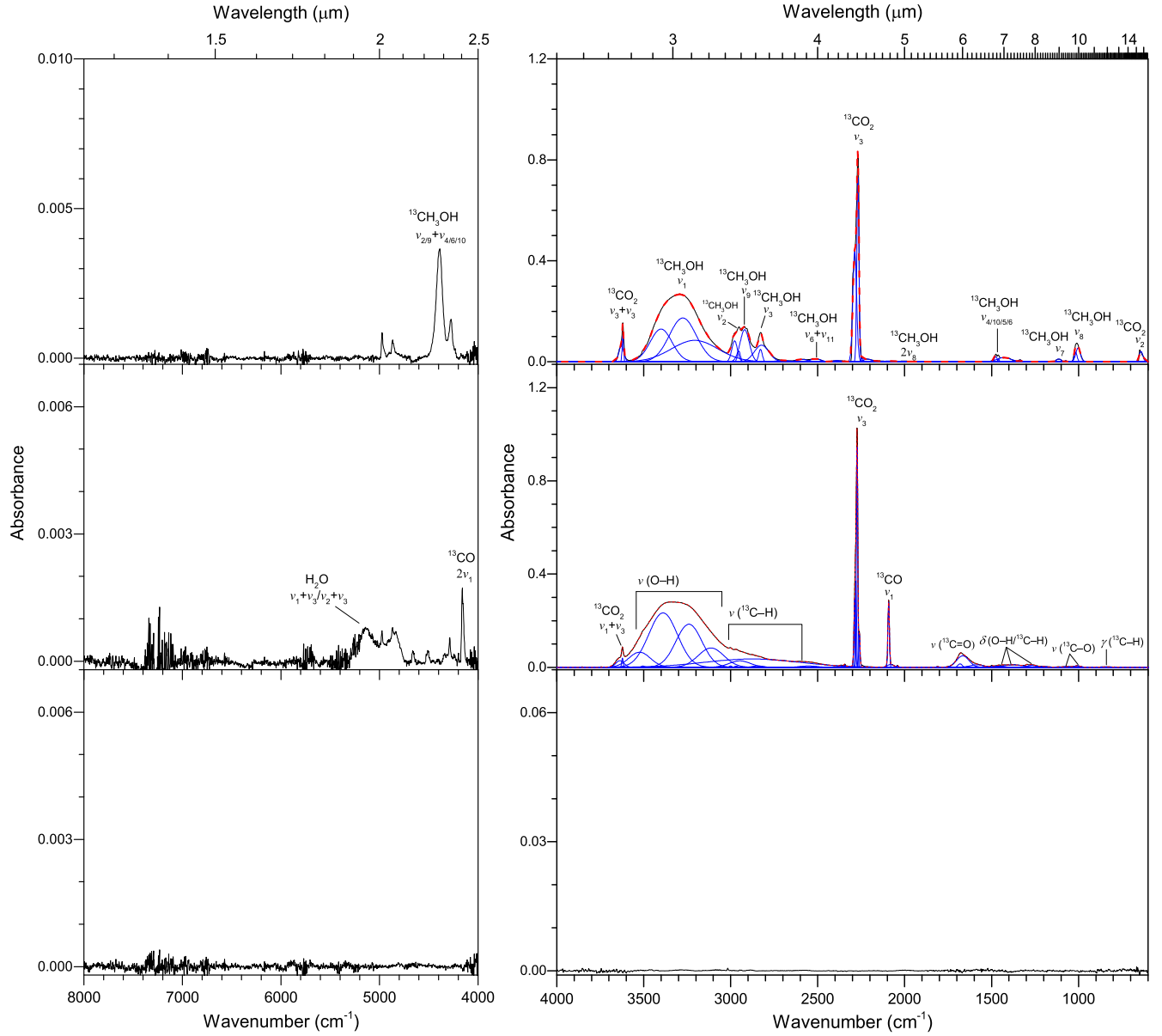


Figure 35. Infrared spectra of carbon dioxide–methanol ($^{13}\text{CO}_2$ – $^{13}\text{CH}_3\text{OH}$) ice mixtures before (top) and after (middle) irradiation at 10 K. The infrared spectra of the irradiated sample warmed up to 320 K are also shown at the bottom. The experimental spectra are plotted in black, the deconvoluted peaks are in blue, and the sums are in red. Only noticeable peaks are labeled for clarity, and detailed peak assignments are listed in Table 17.

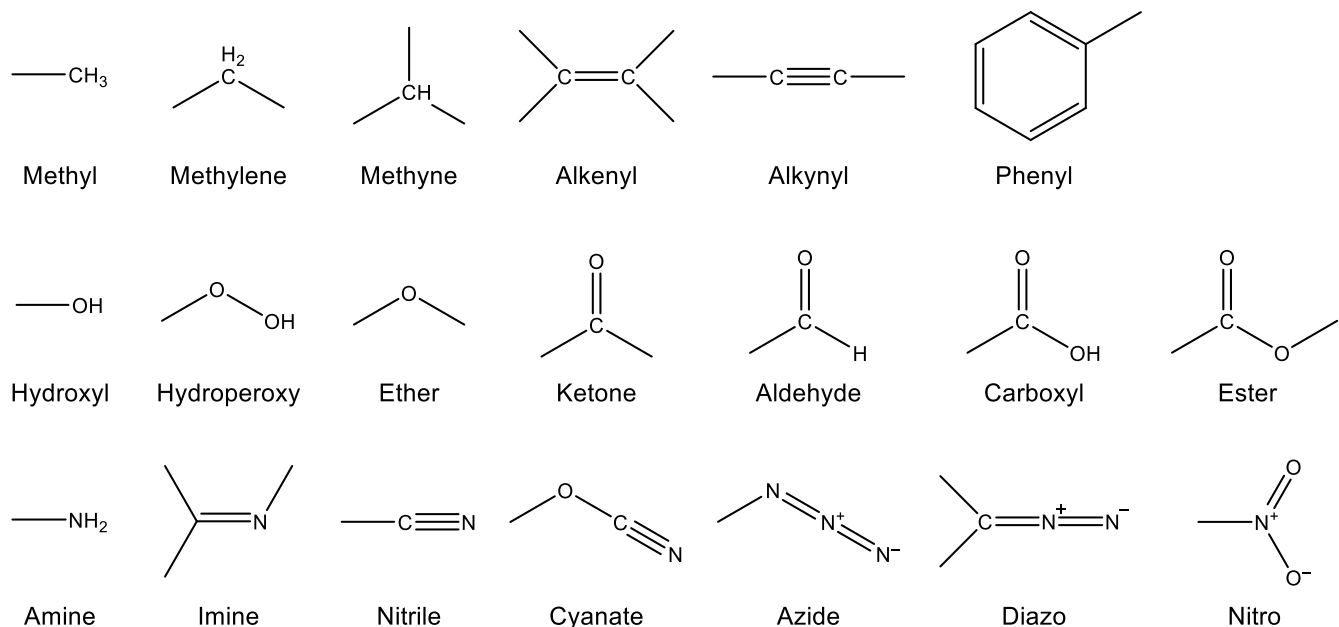


Figure 36. Functional groups identified from the infrared spectra of irradiated TNO ice analogs. These groups can be combined into various compounds, suggesting complex species in the outer solar system. Carbon atoms in all groups are the isotopically labeled 13-carbon.

Acknowledgments

This study was supported by the US National Aeronautics and Space Administration (NASA) under grant Nos. 80NSSC21K1834 and 80NSSC24K1732.

ORCID iDs

Chaojiang Zhang <https://orcid.org/0000-0003-3727-901X>
 Jia Wang <https://orcid.org/0000-0002-3795-8699>
 Leslie A. Young <https://orcid.org/0000-0002-7547-3967>
 Ralf I. Kaiser <https://orcid.org/0000-0002-7233-7206>

References

- Abou Mrad, N., Duvernay, F., Chiavassa, T., & Danger, G. 2016, *MNRAS*, **458**, 1234
 Abplanalp, M. J., Förstel, M., & Kaiser, R. I. 2016a, *CPL*, **644**, 79
 Abplanalp, M. J., Frigge, R., & Kaiser, R. I. 2019a, *SciA*, **5**, eaaw5841
 Abplanalp, M. J., Góbi, S., & Kaiser, R. I. 2019b, *PCCP*, **21**, 5378
 Abplanalp, M. J., Gozem, S., Krylov, A. I., et al. 2016b, *PNAS*, **113**, 7727
 Abplanalp, M. J., Jones, B. M., & Kaiser, R. I. 2018, *PCCP*, **20**, 5435
 Altun, Z., Bleda, E., & Trindle, C. 2019, *Life*, **9**, 34
 Altwegk, K., Balsiger, H., Bar-Nun, A., et al. 2016, *SciA*, **2**, e1600285
 Arumainayagam, C. R., Garrod, R. T., Boyer, M. C., et al. 2019, *ChSRv*, **48**, 2293
 Augé, B., Dartois, E., Engrand, C., et al. 2016, *A&A*, **592**, A99
 Awad, Z., Chigai, T., Kimura, Y., Shalabiea, O. M., & Yamamoto, T. 2005, *ApJ*, **626**, 262
 Baratta, G. A., Domingo, M., Ferini, G., et al. 2003, *NIMB*, **209**, 283
 Baratta, G. A., Leto, G., & Palumbo, M. E. 2002, *A&A*, **384**, 343
 Bartels-Rausch, T., Bergeron, V., Cartwright, J. H. E., et al. 2012, *RvMP*, **84**, 885
 Barucci, M. A., Belskaya, I. N., Fulchignoni, M., & Birlan, M. 2005, *AJ*, **130**, 1291
 Barucci, M. A., & Merlin, F. 2020, in *The Trans-Neptunian Solar System*, ed. D. Prialnik, A. Barucci, & L. Young (1st ed.; Amsterdam: Elsevier), 109
 Barucci, M., Brown, M., Emery, J., & Merlin, F. 2008, in *The Solar System Beyond Neptune*, ed. M. A. Barucci et al. (1st ed.; Tucson, AZ: Univ. Arizona Press), 143
 Behr, P. R., Tribbett, P. D., Robinson, T. D., & Loeffler, M. J. 2020, *ApJ*, **900**, 147
 Bennett, C. J., Chen, S.-H., Sun, B.-J., Chang, A. H. H., & Kaiser, R. I. 2007, *ApJ*, **660**, 1588
 Bennett, C. J., Hama, T., Kim, Y. S., Kawasaki, M., & Kaiser, R. I. 2011, *ApJ*, **727**, 27
 Bennett, C. J., Jamieson, C., Mebel, A. M., & Kaiser, R. I. 2004, *PCCP*, **6**, 735
 Bennett, C. J., Jamieson, C. S., & Kaiser, R. I. 2009, *ApJS*, **182**, 1
 Bennett, C. J., Jamieson, C. S., Osamura, Y., & Kaiser, R. I. 2005, *ApJ*, **624**, 1097
 Bennett, C. J., Jamieson, C. S., Osamura, Y., & Kaiser, R. I. 2006, *ApJ*, **653**, 792
 Bennett, C. J., Jones, B., Knox, E., et al. 2010, *ApJ*, **723**, 641
 Bennett, C. J., & Kaiser, R. I. 2007a, *ApJ*, **660**, 1289
 Bennett, C. J., & Kaiser, R. I. 2007b, *ApJ*, **661**, 899
 Bennett, C. J., Pirim, C., & Orlando, T. M. 2013, *ChRv*, **113**, 9086
 Bergantini, A., Abplanalp, M. J., Pokhilko, P., et al. 2018a, *ApJ*, **860**, 108
 Bergantini, A., Frigge, R., & Kaiser, R. I. 2018b, *ApJ*, **859**, 59
 Bergantini, A., Góbi, S., Abplanalp, M. J., & Kaiser, R. I. 2018c, *ApJ*, **852**, 70
 Bergantini, A., Maksyutenko, P., & Kaiser, R. I. 2017, *ApJ*, **841**, 96
 Bergantini, A., Zhu, C., & Kaiser, R. I. 2018d, *ApJ*, **862**, 140
 Bertin, M., Martin, I., Duvernay, F., et al. 2009, *PCCP*, **11**, 1838
 Bertin, M., Romanzin, C., Doronin, M., et al. 2016, *ApJL*, **817**, L12
 Boogert, A. C. A., Gerakines, P. A., & Whittet, D. C. B. 2015, *ARA&A*, **53**, 541
 Bordalo, V., da Silveira, E. F., Lv, X. Y., et al. 2013, *ApJ*, **774**, 105
 Bossa, J. B., Duvernay, F., Theulé, P., Borget, F., & Chiavassa, T. 2008a, *CP*, **354**, 211
 Bossa, J. B., Theulé, P., Duvernay, F., Borget, F., & Chiavassa, T. 2008b, *A&A*, **492**, 719
 Bouilloud, M., Fray, N., Bénilan, Y., et al. 2015, *MNRAS*, **451**, 2145
 Bouwman, J., Ludwig, W., Awad, Z., et al. 2007, *A&A*, **476**, 995
 Bredehoft, J. H., Böhler, E., Schmidt, F., Borrmann, T., & Swiderek, P. 2017, *ESC*, **1**, 50
 Brown, M. E. 2012, *AREPS*, **40**, 467
 Brown, M. E., Schaller, E. L., & Fraser, W. C. 2011, *ApJL*, **739**, L60
 Brown, R. H., Cruikshank, D. P., & Pendleton, Y. 1999, *ApJL*, **519**, L101
 Brucato, J. R., Strazzulla, G., Baratta, G., Mennella, V., & Colangeli, L. 2003, *EM&P*, **92**, 307
 Brunetto, R., Barucci, M. A., Dotto, E., & Strazzulla, G. 2006, *ApJ*, **644**, 646
 Buch, V., & Devlin, J. P. 1991, *JChPh*, **94**, 4091
 Canta, A., Öberg, K. I., & Rajappan, M. 2023, *ApJ*, **953**, 81
 Carrascosa, H., Hsiao, L. C., Sie, N. E., Muñoz Caro, G. M., & Chen, Y. J. 2019, *MNRAS*, **486**, 1985
 Cartwright, R. J., Villanueva, G. L., Holler, B. J., et al. 2024, *PSJ*, **5**, 60
 Chen, Y. J., Nuevo, M., Hsieh, J. M., et al. 2007, *A&A*, **464**, 253
 Chyba, C. F., Thomas, P. J., Brookshaw, L., & Sagan, C. 1990, *Sci*, **249**, 366
 Chyba, C., & Sagan, C. 1992, *Natur*, **355**, 125
 Cooke, I. R., Fayolle, E. C., & Öberg, K. I. 2016, *ApJ*, **832**, 5

- Cooper, G., Kimmich, N., Belisle, W., et al. 2001, *Natur*, **414**, 879
- Cooper, G., & Rios, A. C. 2016, *PNAS*, **113**, E3322
- Cooper, J. F., Christian, E. R., Richardson, J. D., & Wang, C. 2003, *EM&P*, **92**, 261
- Cronin, J. R., & Pizzarello, S. 1997, *Sci*, **275**, 951
- Cruikshank, D. P., Grundy, W. M., DeMeo, F. E., et al. 2015, *Icar*, **246**, 82
- Cruikshank, D. P., Imanaka, H., & Dalle Ore, C. M. 2005, *AdSpR*, **36**, 178
- Cruikshank, D. P., Materese, C. K., Pendleton, Y. J., et al. 2019, *AsBio*, **19**, 831
- Cuppen, H. M., Linnartz, H., & Ioppolo, S. 2024, *ARA&A*, **62**, 243
- Danger, G., Orthous-Daunay, F. R., de Marcellus, P., et al. 2013, *GeCoA*, **118**, 184
- Dartois, E., Chabot, M., Bacmann, A., et al. 2020, *A&A*, **634**, A103
- de Barros, A. L. F., Bergantini, A., Domaracka, A., et al. 2020, *MNRAS*, **499**, 2162
- de Barros, A. L. F., da Silveira, E. F., Bergantini, A., Rothard, H., & Boduch, P. 2015, *ApJ*, **810**, 156
- de Barros, A. L. F., da Silveira, E. F., Rothard, H., Langlinay, T., & Boduch, P. 2014, *MNRAS*, **443**, 2733
- de Marcellus, P., Meinert, C., Mygorodksa, I., et al. 2015, *PNAS*, **112**, 965
- De Prá, M. N., Hénault, E., Pinilla-Alonso, N., et al. 2025, *NatAs*, **9**, 252
- Drouin, D., Couture, A. R., Joly, D., et al. 2007, *Scanning*, **29**, 92
- Eckhardt, A. K., Bergantini, A., Singh, S. K., Schreiner, P. R., & Kaiser, R. I. 2019, *AngCh*, **58**, 5663
- Ehrenfreund, P., & Charnley, S. B. 2000, *ARA&A*, **38**, 427
- Emery, J. P., Wong, I., Brunetto, R., et al. 2024, *Icar*, **414**, 116017
- Farnik, M., Pysanenko, A., Moriova, K., et al. 2018, *JPCA*, **122**, 8458
- Ferrari, B. C., Slavicsinska, K., & Bennett, C. J. 2021, *AcChr*, **54**, 1067
- Fornasier, S., Barucci, M. A., de Bergh, C., et al. 2009, *A&A*, **508**, 457
- Förstel, M., Bergantini, A., Maksyutenko, P., Góbi, S., & Kaiser, R. I. 2017, *ApJ*, **845**, 83
- Förstel, M., Maksyutenko, P., Jones, B. M., et al. 2016, *ApJ*, **820**, 117
- Fulle, M. 2017, *NatAs*, **1**, 0018
- Furukawa, Y., Chikaraishi, Y., Ohkouchi, N., et al. 2019, *PNAS*, **116**, 24440
- Gálvez, Ó., Maté, B., Herrero, V. J., & Escribano, R. 2009, *ApJ*, **703**, 2101
- Gerakines, P. A., & Hudson, R. L. 2015, *ApJL*, **808**, L40
- Gerakines, P. A., Materese, C. K., & Hudson, R. L. 2023, *MNRAS*, **522**, 3145
- Gerakines, P. A., Moore, M. H., & Hudson, R. L. 2000, *A&A*, **357**, 793
- Gil-Hutton, R. 2002, *P&SS*, **50**, 57
- Gladman, B., & Volk, K. 2021, *ARA&A*, **59**, 203
- Golabek, G. J., & Jutzi, M. 2021, *Icar*, **363**, 114437
- Grant, S. L., van Dishoeck, E. F., Tabone, B., et al. 2023, *ApJL*, **947**, L6
- Grundy, W. M., Bird, M. K., Britt, D. T., et al. 2020, *Sci*, **367**, eaay3705
- Grundy, W. M., Cruikshank, D. P., Gladstone, G. R., et al. 2016, *Natur*, **539**, 65
- Gudipati, M. S., & Castillo-Rogez, J. 2013, The Science of Solar System Ices (1st ed.; New York: Springer)
- Hasegawa, T., Yanagisawa, H., Nagasawa, T., et al. 2024, *ApJ*, **969**, 134
- He, J., Clements, A. R., Emtiaz, S. M., et al. 2019, *ApJ*, **878**, 94
- He, J., Emtiaz, S. M., & Vidali, G. 2018, *ApJ*, **863**, 156
- Heavens, O. S. 1955, Optical Properties of Thin Solid Films (1st ed.; New York: Dover)
- Hollenberg, J. L., & Dows, D. A. 1961, *JChPh*, **34**, 1061
- Holt, J. S., Sadoskas, D., & Pursell, C. J. 2004, *JChPh*, **120**, 7153
- Huang, C. H., Cecchi-Pestellini, C., Ciaravella, A., et al. 2022, *MNRAS*, **517**, 3078
- Hudson, R., Palumbo, M. E., Strazzulla, G., et al. 2008, in The Solar System Beyond Neptune, ed. M. A. Barucci et al. (1st ed.; Tucson, AZ: Univ. Arizona Press), 507
- Hudson, R. L. 2018, *ApJ*, **867**, 160
- Hudson, R. L., Gerakines, P. A., & Yarnall, Y. Y. 2022, *ApJ*, **925**, 156
- Hudson, R. L., Gerakines, P. A., & Yarnall, Y. Y. 2024, *ApJ*, **970**, 108
- Hudson, R. L., Loeffler, M. J., Ferrante, R. F., Gerakines, P. A., & Coleman, F. M. 2020, *ApJ*, **891**, 22
- Hudson, R. L., & Moore, M. H. 2005, in IAU Symp. 231, Astrochemistry: Recent Successes and Current Challenges, ed. D. C. Lis et al. (Cambridge: Cambridge Univ. Press), 247
- James, R. L., Ioppolo, S., Hoffmann, S. V., et al. 2020, *RSCAd*, **10**, 37515
- James, R. L., Ioppolo, S., Hoffmann, S. V., et al. 2021, *RSCAd*, **11**, 33055
- Jamieson, C. S., Bennett, C. J., Mebel, A. M., & Kaiser, R. I. 2005, *ApJ*, **624**, 436
- Jamieson, C. S., Mebel, A. M., & Kaiser, R. I. 2006a, *ChemPhysChem*, **7**, 2508
- Jamieson, C. S., Mebel, A. M., & Kaiser, R. I. 2006b, *ApJS*, **163**, 184
- Jamieson, C. S., Mebel, A. M., & Kaiser, R. I. 2007a, *CPL*, **443**, 49
- Jamieson, C. S., Mebel, A. M., & Kaiser, R. I. 2007b, *CPL*, **440**, 105
- Jamieson, C. S., Mebel, A. M., & Kaiser, R. I. 2008, *CPL*, **450**, 312
- Jewitt, D., & Luu, J. 1993, *Natur*, **362**, 730
- Jewitt, D. C., & Luu, J. X. 2001, *AJ*, **122**, 2099
- Jheeta, S., Domaracka, A., Ptasińska, S., Sivaraman, B., & Mason, N. J. 2013, *CPL*, **556**, 359
- Jheeta, S., Ptasińska, S., Sivaraman, B., & Mason, N. J. 2012, *CPL*, **543**, 208
- Jiménez-Escobar, A., Chen, Y. J., Ciaravella, A., et al. 2016, *ApJ*, **820**, 25
- Johnson, R. E. 1990, Energetic Charged-particle Interactions with Atmospheres and Surfaces (1st ed.; Berlin: Springer)
- Johnson, R. E. 1991, *JGR*, **96**, 17553
- Jones, B. M., & Kaiser, R. I. 2013, *JPCL*, **4**, 1965
- Kaiser, R. I., Maity, S., & Jones, B. M. 2014, *PCCP*, **16**, 3399
- Kaiser, R. I., & Mebel, A. M. 2008, *CPL*, **465**, 1
- Kaiser, R. I., Zheng, W., Osamura, Y., & Chang, A. H. 2011, *PCCP*, **13**, 15747
- Kim, Y. S., & Kaiser, R. I. 2010, *ApJ*, **725**, 1002
- Kim, Y. S., & Kaiser, R. I. 2011, *ApJ*, **729**, 68
- Kim, Y. S., & Kaiser, R. I. 2012, *ApJ*, **758**, 37
- Kim, Y. S., Zhang, F., & Kaiser, R. I. 2011, *PCCP*, **13**, 15766
- Kipfer, K. A., Galli, A., Riedo, A., et al. 2024, *Icar*, **410**, 115742
- Kleimeier, N. F., & Kaiser, R. I. 2022, *JPCL*, **13**, 229
- Kleimeier, N. F., Liu, Y., Turner, A. M., et al. 2022, *PCCP*, **24**, 1424
- Krim, L., & Jonusas, M. 2019, *LTP*, **45**, 606
- Kundu, S., Prabhudesai, V. S., & Krishnakumar, E. 2017, *PCCP*, **19**, 25723
- Licandro, J., Pinilla-Alonso, N., Holler, B. J., et al. 2025, *NatAs*, **9**, 245
- Ligterink, N. F. W., Walsh, C., Bhuij, R. G., et al. 2018, *A&A*, **612**, A88
- Lisse, C., Bauer, J., Cruikshank, D., et al. 2020, *NatAs*, **4**, 930
- Loeffler, M. J., & Baragiola, R. A. 2010, *JChPh*, **133**, 214506
- Loeffler, M. J., Raut, U., & Baragiola, R. A. 2010, *JChPh*, **132**, 054508
- Loeffler, M. J., Tribbett, P. D., Cooper, J. F., & Sturmer, S. J. 2020, *Icar*, **351**, 113943
- Luu, J., & Jewitt, D. 1996, *AJ*, **112**, 2310
- Luu, J. X., & Jewitt, D. C. 2002, *ARA&A*, **40**, 63
- Lv, X. Y., Boduch, P., Ding, J. J., et al. 2014, *PCCP*, **16**, 3433
- Mahjoub, A., Brown, M. E., Poston, M. J., et al. 2021, *ApJL*, **914**, L31
- Maity, S., Kaiser, R. I., & Jones, B. M. 2014a, *ApJ*, **789**, 36
- Maity, S., Kaiser, R. I., & Jones, B. M. 2014b, *FaDi*, **168**, 485
- Maity, S., Kaiser, R. I., & Jones, B. M. 2015, *PCCP*, **17**, 3081
- Marks, J. H., Wang, J., Evseev, M. M., et al. 2023a, *ApJ*, **942**, 43
- Marks, J. H., Wang, J., Sun, B. J., et al. 2023b, *ACSCS*, **9**, 2241
- Martín-Doménech, R., Cruz-Díaz, G. A., & Muñoz Caro, G. M. 2018, *MNRAS*, **473**, 2575
- Martinez, R., Bordalo, V., da Silveira, E. F., & Boechat-Roberty, H. M. 2014, *MNRAS*, **444**, 3317
- Materese, C. K., Cruikshank, D. P., Sandford, S. A., et al. 2014, *ApJ*, **788**, 111
- Materese, C. K., Cruikshank, D. P., Sandford, S. A., Imanaka, H., & Nuevo, M. 2015, *ApJ*, **812**, 150
- McClure, M. K., Rocha, W. R. M., Pontoppidan, K. M., et al. 2023, *NatAs*, **7**, 431
- Meinert, C., & Meierhenrich, U. J. 2012, *AngCh*, **51**, 10460
- Meinert, C., Mygorodksa, I., de Marcellus, P., et al. 2016, *Sci*, **352**, 208
- Mejía, C., de Barros, A. L. F., Rothard, H., Boduch, P., & da Silveira, E. F. 2020, *ApJ*, **894**, 132
- Menten, S. M., Sori, M. M., & Bramson, A. M. 2022, *NatCo*, **13**, 4457
- Métayer, R., Guibert-Lepoutre, A., Ferruit, P., et al. 2019, *FrASS*, **6**, 8
- Mifsud, D. V., Herczeg, P., Sulik, B., et al. 2023, *Atoms*, **11**, 19
- Modica, P., & Palumbo, M. E. 2010, *A&A*, **519**, A22
- Moore, M. H., Ferrante, R. F., Hudson, R. L., & Stone, J. N. 2007, *Icar*, **190**, 260
- Moore, M. H., Ferrante, R. F., & Nuth, J. A. 1996, *P&SS*, **44**, 927
- Moore, M. H., & Hudson, R. L. 2003, *Icar*, **161**, 486
- Moore, M. H., Hudson, R. L., & Ferrante, R. F. 2003, *EM&P*, **92**, 291
- Muñoz Caro, G. M., Dartois, E., Boduch, P., et al. 2014, *A&A*, **566**, A93
- Nayak, O., Hirschauer, A. S., Kavanagh, P. J., et al. 2024, *ApJ*, **963**, 94
- Nesvorný, D. 2018, *ARA&A*, **56**, 137
- Nesvorný, D., Li, R., Youdin, A. N., Simon, J. B., & Grundy, W. M. 2019, *NatAs*, **3**, 808
- Nesvorný, D., Vokrouhlický, D., Dones, L., et al. 2017, *ApJ*, **845**, 27
- Neubeck, A., & McMahon, S. 2022, Prebiotic Chemistry and the Origin of Life (1st ed.; Cham: Springer)
- Noble, J. A., Fraser, H. J., Smith, Z. L., et al. 2024, *NatAs*, **8**, 1169
- Noble, J. A., Theule, P., Duvernay, F., et al. 2014, *PCCP*, **16**, 23604
- Nuevo, M., Bredehöft, H. J., Meierhenrich, U. J., d'Hendecourt, L., & Thiemann, W. H. P. 2010, *AsBio*, **10**, 245
- Nuevo, M., Cooper, G., & Sandford, S. A. 2018, *NatCo*, **9**, 5276
- Oba, Y., Takano, Y., Naraoka, H., Watanabe, N., & Kouchi, A. 2019, *NatCo*, **10**, 4413

- Öberg, K. I., Facchini, S., & Anderson, D. E. 2023, *ARA&A*, **61**, 287
- Öberg, K. I., Fraser, H. J., Boogert, A. C. A., et al. 2007, *A&A*, **462**, 1187
- Öberg, K. I., Garrod, R. T., van Dishoeck, E. F., & Linnartz, H. 2009, *A&A*, **504**, 891
- Palumbo, M. E. 2006, *A&A*, **453**, 903
- Palumbo, M. E., Baratta, G. A., Leto, G., & Strazzulla, G. 2010, *JMoSt*, **972**, 64
- Parent, P., Bournel, F., Lasne, J., et al. 2009, *JChPh*, **131**, 154308
- Pasek, M., & Lauretta, D. 2008, *OLEB*, **38**, 5
- Peeters, Z., Hudson, R. L., Moore, M. H., & Lewis, A. 2010, *Icar*, **210**, 480
- Phua, Y. Y., Sakakibara, N., Ito, T., & Terashima, K. 2022, *Icar*, **387**, 115152
- Pilling, S., Seperuelo Duarte, E., da Silveira, E. F., et al. 2010a, *A&A*, **509**, A87
- Pilling, S., Seperuelo Duarte, E., Domaracka, A., et al. 2010b, *A&A*, **523**, A77
- Pinilla-Alonso, N., Brunetto, R., De Prá, M. N., et al. 2025, *NatAs*, **9**, 230
- Pinilla-Alonso, N., Licandro, J., Brunetto, R., et al. 2024, *A&A*, **692**, L11
- Ponciano, C. R., Farenzena, L. S., Collado, V. M., da Silveira, E. F., & Wien, K. 2005, *JMoSp*, **244**, 41
- Poston, M. J., Mahjoub, A., Ehlmann, B. L., et al. 2018, *ApJ*, **856**, 124
- Potapov, A., Fulvio, D., Krasnokutski, S., Jager, C., & Henning, T. 2022, *JPCA*, **126**, 1627
- Prasad, S. S., & Tarafdar, S. P. 1983, *ApJ*, **267**, 603
- Prialnik, D. K., Barucci, A., & Young, L. 2020, The Trans-Neptunian Solar System (1st ed.; Amsterdam: Elsevier Science)
- Protopapa, S., Raut, U., Wong, I., et al. 2024, *NatCo*, **15**, 8247
- Quirico, E., Bacmann, A., Wolters, C., et al. 2023, *Icar*, **394**, 115396
- Raut, U., Famá, M., Loeffler, M. J., & Baragiola, R. A. 2008, *ApJ*, **687**, 1070
- Rodríguez-Lazcano, Y., Maté, B., Herrero, V. J., Escribano, R., & Gálvez, Ó. 2014, *PCCP*, **16**, 3371
- Roser, J. E., Ricca, A., Cartwright, R. J., Dalle Ore, C., & Cruikshank, D. P. 2021, *PSJ*, **2**, 240
- Sakakibara, N., Yu, P. Y., Ito, T., & Terashima, K. 2020, *ApJL*, **891**, L44
- Sandford, S. A., Nuevo, M., Bera, P. P., & Lee, T. J. 2020, *ChRev*, **120**, 4616
- Schmidt, F., Borrman, T., Mues, M. P., et al. 2022, *Atoms*, **10**, 25
- Schmidt, F., Swiderek, P., & Bredehöft, J. H. 2019, *ESC*, **3**, 1974
- Schmidt, F., Swiderek, P., Scheele, T., & Bredehöft, J. H. 2021, *PCCP*, **23**, 11649
- Seccull, T., Fraser, W. C., Kiersz, D. A., & Puzia, T. H. 2024, *PSJ*, **5**, 42
- Seccull, T., Fraser, W. C., Puzia, T. H., Brown, M. E., & Schönebeck, F. 2018, *ApJL*, **855**, L26
- Socrates, G. 2004, Infrared and Raman Characteristic Group Frequencies: Tables and Charts (3rd ed.; Chichester: Wiley)
- Soland, N. E., Roh, I., Huynh, W.-S., & Yang, P. 2023, *ACS Sust. Chem. Eng.*, **11**, 12478
- Souza-Feliciano, A. C., Holler, B. J., Pinilla-Alonso, N., et al. 2024, *A&A*, **681**, L17
- Strazzulla, G., Cooper, J. F., Christian, E. R., & Johnson, R. E. 2003, *CRPhy*, **4**, 791
- Teolis, B. D., Loeffler, M. J., Raut, U., Famá, M., & Baragiola, R. A. 2007, *Icar*, **190**, 274
- Tielens, A. G. G. M. 2013, *RvMP*, **85**, 1021
- Tonauer, C. M., Kock, E. M., Gasser, T. M., et al. 2021, *JPCA*, **125**, 1062
- Torres-Díaz, D., Basalgète, R., Amiaud, L., et al. 2024, *A&A*, **690**, A90
- Tribbett, P. D., Tegler, S. C., & Loeffler, M. J. 2021, *ApJ*, **915**, 40
- Tsuge, M., Hidaka, H., Kouchi, A., & Watanabe, N. 2020, *ApJ*, **900**, 187
- Turner, A. M., Abplanalp, M. J., Chen, S. Y., et al. 2015, *PCCP*, **17**, 27281
- Turner, A. M., Bergantini, A., Koutsogiannis, A. S., et al. 2021a, *ApJ*, **916**, 74
- Turner, A. M., Chandra, S., Fortenberry, R. C., & Kaiser, R. I. 2021b, *ChemPhysChem*, **22**, 985
- Turner, A. M., & Kaiser, R. I. 2020, *AcChR*, **53**, 2791
- Turner, A. M., Koutsogiannis, A. S., Kleimeier, N. F., et al. 2020, *ApJ*, **896**, 88
- Urso, R. G., Vuitton, V., Danger, G., et al. 2020, *A&A*, **644**, A115
- van Dishoeck, E. F., Herbst, E., & Neufeld, D. A. 2013, *ChRv*, **113**, 9043
- Vasconcelos, F. A., Pilling, S., Agnihotri, A., Rothard, H., & Boduch, P. 2020, *Icar*, **351**, 113944
- Vasconcelos, F. d. A., Pilling, S., Rocha, W. R. M., Rothard, H., & Boduch, P. 2017, *ApJ*, **850**, 174
- Vinogradoff, V., Fray, N., Duvernay, F., et al. 2013, *A&A*, **551**, A128
- Vinogradoff, V., Leyva, V., Mates-Torres, E., et al. 2024, *E&PSL*, **626**, 11855
- Volosatova, A. D., Tyurin, D. A., & Feldman, V. I. 2022, *JPCA*, **126**, 3893
- Wada, A., Mochizuki, N., & Hiraoka, K. 2006, *ApJ*, **644**, 300
- Walton, C. R., Rigley, J. K., Lipp, A., et al. 2024, *NatAs*, **8**, 556
- Wang, J., Nikolayev, A. A., Marks, J. H., et al. 2024a, *JACbS*, **146**, 28437
- Wang, J., Turner, A. M., Marks, J. H., et al. 2024b, *ApJ*, **967**, 79
- Wang, X., & Burgi, T. 2021, *AngCh*, **60**, 7860
- Wohar, M. M., & Jagodzinski, P. W. 1991, *JMoSp*, **148**, 13
- Wu, C. Y. R., Judge, D. L., Cheng, B. M., et al. 2003, *JGRE*, **108**, 5032
- Yeghikyan, A. 2017, *Ap*, **60**, 374
- Young, L. A., Braga-Ribas, F., & Johnson, R. E. 2020, in The Trans-Neptunian Solar System, ed. D. Prialnik, M. A. Barucci, & L. A. Young (1st ed.; Amsterdam: Elsevier), 127
- Zanchet, A., Rodríguez-Lazcano, Y., Gálvez, Ó., et al. 2013, *ApJ*, **777**, 26
- Zasimov, P. V., Sanochkina, E. V., Tyurin, D. A., & Feldman, V. I. 2023, *PCCP*, **25**, 21883
- Zhang, C., Leyvac, V., Wang, J., et al. 2024, *PNAS*, **121**, e2320215121
- Zhang, C., Wang, J., Turner, A. M., et al. 2023a, *ApJ*, **952**, 132
- Zhang, C., Wang, J., Turner, A. M., Young, L. A., & Kaiser, R. I. 2025a, *ApJS*, **278**, 30
- Zhang, C., Young, L. A., & Kaiser, R. I. 2025b, *ApJ*, **980**, 248
- Zhang, C., Zhu, C., Turner, A. M., et al. 2023b, *SciA*, **9**, eadg6936
- Zheng, W., Jewitt, D., & Kaiser, R. I. 2006a, *ApJ*, **639**, 534
- Zheng, W., Jewitt, D., & Kaiser, R. I. 2006b, *ApJ*, **648**, 753
- Zheng, W., Jewitt, D., & Kaiser, R. I. 2009a, *ApJS*, **181**, 53
- Zheng, W., Jewitt, D., & Kaiser, R. I. 2009b, *JPCA*, **113**, 11174
- Zheng, W., Jewitt, D., Osamura, Y., & Kaiser, R. I. 2008, *ApJ*, **674**, 1242
- Zheng, W., & Kaiser, R. I. 2007a, *CPL*, **440**, 229
- Zheng, W., & Kaiser, R. I. 2007b, *CPL*, **450**, 55
- Zheng, W., & Kaiser, R. I. 2010, *JPCA*, **114**, 5251
- Zheng, W., Kim, Y. S., & Kaiser, R. I. 2011, *PCCP*, **13**, 15749
- Zhu, C., Bergantini, A., Singh, S. K., Abplanalp, M. J., & Kaiser, R. I. 2021, *ApJ*, **920**, 73
- Zhu, C., Turner, A. M., Abplanalp, M. J., & Kaiser, R. I. 2018, *ApJS*, **234**, 15
- Zhu, C., Turner, A. M., Meinert, C., & Kaiser, R. I. 2020, *ApJ*, **889**, 134